Analysing Potential Drivers of Recurrent Rossby Wave Packets using Causal Inference

Master Thesis

Faculty of Science, University of Bern

handed in by

Lukas Meyer

January 2022

Supervisor:

Prof. Dr. Olivia Romppainen-Martius

Institute of Geography and Oeschger Centre for Climate Change Research, University of Bern

Advisors:

Mubashshir Ali

Institute of Geography and Oeschger Centre for Climate Change Research, University of Bern

Dr. Jakob Zscheischler

Physics Institute and Oeschger Centre for Climate Change Research, University of Bern

Department of Computational Hydrosystems Helmholtz Centre for Environmental Research

Abstract

The persistence of weather events plays a large role for the associated impacts and thus society. Understanding the mechanisms leading to persistent weather can improve forecasting skill of such events. Recurrent Rossby wave packets (RRWPs) have recently been recognised to produce persistent high-impact weather. However, little is known about what causes RRWPs. Therefore, this thesis investigates potential drivers of boreal winter RRWPs in the North Atlantic and eastern North Pacific basins. This work shows that atmospheric blocking, changes in the zonal background flow, and, to a lesser degree, forcing from deep convection are drivers of RRWPs. Areas where blocks, the background flow, and deep convection are linked to RRWP events are identified using composite maps and regression analysis. Subsequently, the causal inference method PCMCI was used to quantify the strength and time lags of causal links between RRWPs, measured by the R-metric R, and these possible drivers. We find that R is increased after an increase in the local background flow at a lag of one week in both basins. In the North Atlantic, R increases after an increase in blocking in the central North Atlantic within a week, whilst in the eastern North Pacific, an increase in R is preceded by an increase in Greenland blocking at a lag of one week. Increases in R can also be caused by strengthened deep convection. Finally, I find that R also drives many of the investigated processes and can foster downstream blocking, decrease the local background flow, and invigorate tropical convection. These results highlight the large interconnectedness between transient RRWPs, the background flow, and blocking. By identifying regions where these drivers influence R and by providing consistent causal pathways for these interactions, this work suggests that prediction of RRWPs could be improved by further studying these pathways.

Table of Contents

1. Introduction

1.1   Persistent surface weather and extreme events

The persistence of weather phenomena is often crucial to the impacts on the surface (Davies, 2015; Barton et al., 2016; Pfleiderer and Coumou, 2018; Lenggenhager et al., 2019; Röthlisberger and Martius, 2019). Persistent weather can lead to prolonged extreme conditions such as cold spells (Hoskins and Sardeshmukh, 1987; Davies, 2015), heavy precipitation (Barton et al., 2016; Lenggenhager et al., 2019), dry spells and heatwaves (Röthlisberger and Martius, 2019). Extreme events often have a large socio-economic impact, damaging property and livestock, creating various physical and mental health-related issues, and producing direct or indirect mortality (Huynen et al., 2001; MeteoSchweiz, 2006; Gosling et al., 2009; Hajat et al., 2010). A better understanding of the atmospheric processes leading to persistent surface weather patterns is vital for accurate weather forecasts, especially concerning extreme events (Cassou, 2008; Horton et al., 2015; Quandt et al., 2017).

1.2   Upper-level dynamics and recurrent Rossby wave packets

The surface weather systems such as cyclones and anticyclones are to a large degree steered by synoptic-scale transient Rossby waves (RWs) at upper levels (Hoskins et al., 1985; see Appendix A1.1 for a brief introduction to RW theory). It is well established that when the upper-level RWs move slowly or become quasi-stationary they can cause persistent, and thus possibly high-impact surface weather. Examples include atmospheric blocking (Hoskins and Sardeshmukh, 1987; Buehler et al., 2011; Sillmann et al., 2011; Pfahl and Wernli, 2012; Whan et al., 2016; Lenggenhager et al., 2019) or nearly stationary troughs, as in the case described by Blackburn et al. (2008). They found that extremely persistent RW patterns caused nearly stationary troughs and thereby lead to prolonged precipitation and subsequent floods over the United Kingdom in summer 2007. Generally, slower moving RWs have been suggested to cause more persistent surface weather (Francis and Vavrus, 2012 and 2015).

However, non-stationary, transient flow configurations can also cause extreme weather. The amplitude of RWs is often not uniform across longitude and time, with local maxima confined to certain longitudes and amplitude decreasing with distance (Fig. 1; Wirth et al., 2018). An area of enhanced RW amplification is termed Rossby wave packet (RWP) and is denoted by the envelope of the amplified waves. In part due to the large amplitude RWs confined within RWPs, which are prone to wave breaking (Wirth et al., 2018), RWPs can act as a precursor to high-impact surface weather (Davies, 2015; Barton et al., 2016; Röthlisberger et al., 2016; Fragkoulidis et al., 2018). This suggests another mechanism leading to persistent surface weather: The repeated occurrence of the same flow pattern over the same spatial area. Concretely, a series of transient RWPs can occur in phase and the troughs and ridges of each RWP will amplify over the same region repeatedly. This can cause "persistent" surface weather co-located with, as well as up and downstream of, the area of repeated amplification (Röthlisberger et al., 2019; Ali et al., 2021).

These so-called recurrent Rossby wave packets (RRWPs) were first formally described by Röthlisberger et al. (2019), who also introduced a quantity to measure RRWPs, the R-metric (R). Furthermore, they showed that the transient RWPs which caused the extreme precipitation in 1993 described by Barton et al. (2016) and the RWPs which caused the cold spell over the US described by Davies (2015) were RRWPs characterized by high values of R. Climatological evidence also shows that RRWPs can increase the duration of northern hemisphere winter cold spells and summer hot spells (Röthlisberger et al., 2019) and dry and wet spells in both hemispheres (Ali et al., 2021). These findings are supported by case studies, showing the causal effect of RRWPs on the surface weather (Röthlisberger et al., 2019; Ali et al., 2021). From the perspective of human wellbeing, the impacts of the persistent surface weather associated with RRWPs are mainly important over land. Considering the land-surface effects of northern hemisphere RRWPs in boreal winter, Röthlisberger et al. (2019) found that R increases the duration of cold spells in extended boreal winter over the east - and west coast of the US as well as over the Mediterranean. Ali et al. (2021) showed that RRWPs are also linked to an increase in the duration of extended boreal winter wet spells over central Europe and the Mediterranean, and to a lesser degree over the eastern US. Furthermore, they found that RRWPs increase the duration

of extended boreal winter dry spells over the entire US and central Asia. Hence, for boreal winter, RRWPs upstream of the affected land masses, mainly North America and Europe, warrant attention.
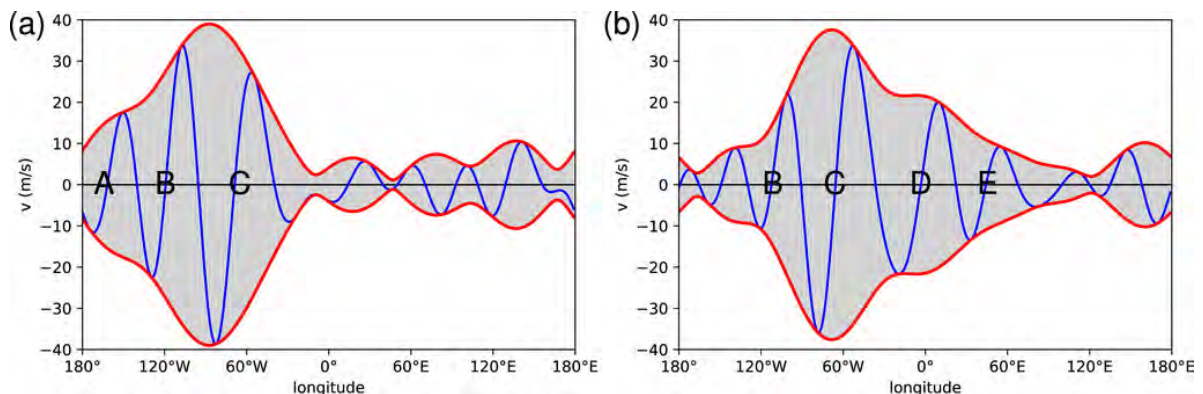
Figure 1: A Rossby wave packet at a) 00:00 UTC 7th August 2002 and b) 48 hours later at 00:00 UTC 9th August. The meridional wind *V* at 300 hPa meridionally averaged (40° N to 60° N) and filtered for synoptic wavenumbers 4-10 is shown with blue lines. The envelope is shown with red lines and capital letters denote individual troughs. Note that the RWP propagates faster than the RWs and hence trough A has dissipated between (a) and (b), whilst new troughs D and E have formed in (b), exemplifying downstream development. Taken from Wirth et al. (2018).

Moreover, RWPs, and consequently RRWPs, are of interest for weather forecasting and predictability. The predictability of RWPs can be higher than that of individual troughs and ridges contained within (Glatt and Wirth, 2014). However, Glatt and Wirth (2014) found that a RWP was only well predicted by a numerical weather prediction model if it was already present at the time of model initiation. The onset of the RWP is not well resolved. Furthermore, forecast errors can propagate with RWPs, thus causing substantial forecasting uncertainty in the downstream area of RWPs (Wirth et al., 2018). Finally, the large impact of RRWPs on the persistence of surface weather (Davies, 2015; Barton et al., 2016; Fragkoulidis et al., 2018; Röthlisberger et al., 2019; Ali et al., 2021) highlight the potential gain in forecasting capabilities in the seasonal to sub-seasonal realm if RRWPs were accurately predicted.

1.3 Causes of RRWPs

However, the atmospheric processes driving RRWPs are not known. Amongst others, Röthlisberger et al. (2019) list the following phenomena as possible drivers of RRWPs: Atmospheric blocking, wave–mean flow interactions, and Rossby wave forcing from the tropics.

1.3.1 Atmospheric blocking

Röthlisberger et al. (2019) investigated composites of *R* anomalies centred on blocks in the North Pacific and the North Atlantic. They found that *R* values increased considerably downstream of blocks 3-9 days prior and again 3-6 days after the time of maximum blocking. Atmospheric blocking might initiate a wave train downstream, a mechanism described by Altenhoff et al. (2008), and thus cause RRWPs. Blocking is also identified up and downstream of, as well as co-located with, positive *R* anomalies in two case studies of RRWPs by Röthlisberger et al. (2019). Moreover, Ali et al. (2021) investigated prolonged dry anomalies over São Paulo in November 1985 triggered by RRWPs and found blocking upstream of the RRWPs. They also investigated a RRWP episode over the North Atlantic associated with persistent wet conditions and anomalous precipitation over the Iberian Peninsula. Blocking conditions were found upstream of this event, over the Gulf of Alaska and southern Greenland. Blocking also contributed to the RRWPs leading to the 1993 clustered extreme precipitation event over Switzerland described by Barton et al. (2016). Here, blocking over the Gulf of Alaska caused phase locking of the Rossby waves downstream which was reinforced by blocking in the North Atlantic. In summary, blocking upstream might cause in phase wave trains and thus RRWPs downstream. Röthlisberger et al. (2019) also describe a different interaction between *R* and blocking. They found positive *R* anomalies upstream of blocking events 3-9 days prior to, and for about 3-6 days after the

time of maximum amplitude of the blocks. Here, waves amplifying in phase might continuously strengthen the block downstream and hence blocking does not act as a driver of RRWPs but vice versa.

1.3.2 Changes in the background flow

The jet stream (hereafter jet), a band of enhanced zonal wind, often acts as a waveguide for RWPs so that they propagate eastwards with the direction of the jet (Martius et al., 2010). Waveguides can also be viewed as areas with a large meridional gradient of potential vorticity (PV) along which Rossby waves, which are PV anomalies triggered by local perturbations of PV, can propagate (Martius et al., 2010; Wirth et al., 2018). Therefore, the state of the waveguide affects the propagation of RWPs (Wirth et al., 2018). Generally, higher jet amplitudes and lower jet width increase the capacity of the jet to act as waveguide (Martius et al., 2010; Wirth, 2020). A stronger, narrower, and therefore more zonal jet consequently corresponds to a better, more zonal waveguide with increased propagation of waves and RWPs in the zonal direction (Wirth et al., 2018; Wirth, 2020). Consequently, the amplitude of the meridional wind V, which is directly linked to RWs and RWPs, is smaller on a more zonally aligned jet (Wirth et al., 2018). Conversely, a wider and weaker jet also affects the propagation of RWPs, and therefore RRWPs, by causing weaker eastward propagation and enabling larger meridional amplification, i.e., wavier flow (Wirth et al., 2018; Wirth, 2020). In terms of PV thinking, this waveguidability of the jet depends strongly on the meridional PV gradient. Large meridional gradients are conductive of strong zonal propagation of RWs and vice versa (Wirth, 2020).

Furthermore, diffluent flow, flow which decelerates and fans outwards, can also influence Rossby wave propagation. Nakamura and Huang (2017) investigated connections between high-frequency transient wave trains and diffluent flow. They found that advection of local wave activity (LWA) from upstream and the local deceleration of the background flow in regions with diffluent flow can cause large meridional PV perturbations, i.e., wavey flow, and eventually a blocking like pattern. This shows that a diffluent flow can develop into a blocked or meridional state due to forcing from high-frequency transient waves upstream (presumably advected on a more zonal flow). Furthermore, results from Huang and Nakamura (2017) indicate that the advection of LWA and the deceleration and diffluence of the background flow can reinforce each other. Therefore, a process might be conceivable where advection of LWA on a strong westerly flow leads to recurrence of amplified waves in areas of diffluent flow, as often found at the jet exit regions.

In practice, the waveguide can be approximated using the zonal wind field. Thereby, the background flow is often defined as a time and/or low pass filtered product of the wind (Wirth et al., 2018). In summary, changes in the upper-level background flow, mainly in the zonal wind U, are related to the waveguide and will interact with RWPs by influencing both their propagation and amplification within the extratropics.

1.3.3 Rossby wave forcing from deep convection

Latent heat release from deep tropical convection and divergent outflow at upper levels can act as a Rossby wave source and force atmospheric circulation in other areas (Wheeler and Hendon, 2004; Moore et al., 2010), e.g., by advection of air with anomalous absolute vorticity from the outflow (Cassou, 2008; Li et al., 2020). The common response is an anticyclone to the north-west of the anomalous convection, which can initiate a RWP and acts to strengthen the waveguide north of the anticyclone as the meridional absolute vorticity gradient is enhanced locally (Moore et al., 2010). Concretely, changes in the extratropical flow in the North Atlantic region have been linked to deep convection in the Caribbean and central Atlantic region (Hoskins and Sardeshmukh, 1987; Li et al., 2020), but also to deep convection in the tropical Pacific, which has been related to the Madden Julian Oscillation (MJO; Cassou, 2008). The North Pacific extratropical flow has also been shown to be sensitive to forcing from the tropical Pacific and Indian oceans (Moore et al., 2010).

Therefore, RRWPs might be initiated or influenced by RW forcing from deep convection. Barton et al. (2016) connected a series of RW trains to tropical forcing in the form of an active MJO phase 2 in the Indian Ocean. They found that low outgoing longwave radiation (OLR) values and associated divergent upper-level outflow caused anticyclonic flow anomalies northwards of the anomalous divergence. These anticyclonic anomalies initiated and strengthened a series of far-reaching wave trains which were

linked to RW breaking over Europe and extreme precipitation over Switzerland. This episode was characterized by high R values exceeding 15 m s^{-1} between 180° W and 150° W and R values of 12 m s^{-1} around 10° W from 21st September until 13th October 2002 (see Appendix A1.2). In his case study of the cold and wet winter 2013/2014 in Europe and North America, Davies (2015) studied backward trajectories of air parcels which formed the upper-level troughs and ridges constituting the RRWPs (Röthlisberger et al., 2019). The amplification of these RRWPs resulted from extreme relative PV values, which were in part generated by diabatic processes. Davies (2015) showed that some of the air parcels reaching the North Atlantic came from lower levels (800 to 500 hPa) of the eastern tropical Pacific, around 25° N and 170° W, and underwent large diabatic ascent over Central America before reaching the RWPs. Further upstream, air parcels which joined and possibly strengthened a ridge over the northeast Pacific originated in the tropics, around 10° N, 95° E and experienced ascent over the western tropical Pacific.

OLR has been used as a proxy for intense tropical convection in many studies (Kiladis, 1998; Wheeler and Hendon, 2004; Cassou, 2008; Moore et al., 2010; Kiladis et al., 2014; van der Wiel et al., 2016; Di Capua et al., 2020b), as deep tropical convection leads to high cloud tops and thus lower emission temperatures and lower OLR values. Furthermore, the divergent outflow at upper levels resulting from the ascending air can also be used as an indicator of deep convection (Cassou, 2008; Moore et al., 2010; Barton et al., 2016).

1.4   Causal inference

To summarize, there exist many potential drivers of RRWPs but no dedicated studies to investigate them. Atmospheric blocking, changes in the background flow, and RW forcing from deep convection are three plausible drivers (Röthlisberger et al., 2019) which are also interconnected (Moore et al., 2010; Nakamura and Huang, 2017; Li et al., 2020).

Identifying cause and effect in complex systems such as the earth-system is often not possible using conventional statistical methods (Moore et al., 2010; Kretschmer et al., 2016; Runge, 2018; Runge et al., 2019a and 2019b). To overcome this hurdle, novel approaches based on causal inference methods have been developed and increasingly applied in atmospheric sciences. Ebert-Uphoff and Deng (2012) first used causal discovery to study relations between large climate oscillations. Causal inference methods in atmospheric science have further been used to study atmospheric flow changes (Deng and Ebert-Uphoff, 2014), teleconnections between ENSO and the Walker circulation (Runge et al., 2014), monsoon dynamics (Runge et al., 2015; Di Capua et al., 2020a and 2020b), the Atlantic meridional overturning circulation and its influence on global temperature variability (Schleussner et al., 2014), and Arctic drivers of midlatitude winter circulation (Kretschmer et al., 2016).

One such method is the *Peter and Clark momentary conditional independence* (PCMCI) algorithm (Runge, 2018; Runge et al., 2019b), a causal inference method which combines a condition-selection step, the PC algorithm developed by Spirtes and Glymour (1991), with a momentary conditional independence (MCI) test. PCMCI deals well with autocorrelated, high dimensional, and non-linear time series and is therefore suited for complex interactions as is often the case in the climate system (Runge et al., 2019a and 2019b).

1.5   Research questions

In this thesis, areas where atmospheric blocking, the background flow, and deep convection might drive the occurrence of boreal winter RRWPs in the North Atlantic and eastern North Pacific are identified using composite maps and regression analysis. The causal inference method PCMCI is applied to find relevant links and their time lags between RRWPs and these potential drivers. Applying causal inference methods to a complex, not yet fully understood phenomenon such as drivers of RRWPs, can yield insight into the direction, strength, and temporal scale of these processes. Thus, two research questions can be derived.

I.   **In what regions are changes in atmospheric blocking, the background flow, and deep convection related to RRWPs in the North Atlantic and eastern North Pacific in boreal winter, as measured by the R-metric?**

II.   **At what time lags and with which link strength do atmospheric blocking, the background flow, and deep convection in the regions identified in I. interact with RRWPs?**

Moreover, from a methodological point of view, the insights gained during this work will also contribute to evaluating an emerging statistical method to take advantage of the large amount of data available in climate sciences. This leads to a final, broader research question.

III. **How can causal inference be applied to capture links between synoptic-scale phenomena such as RRWPs and their drivers?**

2. Data and Methods

2.1 Data

Data from the ERA5 reanalysis (Hersbach et al., 2020) from 01.01.1979 to 31.12.2018 was used. The spatial resolution is 31 km horizontally and 137 levels up to 0.01 hPa vertically and its output frequency is hourly. In this work the data was resampled to daily resolution. Data was available at 0.5° by 0.5° spatial resolution, except for atmospheric blocking, where 1° by 1° data was used. In this thesis, December, January, and February (DJF) are investigated.

2.1.1 R-metric

The R-metric, R, quantifies RRWPs. It was developed by Röthlisberger et al. (2019) and describes a time – and wavenumber filtered 250 hPa meridional wind velocity (Ali et al., 2021). It has high values, when troughs and ridges repeatedly amplify in phase, that is at the same longitudes. R used in this work is derived from the ERA5 meridional wind ("V-component of wind") at 250 hPa using publicly available code (Ali and Röthlisberger, 2021). For a detailed description see Röthlisberger et al. (2019). The derivation of R can be broken down into 4 consecutive steps (Fig. 2):

1. Meridionally average the 250 hPa meridional wind from 35° N to 65° N.
2. Apply a 14.25-day running mean filter to only retain signals lasting longer than the synoptic scale. Note that 14.25 corresponds to approximately two synoptic-scale Rossby wave periods. This removes instances where synoptic-scale waves do not amplify in phase.
3. Apply a high-pass filter for synoptic (4–15) wavenumber signals to remove planetary-scale waves and retain synoptic-scale waves.
4. Calculate the envelope of this synoptic wavenumber signal.

In this work, R was further zonally averaged over (1) the area between 50° W to 10° E for R in the North Atlantic (R_{N-Atl}) and (2) the area between 175° W to 115° W for R in the eastern North Pacific (R_{NE-Pac}), thus deriving a daily time series of R for each region. In both these areas the mean and 95th percentile of R in DJF is high (Fig. 3). The link between R and persistent DJF surface weather downstream of these ocean basins has been established in section 1.2 (Röthlisberger et al., 2019; Ali et al., 2021).

2.1.2 Atmospheric blocking, PV, and the Atlantic European weather regimes

Atmospheric blocking is defined based on negative upper level (500-150 hPa) PV anomalies as in Schwierz et al. (2004) with modifications following Rohrer et al. (2018). Hereby, PV anomalies below -1.3 PVU (1 PVU = $10^{-6} \, K \, kg^{-1} \, m^2 \, s^{-2}$) which can be identified for a minimum of 5 consecutive days and whose area between 6-hourly timesteps overlaps at least by 70 % are identified as blocked. In this thesis, the 6-hourly data was resampled to daily data by assigning a grid cell as blocked on a given day, if a block was present on any one of the four 6-hourly time steps within said day. PV on the 320 K isentrope was used in the composite maps to show the approximate location of the jet, i.e., waveguide (Martius et al., 2010; Wirth et al., 2018). Röthlisberger et al. (2018) show that the 320 K isentrope displays the largest PV gradient between the latitudes 35° N to 65° N in DJF and is thus best suited to represent the extratropical waveguide (Martius et al., 2010). For the North Atlantic, there is a tradition of classifying the synoptic situation using weather regimes (Vautard, 1990; Cassou, 2008), which include blocked weather situations. In this work the *Atlantic European weather regimes* defined by Grams et al. (2017) are used to represent selected blocking patterns like Greenland blocking (see Appendix A2.1 for a full description of the weather regimes).

2.1.3 Background flow

The background flow was approximated using the instantaneous, low-pass filtered for zonal wavenumbers 0 to 3 zonal wind U at 250 hPa ($U250_{wvnf\,k0k3}$). Most common definitions of the background flow include not only such a filtering for low-frequency wavenumbers but also averaging over time (Wirth et al., 2018). This was not done in this work, as potential areas of interest revealed by analysing the background flow shall be used in PCMCI. Time-averaged quantities have higher than

usual autocorrelation, which reduces the detection power of PCMCI (Runge et al., 2019b; Runge, 2020). Furthermore, this quantity should represent the atmospheric background state, or the position and strength of jet acting as a waveguide at a given moment, and thus instantaneous values are more appropriate. In this work, I limit the investigation to areas related to the jet, which are defined as anomalies in proximity to the climatological jets (Moore et al., 2010; Li et al., 2020).

2.1.4 Deep convection - outgoing longwave radiation and velocity potential

The negative of ERA5 *mean top net long-wave radiation flux* was used as OLR data (Hersbach et al., 2018). Enhanced convection is captured by small absolute values of OLR (Kiladis, 1998; Moore et al., 2010; Li et al., 2020) or when considering anomalies, by negative OLR anomalies (Cassou, 2008). As deep convection leads to divergent outflow at upper levels, negative velocity potential (VP) values or anomalies at upper levels can be used to track tropical deep convection (Cassou, 2008; Kiladis et al., 2014). In this work, velocity potential at 250 hPa, derived from ERA5 zonal and meridional wind, was used in conjunction with OLR to determine areas with enhanced convection.
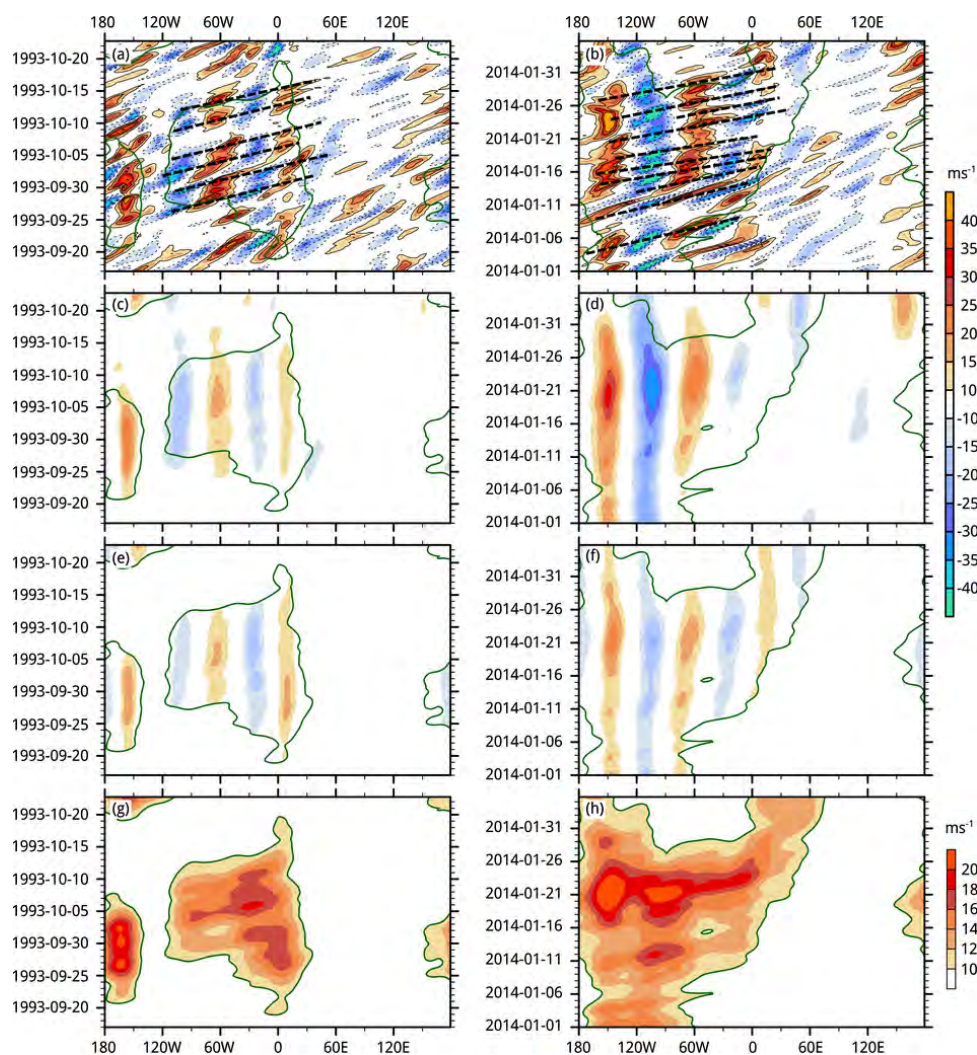
Figure 2: Calculation of R for two RRWP events. One event a), c), e), g) linked to extreme precipitation in autumn 1993 described by Barton et al. (2016) and another b), d), f), h) linked to persistent cold and wet conditions in winter 2013/2014 described by Davies (2015). Hovmöller diagrams a), b) show the 250 hPa meridionally averaged meridional wind V_{ma} in shadings and black dashed lines indicate the approximate trajectories of individual RWPs. After applying a time filter c), d), a wavenumber filter e), f), and calculating the envelope of this signal, R is retained g), h). Green contours indicate R of 10 m s^{-1}. Taken from Röthlisberger et al. (2019).
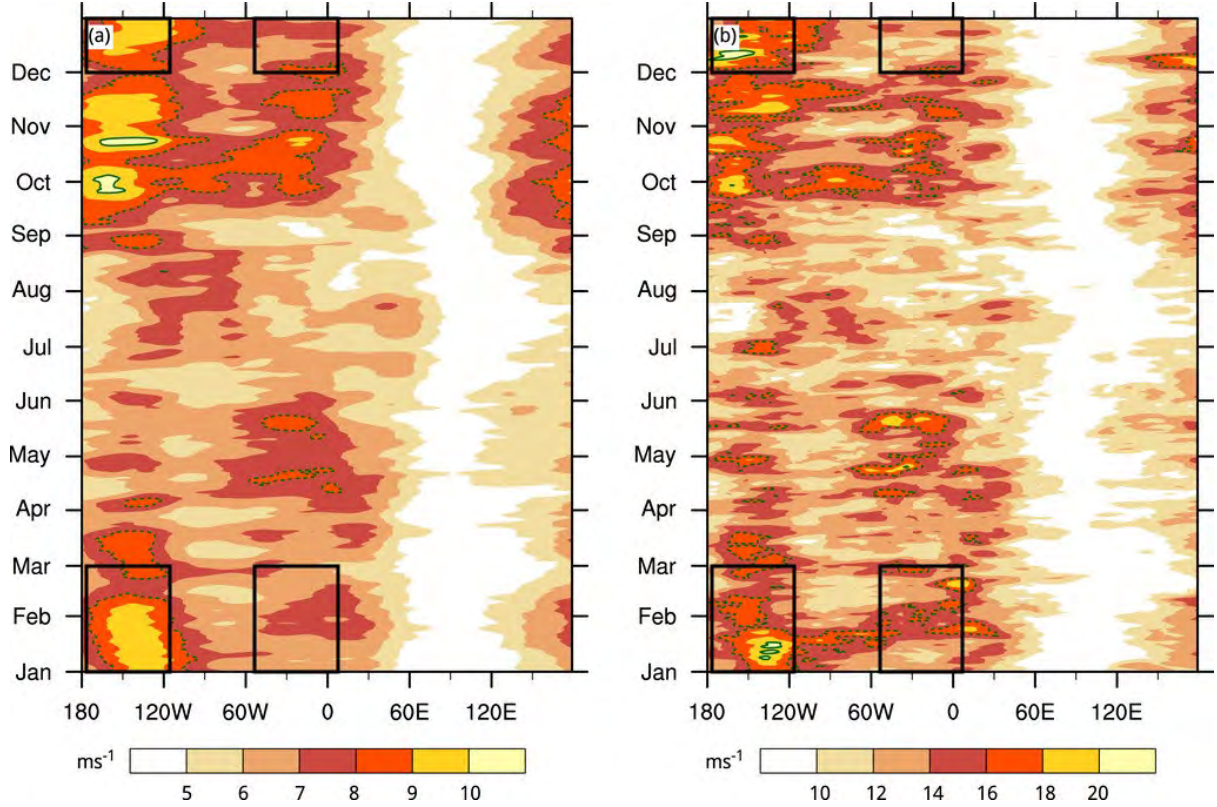
Figure 3: R **climatology a) and 95th percentile b) for each longitude and day of year. Taken from Röthlisberger et al. (2019). Black rectangles have been added to mark the study areas (North Atlantic: 50° W to 10° E; eastern North Pacific: 175° W to 115° W) and studied season (DJF) for this work.**

2.2 Methods

2.2.1 Composites

Composite maps are a useful tool to characterize the mean state of the atmosphere during periods of interest. In this work, composite maps of blocking frequency anomalies, $U250_{wvnf\,k0k3}$ anomalies, and OLR and VP anomalies leading up to and during days with RRWP activity, i.e., days where R is high, are created. Recall that time series of R averaged over the North Atlantic (R_{N-Atl}) and eastern North Pacific (R_{NE-Pac}) basins are studied. To investigate days with RRWPs, high R days (R_{high}) are defined as days where R, averaged over an ocean basin, is higher than the 85th percentile of R (R_{85pctl}) in that basin:

$$R_{high} = \{R_t \mid R_t \geq R_{85pctl}\}$$

(Eq. 1)

, read as: "R_{high} is the set of all elements of the form R_t where $R_t \geq R_{85pctl}$ holds", where R_t is the time series of R and t stands for time. The distribution of high R days within DJF (Fig. 4) reveals that they are spread evenly within DJF and that there is no tendency for high R days to fall within a certain month. This indicates that there is not much seasonality in occurrence of high R days within DJF. Furthermore, high R days in the North Atlantic (Fig. 4a) occur in shorter "bursts", whilst in the eastern North Pacific (Fig. 4b), high R days more often occur in long consecutive episodes.

8
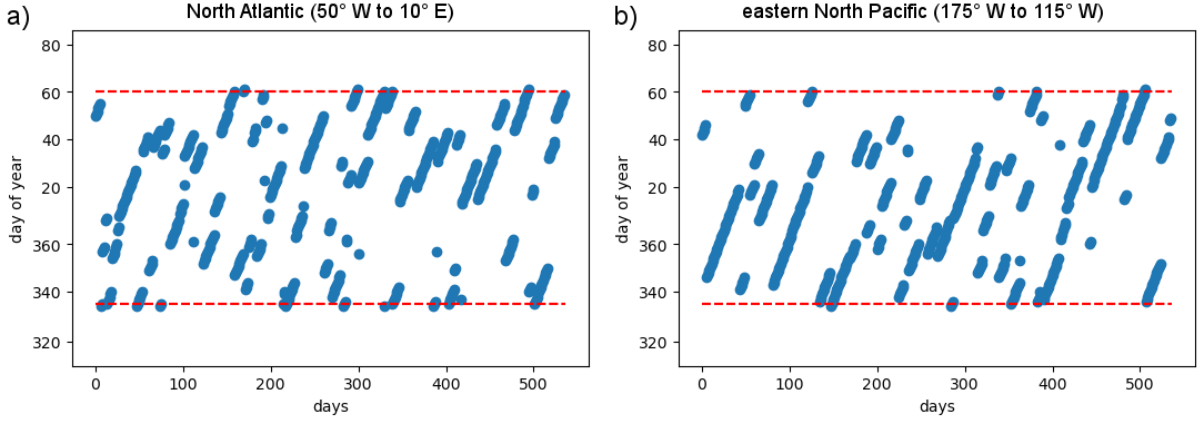
Figure 4: Distribution of high R days within DJF for a) the North Atlantic basin and b) the eastern North Pacific basin. The y-axis shows the day of year of each high R day, whilst the x-axis is the index of the n = 540 days during which R exceeded the 85th percentile of R within each basin. The horizontal red dashed lines show the boundaries of DJF by day of year.

To capture the state of the atmosphere during RRWPs, composites of selected variables were created during high R days. The composites display the mean difference to the seasonal climatology of the respective variable per gridpoint, e.g., the average difference in blocking frequency between the composite period, R_{high}, and the seasonal mean.

Furthermore, the conditions leading up to RRWPs are of interest to identify possible precursors of RRWPs. Therefore, time lagged composites with respect to high R days were also created. Since high R days often occur in long consecutive episodes (Fig. 4), days in the lagged composite sample are often also high R days. These high R days should not be included in the lagged composites, as the intent of this analysis is to examine the atmospheric state prior to RRWPs and remove any signal from RRWPs. Therefore, the composites at lag τ ($R_{high,\tau}$) were defined as:

$$R_{high,\tau} = \{R_{t-\tau} \mid R_t \geq R_{85pctl} \wedge R_{t-\tau} < R_{85pctl}\}$$

(Eq. 2)

, read as: "$R_{high,\tau}$ is the set of all elements of the form $R_{t-\tau}$ where $R_t \geq R_{85pctl}$ and $R_{t-\tau} < R_{85pctl}$ holds", where $R_{t-\tau}$ is the time series of R lagged by τ days. As an example, consider two days with high R in the North Atlantic: The 31st January and 1st February 1985 (t = 31.01.1985, 01.02.1985). Both dates are included in the non-lagged composite as $R_t \geq R_{85pctl}$ holds for both t. In the composite at lag $\tau = 1$ day (t-1 = 30.01.1985, 31.01.1985) only the 30.01.1985 is included as the 31.01.1985 is a high R day and $R_{t-\tau} < R_{85pctl}$ does not hold. In other words, if at a date within $t - \tau$, $R \geq R_{85pctl}$, then that date is removed from the t - τ composite.

Statistically significant areas were determined by applying a two-sided Welch's t-test (Welch, 1947) on the samples of low R days ($R_{low} = \{R_t \mid R_t \leq R_{15pctl}\}$; $R_{low,\tau} = \{R_{t-\tau} \mid R_t \leq R_{15pctl}\}$) and high R days at equivalent lags. The Welch's t-test is a variation of the Student's t-test, which does not assume equal sample variance as its test statistic value is calculated by including each sample's standard deviation. The test statistic *t* is calculated as:

$$t = \frac{\bar{x}_1 - \bar{x}_2}{\sqrt{\dfrac{\sigma_{x_1}^2}{n_1} + \dfrac{\sigma_{x_2}^2}{n_2}}}$$

(Eq. 3)

, where $\bar{x}_i$ is the mean of sample i, $\sigma_{x_i}^2$ is the variance of sample i, and n_i is the sample size. It should be noted that whilst the fraction of area blocked is not a normally distributed variable, the means of samples

9

will still be normally distributed and hence the Welch's t-test is appropriate. The unequal variance of the fraction of area blocked samples for high and low R is not an issue with the Welch's t test, as it does not assume equal sample variance.

The spatial field of p-values obtained by the Welch's t-test were corrected for multiple testing using the method by Benjamini and Hochberg (BH; 1995) to control the false discovery rate (FDR) to a given level. The FDR is defined as:

$$\mathrm{FDR} = \mathrm{E}\left(\frac{FP}{FP + TP}\right) = E\left(\frac{FP}{D}\right)$$

(Eq. 4)

, where E denotes the expected value, FP is the number of false positives and TP the number of true positives, and D the total discoveries, i.e., the sum of FP and TP. In this work the p-values were adjusted (i.e., increased) so that the FDR is constrained at 0.01. Concretely, the p-values are sorted by rank, k, where the smallest p-values receives rank 1. Then for each ranked p-value, p_k, an adjusted p-value, $p_{k,adj}$, is calculated:

$$p_{k,adj} = p_k \frac{m}{k}$$

(Eq. 5)

, where m is the total number of p-values and k is the rank of current p-value p_k. Note that $p_{k,adj} > p_k$, except for the largest p-value, where m = k, and thus $p_{k,adj} = p_k$. The BH adjusted p-value $p_{k,adj,BH}$ is then the smaller value of either $p_{k,adj}$ or the BH adjusted p-value of the next highest rank $p_{k+1,adj,BH}$:

$$p_{k,adj,BH} = \begin{cases} \mathbf{p_{k,adj}} \; if \; p_{k,adj} \leq p_{k+1,adj,BH} \\ \mathbf{p_{k+1,adj,BH}} \; if \; p_{k,adj} > p_{k+1,adj,BH} \end{cases}$$

(Eq. 6)

Finally, only gridpoints where $p_{k,adj,BH} \leq \alpha$, are marked as statistically significant, with $\alpha = 0.01$.

2.2.2 Regression analysis

Whilst composite maps show the mean state of the atmosphere associated with high R days, a regression analysis can provide information on whether the observed changes, e.g., large $U250_{wvnf\,k0k3}$ anomalies in a certain region, influence or can predict changes the dependent variable (Draper and Smith, 1998, p. 15-20), in this case R. Therefore, a linear least-squares regression of R on the variables described above was carried out:

$$Y_t = \beta_0 + \beta_1 X_t$$

(Eq. 7)

The R time series for the basin of choice (Y_t) was regressed against each gridpoint's time series of the selected variable (X_t). For each gridpoint, the slope parameter of the regression (β_1) indicates the mean change in R for one unit change in the dependent variable (X_t). Because blocking data is binary (1 if a block is present in a gridpoint, 0 if not) β_1 cannot be considered a slope parameter, since there are only two groups of data (0,1) instead of continuous values. Here X_t takes the form:

$$X_t = \begin{cases} 1 \; if \; block \; present \; at \; time \; t \\ 0 \; if \; no \; block \; present \; at \; time \; t \end{cases}$$

(Eq. 8)

and β_1 corresponds to the difference between expected R value $E(Y_t)$ in absence *(Eq. 9)* and presence *(Eq. 10)* of a block at each gridpoint. The expected R values are defined as:

$$E(Y_t \mid X_t = 0) = \beta_0$$

(Eq. 9)

$$E(Y_t \mid X_t = 1) = \beta_0 + \beta_1$$

(Eq. 10)

Thus, β_1 can be defined as:

$$\beta_1 = E(Y_t \mid X_t = 1) - E(Y_t \mid X_t = 0)$$

(Eq. 11)

In other words, β_1 is the difference in mean values of R between two groups distinguished by presence or absence of a block (Stock and Watson, 2015; p. 158-160).

Linear least square regression analysis assumes that observations are independent of each other (Draper and Smith, 1998, p. 62-69, p. 179ff.), an assumption that is violated in highly autocorrelated time series. As R is a 14.25-day time-averaged product of the meridional wind at 250 hPa, consecutive observations within 14.25 of each other are not independent and autocorrelation of R time series is high (Fig. 5). The autocorrelation stabilizes around lag 14 days at 0.07 for R_{N-Atl} (Fig. 5a) and 0.12 for R_{NE-Pac} (Fig. 5a). Therefore, only every 7th day of the time series was used for the regression to reduce autocorrelation. Whilst the observations are still not completely independent as would have been with selecting every 14th day, the results using every 14th day were sensitive to the choice of start date, meaning that the 14 different possible regression analyses differed. Using every 7th day gave similar results independently of start day selection. The autocorrelation of R at lag 7 is 0.42 for R_{N-Atl} (Fig. 5a) and 0.46 for R_{NE-Pac} (Fig. 5a), which is still considerable, but markedly lower than when using the whole dataset. Note that the partial autocorrelation drops to values around 0.1 at lag 7 (Figs. 5c and 5d). Therefore, an observation at lag 0 is nearly independent of an observation at lag 7 if lags 1,2,3, …, 6 are conditioned on.
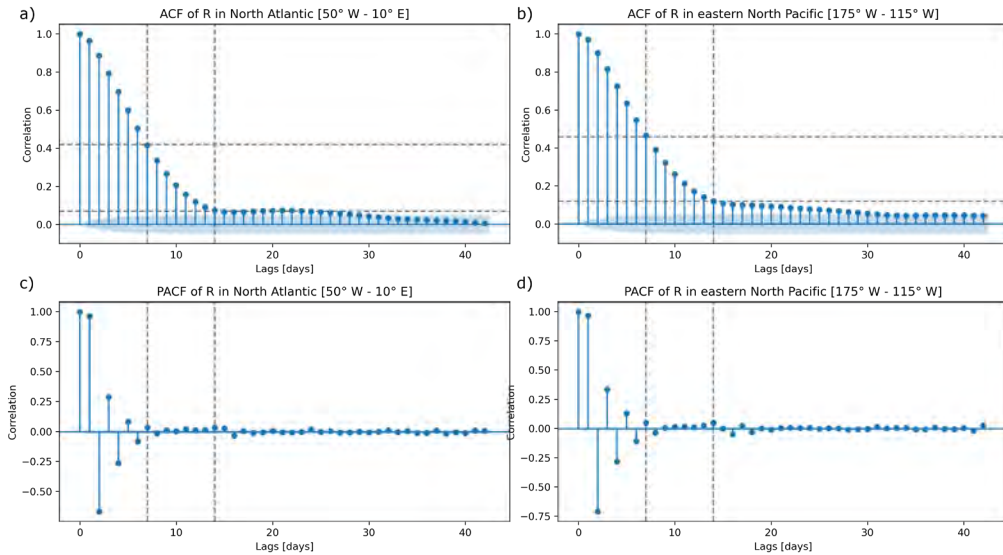
Figure 5: The autocorrelation function (ACF) and partial autocorrelation function (PACF) for time lags from 0 to 40 days for R over a) and c) the North Atlantic and b) and d) the eastern North Pacific. Shaded areas correspond to the 95 % confidence interval per lag. Vertical dashed lines mark lags 7 and 14 and horizontal dashed lines in a) and b) mark the correlation at those two lags.

The p-values obtained by the regression analysis indicate whether the obtained slope, β_1, differs significantly from 0 using a Wald test (Wald, 1943). The spatial field of p-values was corrected for multiple testing in the same manner as the p-values obtained from the significance test of the composites (Benjamini and Hochberg, 1995) and grid points where $p_{k,adj,BH} \leq 0.01$ are marked as significant.

2.2.3 PCMCI

The information from the composites and regression analysis as well as insights from the literature will be combined to build concrete hypotheses on what causes RRWPs. More precisely, the direction, strength, time lag, and if possible, driving physical mechanism behind causal links should be formulated. These hypotheses can then be tested using the causal inference tool PCMCI (Runge et al., 2019b), which quantifies link direction, time lags, and link strength. In the following section a theoretical introduction to PCMCI is first given. Then assumptions and limitations of PCMCI are considered, before PCMCI is applied to generic data to show its functionality. Finally, the concrete application of PCMCI to discern the causal drivers of RRWPs is discussed.

2.2.3.1 Theory of the PCMCI algorithm

PCMCI can be separated into two parts: The first step, the Peter and Clark algorithm (Spirtes and Glymour, 1991), detects causal drivers of each link, also called causal parents, whilst the second step, the momentary conditional independence test, quantifies the link strength. Both will be explained in the next paragraphs following the descriptions of Kretschmer et al. (2016), Runge (2018), Runge et al. (2019b), and Di Capua et al. (2020a).

1. Detecting the causal links with the Peter and Clark (PC) condition selection algorithm

Assume a system of time series $\boldsymbol{X}_t = (X_t^1, X_t^2, \ldots, X_t^N)$, where t indicates time and N is the number of time series in the system. The PC algorithm is applied to find the causal parents $\hat{P}(X_t^j)$ of the variable X_t^j, where $j \in N$, within the pool of selected univariate detrended time series $\boldsymbol{X}_t$. The assumption of time-order (cause precedes effect) is given in time series and therefore the direction of links is known (Runge, 2018). Simplified this means that the past causes the present. Therefore, the causal parents $\hat{P}(X_t^j)$ are variables within $\boldsymbol{X}_t$, at different time lags τ in the past, which have a causal effect on the examined variable in the present, X_t^j. For the PC algorithm two parameters must be defined by the user: The significance level for the partial correlation tests, α_{PC}, and the maximum time lag, τ_{max}.

- The pool of parents is first initialized as $\hat{P}(X_t^j) = (\boldsymbol{X}_{t-1}, \boldsymbol{X}_{t-2}, \ldots, \boldsymbol{X}_{t-\tau_{max}})$ thus containing every lagged timestep up to τ_{max} of every other variable, see the definition of $\boldsymbol{X}_t$ above. In a next step (iteration $p = 0$) any variable $X_{t-\tau}^i$, where $i \in N$, is removed from the parents $\hat{P}(X_t^j)$ if the null hypothesis

$$X_{t-\tau}^i \perp\!\!\!\perp X_t^j$$

(Eq. 12)

read as: $X_{t-\tau}^i$ and X_t^j are unconditionally independent

cannot be rejected at the significance threshold α_{PC}. This is done by removing all $X_{t-\tau}^i$ which do not significantly correlate with X_t^j.

- In subsequent steps (iterations $p = 1, 2, 3, \ldots$) any variable $X_{t-\tau}^i$ is removed from the parents $\hat{P}(X_t^j)$ if the null hypothesis

$$X_{t-\tau}^i \perp\!\!\!\perp X_t^j \mid S$$

(Eq. 13)

read as: $X_{t-\tau}^i$ and X_t^j are conditionally independent given S

cannot be rejected at the significance threshold α_{PC}. Here S refers to the p elements of $\hat{P}(X_t^j)$ which exhibited the strongest correlations to X_t^j in the previous iteration. This means that partial correlations are calculated between X_t^j and each element $X_{t-\tau}^i$ within $\hat{P}(X_t^j)$ conditional on the

first p most strongly correlating (with X_t^j) variables $X_{t-\tau}^i$ within $\hat{P}(X_t^j)$ as determined by the previous iteration, e.g., for iteration $p = 1$ the 1 most strongly correlating variable as identified in $p = 0$. See Kretschmer et al. (2016) for an applied example.

In other words, in each iteration p the remaining causal parents are tested for independence regarding the variable X_t^j conditional on the p most strongly correlating (with X_t^j) causal parents. If the hypothesis of conditional independence cannot be rejected, this means that there still exists a significant correlation between $X_{t-\tau}^i$ and X_t^j which cannot be explained only by the p most strongly correlating parent $\hat{P}(X_t^j)$. Hence, $X_{t-\tau}^i$ could be a causal parent of X_t^j and should not be removed from the pool. If the above null hypothesis is rejected, this means that $X_{t-\tau}^i$ and X_t^j are conditionally independent given S and thus $X_{t-\tau}^i$ should not be kept within the pool of causal parents.

- The algorithm converges once $S = \hat{P}(X_t^j) \setminus X_{t-\tau}^i$ (the number of parents is equal to the number of conditions) and the null hypothesis

$$X_{t-\tau}^i \perp\!\!\!\perp X_t^j \mid \hat{P}(X_t^j) \setminus X_{t-\tau}^i$$

(Eq. 14)

read as: $X_{t-\tau}^i$ and X_t^j are conditionally independent given the parents of X_t^j excluding $X_{t-\tau}^i$

is rejected. The output of the PC algorithm is that each variable (X_t^j) has a strongly reduced set of causal parents which can then be entered into the MCI algorithm.

2. *Quantifying the strength of the causal effects with the momentary conditional independence (MCI) test*

MCI tests every variable pair $X_{t-\tau}^i, X_t^j$ for a causal link $X_{t-\tau}^i \rightarrow X_t^j$, which is given if the null hypothesis

$$X_{t-\tau}^i \perp\!\!\!\perp X_t^j \mid \hat{P}(X_t^j) \setminus \{X_{t-\tau}^i\}, \hat{P}(X_{t-\tau}^i)$$

(Eq. 15)

read as: $X_{t-\tau}^i$ and X_t^j are conditionally independent given the parents of X_t^j excluding $X_{t-\tau}^i$ and given the parents of $X_{t-\tau}^i$

is rejected. This means that partial correlations are again calculated between each variable X_t^j and every other variable at every time lag up to τ_{max}, but now conditional on both the causal parents $\hat{P}(X_t^j)$ of X_t^j excluding the past $X_{t-\tau}^i$ and the causal parents of every parent $\hat{P}(X_{t-\tau}^i)$ as determined by the PC algorithm. Only the parents that still show a significant partial correlation here are retained and correspond to the final set of causal parents, revealing the causal structure of the system. An advantage of the MCI algorithm, so conditioning on the causal parents of both X_t^j and $X_{t-\tau}^i$, is that autocorrelation is accounted for (Runge et al., 2019b), which reduces false positives and increases detection power (Runge, 2020).

MCI is in essence a multiple linear regression using the parents of each variable, derived in the PC step as independent variables (Kretschmer et al., 2016). Thus, the link strength can be thought of as a path coefficient and expresses the expected difference in standard deviations of a variable, also called an actor, given a change of 1 standard deviation in the parent (Kretschmer et al., 2016), whilst keeping all other parents identical (Di Capua et al., 2020b). A link strength of 0.2 going from X_{t-4}^1 to X_t^2 means

that a change of 1 standard deviation of causal parent X^1 at time t-4 leads to a change of 0.2 standard deviations of X^2 at time t. These results can be visualised using causal effect networks, which can be represented within schematic visualizations, oftentimes maps, of the studied system (Kretschmer et al., 2016; Di Capua et al., 2020b).

2.2.3.2   Assumptions and limitations of PCMCI

Causal inference methods are often based on a set of assumptions, some of which are: Time-order, that is the cause should precede the effect; Causal Sufficiency, all direct common drivers are included; and the Causal Markov Condition, where a variable is conditionally independent of other variables given its parents (direct causes). However, in more recent studies it was shown that PCMCI can still be applied even when these assumptions do not hold completely true (Runge et al., 2019a and 2019b) as is the case in complex systems like the atmosphere. Here, especially the Causal Sufficiency Assumption can hardly be fulfilled and therefore care should be taken when interpreting the results of PCMCI: Adding previously unobserved actors or removing actors might change causal networks. A further assumption is stationarity of the studied time series (Runge et al., 2019b), hence any trends and seasonality should first be removed as far as possible. Retention of some non-stationarity is not an issue however, as PCMCI has proven to deal with observations containing trends or seasonality (Runge et al., 2019b). Finally, Runge (2018) notes that the absence of a link is more robust than the presence of a link as it does not require the assumptions of Causal Sufficiency or the Causal Markov Condition. Further assumptions and limitations and how to deal with them are discussed in detail in Runge (2018) and Runge et al. (2019a and 2019b).

2.2.3.3   Testing PCMCI with generic data

To examine how PCMCI captures links from different lagged relationships, it was tested with various generic time series which should mirror different lagged dependencies. Two binary (0,1) step functions were created to which random noise was added to create two continuous time series, one termed R and the other *driver of R*. Slight modifications to the lags and patterns of increase and decrease in the time series allowed to test different scenarios for causal links and are outlined in the following section. All PCMCI runs used τ_{max} of 5 to inspect only the immediate lagged relationships at lags 4 and 2 and α_{PC} was set to 0.01. The Benjamini and Hochberg (1995) FDR test was applied to correct the p-values for multiple testing and limit FDR to 0.01. Only links significant at the 0.01 level after FDR are plotted.

PCMCI visualises causal network using so-called causal process graphs (Runge et al., 2019b), which consist of nodes and edges connecting the nodes (Figs. 6 and 7). Concretely, the nodes in the causal process graph represent each actor, i.e., time series in this case, and its colour shows the autocorrelation strength, measured by the autocorrelation path coefficient. The edges represent the statistically significant links between actors with the colour indicating the link strength, measured by the path coefficient. Time-lagged and therefore directional links (based on the assumption of time order) are represented by arrows. The time lags of these links are indicated by numbers overlaying the links. If actors are linked on multiple time lags, more than one number is shown, with the strongest link listed first. Note that the link colour is defined by the strongest link. For instantaneous links no direction can be assigned. Thus, instantaneous links are visualised as solid lines with nodes at each end (Fig. 6d).

In a first set of tests (Fig. 6), the links detected by PCMCI for changing lagged relationships between the *driver of R* and R were investigated. If the *driver of R* changes 4 timesteps before a change of R, i.e., at lag 4 (Fig. 6a), PCMCI correctly detects the link (Fig. 6b) with a link strength of 0.848. If the *driver of R* changes at lag 4 to a change of R but remains high while R is high (Fig. 6c), PCMCI correctly detects both the lagged link (Fig. 6d), although with reduced link strength 0.423, and the instantaneous relationship (link strength 0.446). Since PCMCI needs time order to direct causality (Runge et al., 2019b), there is no direction for the instantaneous link. If the *driver of R* changes at lag 4 to a change of R but remains high while R is high and beyond (Fig. 6e), the link is correctly detected (Fig. 6f), but with further reduced effect strength of 0.389. It should be noted that detected autocorrelation increased for each of the last three examples, as less of the variance in the values could be explain by the links between variables. If the *driver of R* changes at lag 4 to a change of R but in another instance also at lag 2 (Fig. 6g), PCMCI correctly detects both links (Fig. 6h). The link at time lag 2 has a larger effect strength (0.462) than the link at time lag 4 (0.380).

As mentioned above, in this work only changes of actors within DJF are investigated, whilst changes in driving variables at given lags might still come from other preceding months, in this case November. PCMCI offers a masking function to achieve this. In the next set of tests, this feature was investigated by separating the time series into a "winter" and "summer" season (Fig. 7). In a first example, *driver of R* changes at lag 4 to a change of *R* in "winter" and at lag 2 in "summer" (Fig. 7a). Without the masking function both links at lags 4 and 2 are detected and the causal network (not shown) is identical to the last example investigated above (Fig. 6h). However, using the PCMCI masking function to only consider changes during "winter", allows to correctly identify only the link at lag 4 (Fig. 7b). In the final example, *driver of R* again changes at lag 4 to a change of *R* in "winter" and at lag 2 in "summer". However, it now has a positive effect on *R* in "winter" and a negative effect in "summer" (Fig. 7c). Both links are detected if the model is not masked for "season" (Fig. 7d). However, due to the noise added to the series the positive link at lag 4 is slightly stronger (0.344) than the negative link at lag 2 (0.342) and thus the causal graph depicts a positive link and displays lags 4 and 2, despite the link at lag 2 being negative. If the season masking for "winter" is applied, the positive link at lag 4 with a strength of 0.848 is correctly detected (Fig. 7e). Vice versa, if masking for changes in "summer" only, the negative link with strength -0.870 at lag 2 is detected (Fig. 7f). This example shows that the causal graph can be misleading, as all significant links are plotted, but the colour of the link and thus the sign of the link is only taken from the strongest link (Fig. 7d). If this example was repeated but the negative link in "summer" acted at the same lag as in "winter", i.e., at lag 4, then the causal network for the whole year would not show any links, as they cancel out (not shown).

### 2.2.3.4 *Application of PCMCI to the drivers of RRWPs*

The following section provides an overview of how the PCMCI algorithm was used to quantify links between potential drivers of RRWPs and *R*. PCMCI was applied using *tigramite*, an open-source python package developed by Runge et al. (2019b), which allows to carry out and visualise PCMCI. The software and documentation are available at https://github.com/jakobrunge/tigramite/.

In a first step, the potential drivers and the time lags at which they influence RRWPs were identified based upon statistically significant areas in the composites and the regression maps and known links from the literature. Often many areas circumglobally show statistically significant signals. Hence, only areas which can also be linked to *R* via a physical mechanism or plausible hypothesis were considered. Once possible drivers and hypotheses on how they influence RRWPs have been defined, the drivers must be converted from gridded data into time series in an appropriate manner. One approach is to spatially average variables over regions (Kretschmer et al., 2016; Runge et al., 2019a). Furthermore, time-averaging can reveal the different timescales, on which each driver is acting (Kretschmer et al., 2016). The process of converting gridded data to time series is outlined in the following paragraph.

PCMCI requires times series of detrended anomalies as input data (Di Capua et al., 2020b). Therefore, for each timestep at each gridpoint, anomalies with regards to its seasonal climatology were calculated, thus removing the seasonal cycle. Next, time series were created from the gridded data by spatially averaging over the regions of interest. When calculating spatial averages, all the gridded data was weighted by the cosine of the latitude to adjust for spherical geometry and the thus decreasing size of grid cells towards the poles. For blocking, the anomaly of the fraction of area blocked was calculated. Here, for a region of interest, again applying the area weighting, the fraction of area blocked per timestep was calculated by dividing the area covered by blocking by the total area of the region of interest. From this value the seasonal mean fraction of area blocked was subtracted, thus receiving an anomaly of fraction of area blocked with regards to the seasonal mean fraction of area blocked for regions of interest. Finally, any linear trend in the time series was removed. As this work focuses on DJF, the masking function of PCMCI was used to ensure that only changes of variables within DJF are considered. Drivers acting at some time lag, however, might still come from other months, specifically November, as the highest time lag investigated in this study is 23 days (Tab. 1).
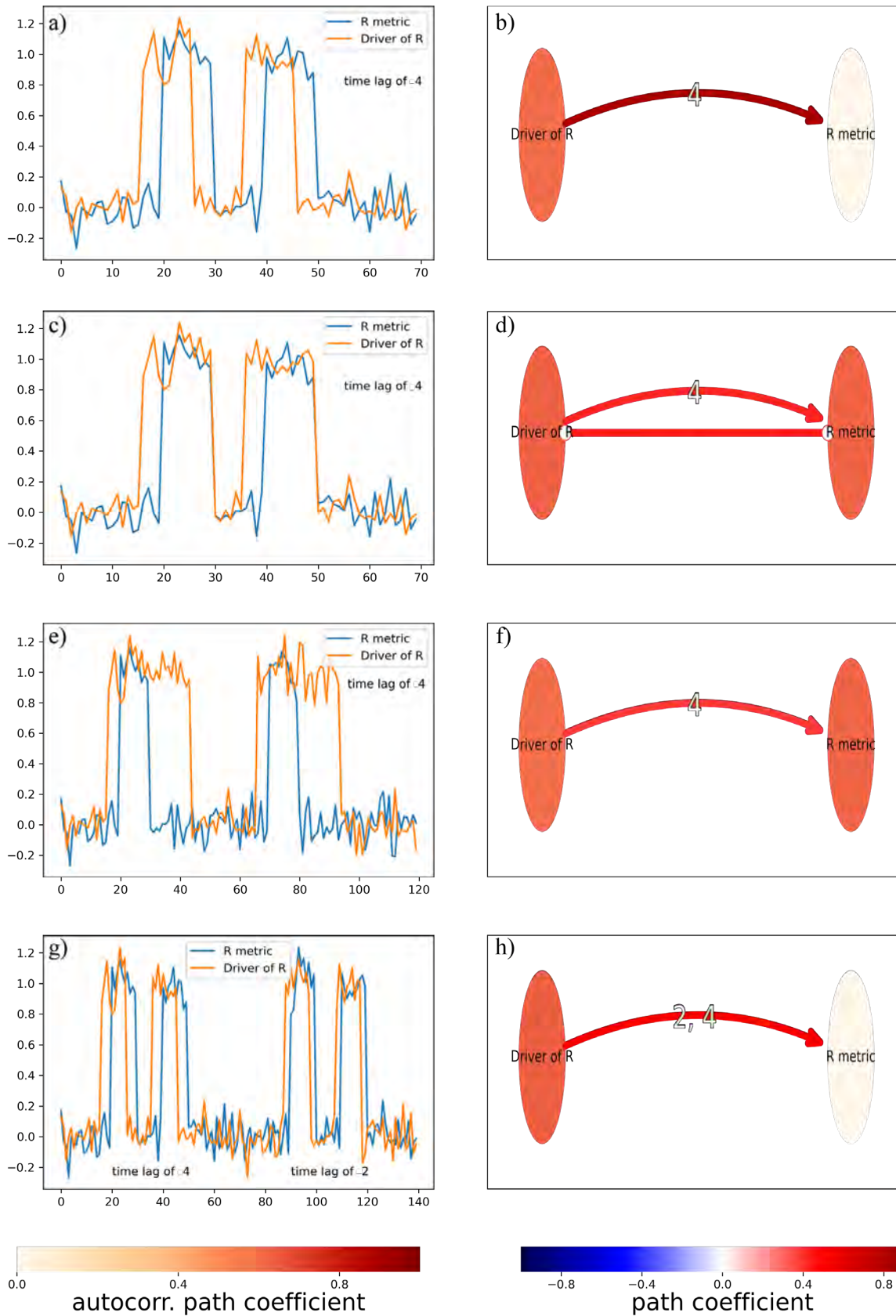
Figure 6: The panels in the left column a), c), e), and g) show generic time series of *R* (blue line) and *driver of R* (orange line). The time series are generated from binary (0,1) step functions with random noise added to each timestep to create a continuous time series. The panels in the right column b), d), f), and h) show the resulting causal networks. The node colour represents the autocorrelation path coefficient (autocorrelation strength) and the link colour indicates the path coefficient (link strength) and sign. Blue denotes a negative link and red a positive link. Note the different colour scales for nodes and links. The numbers written in white on the links in the causal network are the lags at which links were found. Directed links are visualised with arrows, whilst instantaneous links, where no direction of causality is derived, are visualised by lines with nodes at both ends as in panel d).
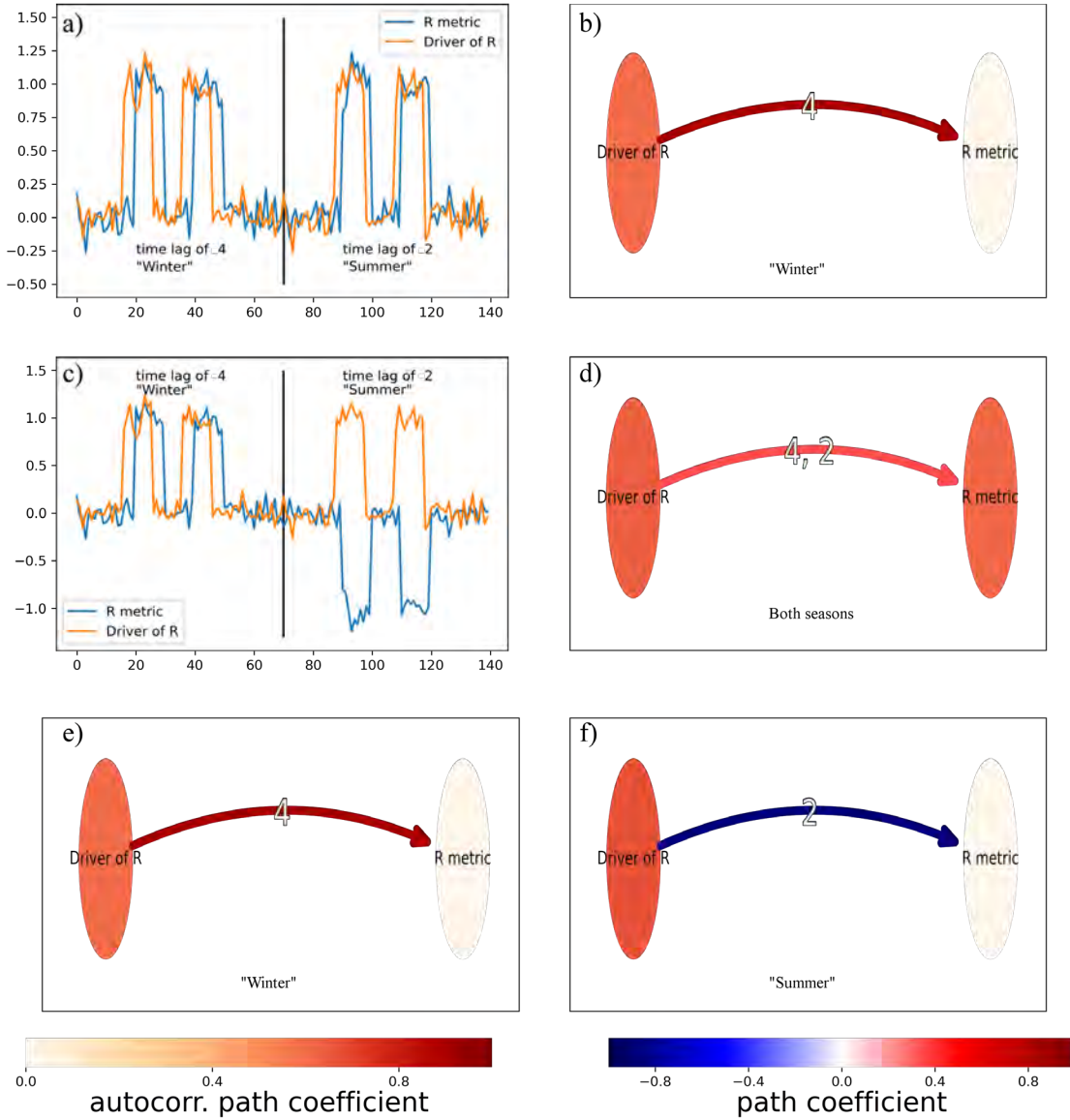
Figure 7: Generic time series a) and c) and resulting causal networks b), and d), e), f) respectively, as in Figure 6. Here the PCMCI season masking function is used to investigate only changes within a specific season.

PCMCI was run for three different time scales: Daily, 3-daily, and 6-daily. This approach can give insight into how actors influence each other on multiple time scales (Kretschmer et al., 2016) and whether the links change across timescales. Since RRWPs are synoptic-scale phenomena, it is expected that most links act within lags of maximum 1-2 weeks. To resample the daily data to 3 and 6-daily resolutions, only every 3rd or 6th timestep was retained and assigned the mean value of itself and the next 2, respectively 5 days for a total of 3, respectively 6 days which were averaged (Tab. 1).

The parameters τ_{max} (maximum time lag), α_{PC} (significance level for the PC algorithm), and α_{FDR} (significance threshold for the FDR corrected p-values) must be set in PCMCI. Kretschmer et al. (2016) found that changing the parameters τ_{max} and α_{PC} would change results, but sensitivity tests using different parameter choices and time scales yielded robust results. It is recommended to select τ_{max} according to the maximum physical time lag expected in the system and that a larger choice is usually better since the only downside is longer runtime (Kretschmer et al., 2016; Runge et al., 2019b). As PCMCI was run on daily, 3-daily, and 6-daily timescales, τ_{max} was adjusted accordingly from 20 for

daily data, to 6 for 3-daily, and 3 for 6-daily so that all PCMCI models investigate processes at lags within about 20 days (Tab. 1).

Table 1: Schematic representation of the time-averaging applied on the three different time scales. Each square is one time step for the respective model. Note that daily lags 19 to 23 are not shown.

daily	0	1	2	3	4	5	6	7	8	9	10	11	12	13	14	15	16	17	18
3-daily		0			1			2			3			4			5		6
6-daily			0						1						2				3

α_{PC} can be set by the user to a single value or determined from multiple values by selecting the best value based on the quality of the model it produces (Runge et al., 2019b; Di Capua et al., 2020). Runge et al. (2019b) note that α_{PC} should not be seen as a significance level, but rather as a "regularization parameter" as is used in model selection techniques. They further remark, that to low α_{PC} excludes too many true links during the PC stage, which can lead to false positives in the MCI stage, where these missing true links are not within the condition set. α_{PC} being too high on the other hand leads to lower detection power and higher runtime. Values between 0.01 and 0.05 were tested for α_{PC}. Higher values did tend to reveal more links, but overall, the links significant at a conservative significance level, i.e., 0.01, tended to be the strongest links and higher α_{PC} often only revealed additional lags to links which already existed (see Appendix A2.2 for sensitivity tests of α_{PC} for the eastern North Pacific model). Furthermore, since the tested time series here are rather long, a lower significance level is recommended (Kretschmer et al., 2016). Therefore, a conservative approach was favoured and α_{PC} set to 0.01 for all tests. This means that after the PC step, parents which are below 99 % significance will not be considered for the MCI stage. PCMCI also includes an FDR control (Runge et al., 2019b) and adjusts the p-values received after the MCI stage for multiple testing. In this work, the BH (Benjamini and Hochberg, 1995) correction was applied to constrain FDR to 0.01 and only links with adjusted p-values, $p_{k,adj,BH}$, significant at $\alpha_{FDR} = 0.01$ were retained.

3. Results and Discussion

In the following chapter, the results from the composites and regression analysis are presented and used to generate concrete hypotheses on areas possibly influencing R. Actors, i.e., time series, representing these areas are created by spatial averaging. The hypotheses are then tested in PCMCI by combining the actors in causal networks. Results are presented separately for the North Atlantic (3.1) and the eastern North Pacific (3.2) basins. Per basin, the results from the composites and regression analysis, and subsequently PCMCI, are also presented separately for each possible driver of R (blocking, changes in the background flow, and forcing from deep convection). Basin specific results regarding the drivers of R are discussed in 3.1.3 (R_{N-Atl}) and 3.2.3 (R_{NE-Pac}). A general discussion, limitations, and outlook are presented in section 3.3.

3.1 North Atlantic

3.1.1 Composites and regression analysis

3.1.1.1 *Atmospheric blocking*

Following the findings of Röthlisberger et al. (2019), I focus on atmospheric blocking within approximately 60° up - or downstream of changes in R. The blocking frequency composite at lag 0 days (Fig. 8c) reveals positive anomalies exceeding 9 % in the central North Atlantic and from Scandinavia into Siberia during high R days. The former are already visible, although extending over a smaller area, at lag 5 (Fig. 8b). Over Scandinavia and the western North Atlantic, however, negative anomalies up to -7 % occur at lags 10 and 5 (Figs. 8a and 8b). The regression analysis reveals a similar pattern. At lag 0 and 3 (Figs. 9c and 9b), blocking in the central North Atlantic is associated with an increase in R, whilst at lag 10 (Fig. 9a) there is a negative relationship between blocking over Scandinavia and R. High R days in the North Atlantic are characterized by positive blocking frequency anomalies in the central North Atlantic and a reversal from negative blocking frequency anomalies leading up to high R days to positive blocking frequency anomalies during high R days over Scandinavia. Therefore, actors representing North Atlantic blocking ($blocks_{N-Atl}$, Tab. 2) and Scandinavian blocking ($blocks_{Scand}$, Tab. 2) were created to test their links to R_{N-Atl}.
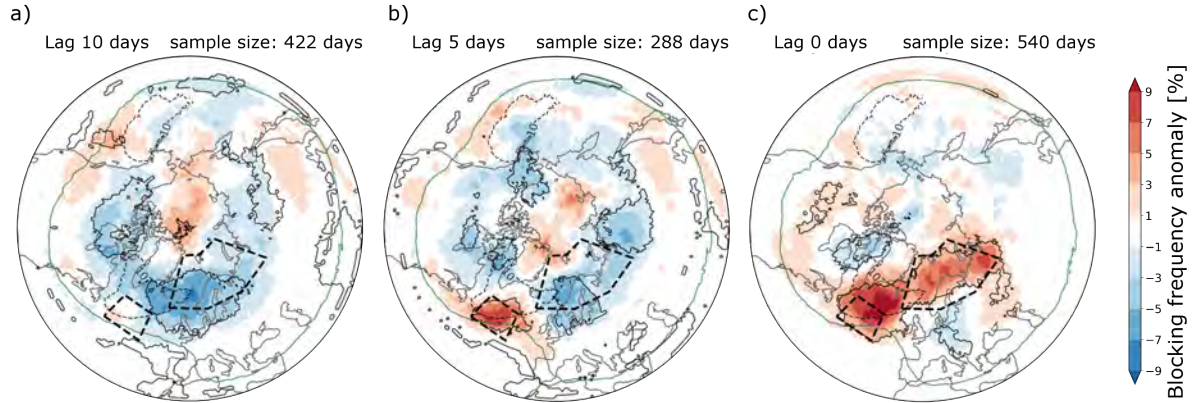
Figure 8: Composite of atmospheric blocking frequency anomalies leading up to high R days in the North Atlantic at lag a) 10 days, b) 5 days, and c) 0 days, i.e., during high R days. The green line shows the composite 2 PVU line on the 320 K isentrope as a proxy of the jet. Black dashed lines denote the 10 % DJF climatological blocking frequency. Statistically significant blocking frequency anomalies at α = 0.01 are marked by black solid lines. The spatial extent of $blocks_{N-Atl}$ (at 50° N and 35° W) and $blocks_{Scand}$ (at 70° N and 40° E) is indicated by rectangles of black dashed lines.
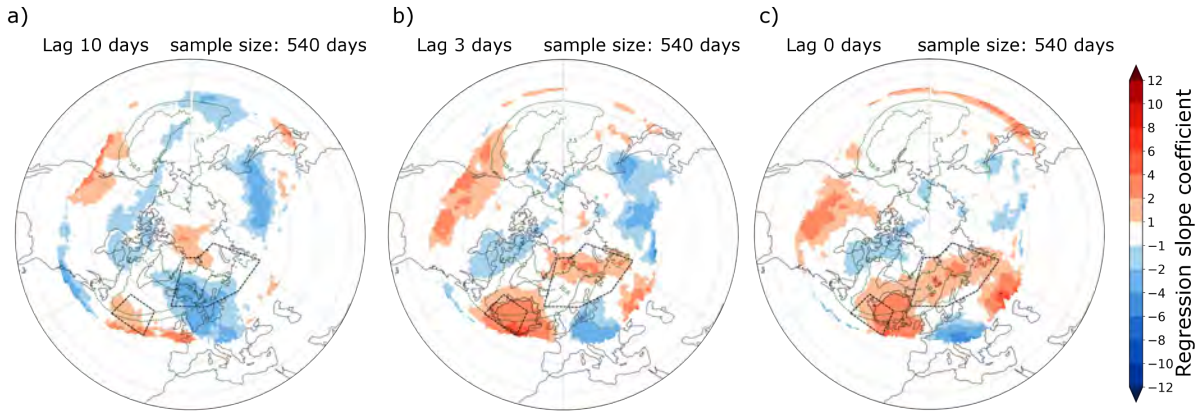
Figure 9: The slope coefficient β_1 of a regression of R_{N-Atl} on blocks displaying the mean expected change in R_{N-Atl} between presence or absence of a block per gridpoint at lag a) 10 days, b) 3 days, and c) 0 days. The green dashed lines denote the 7.5 % and 10 % DJF climatological blocking frequency. Areas where β_1 is significantly different from 0 at the 0.01 and 0.05 significance level are marked by black solid lines. Areas where the seasonal blocking frequency is ≤ 0.01 % are not shown. The spatial extent of $blocks_{N-Atl}$ (at 50° N and 35° W) and $blocks_{Scand}$ (at 70° N and 40° E) is indicated by rectangles of black dashed lines.

3.1.1.2 Changes in the background flow

From the $U250_{wvnf\,k0k3}$ anomaly composites two features of the background flow over the North Atlantic are evident prior to and during high R days (Fig. 10). Firstly, a reversal from positive anomalies up to 4 m s^{-1} 10 days before high R days (Fig. 10a) to negative anomalies up to -6 m s^{-1} during high R days (Fig. 10c) over north-western Europe (around 53°N and 0° W° E) over the exit of the climatological jet. This matches the negative blocking frequency anomalies leading up to high R-days (Fig. 8a) with presumably more zonal flow, and then blocked flow and weaker background flow during high R days (Fig. 8c). Secondly, large negative anomalies up to -6 m s^{-1} over the entire North Atlantic (around 40° N and 40° W) during high R days (Fig. 10c) are found. The onset of these anomalies is rapid, as they are barely discernible 3 days before high R days (Fig. 10b). The regression analysis (not shown) displays both features as well, however with reduced magnitude and not always statistically significant. Both these features were investigated in PCMCI: $U250_{wvnf\,k0k3}$ anomalies averaged over north-western Europe ($U250_{N-Eu}$; Tab. 2) were analysed to test the connection of the reversal of the background flow to R_{N-Atl} and $U250_{wvnf\,k0k3}$ anomalies averaged over the North Atlantic ($U250_{N-Atl}$; Tab. 2) were analysed to test the link between the substantial decrease in the background flow and R_{N-Atl}.
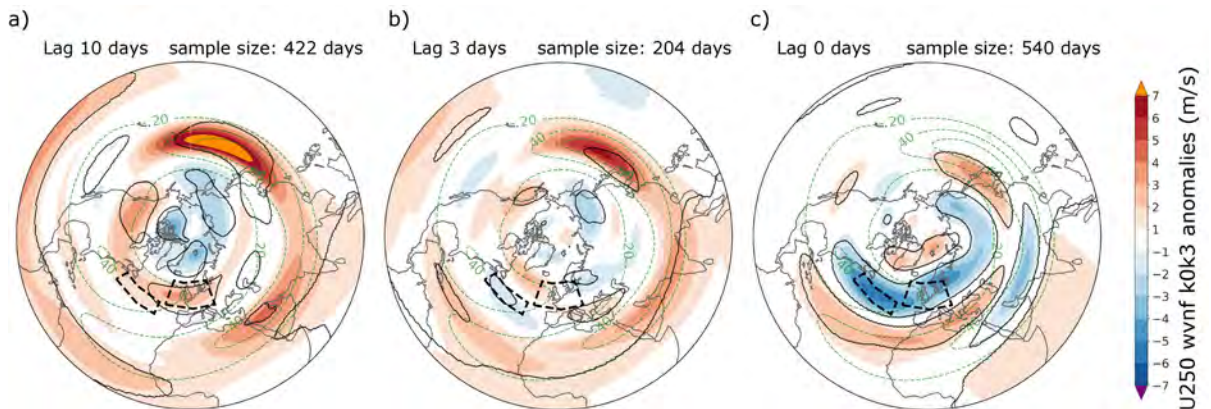

Figure 10: Composite of $U250_{wvnf\,k0k3}$ anomalies leading up to high R days in the North Atlantic at lag a) 10 days, b) 3 days, and c) 0 days, i.e., during high R days. Green dashed lines denote the DJF $U250_{wvnf\,k0k3}$ climatology at 20 m s^{-1} intervals starting at 20 m s^{-1}. Statistically significant $U250_{wvnf\,k0k3}$ anomalies at α = 0.01 are marked by black solid lines. The spatial extent of $U250_{N-Eu}$ (at 52° N and 0° W) and $U250_{N-Atl}$ (at 42° N and 40° W) is indicated by rectangles of black dashed lines.

20

3.1.1.3   Forcing from deep convection

The role (tropical) deep convection can play in modulating the extratropical flow field has been discussed in section 1.3.3. Here, specific hypotheses regarding the role of deep convection relating to RRWPs over the North Atlantic (R_{N-Atl}) shall be discussed. The composites and regression analysis for lag 0 (Figs. 11a, 12a, and 12b) reveal statistically significant overlapping OLR and VP anomalies (up to -8 W m^{-2} and -1x10^6 m^2 s^{-1} respectively) over western Africa around the Gulf of Guinea during high R days, indicating enhanced convection in this area. Therefore, an actor representing OLR anomalies over the Gulf of Guinea, $OLR_{Gulf-Guinea}$ (Tab. 2), was created. However, as these anomalies occur during high R days and geographically downstream of R_{N-Atl}, it is unlikely that this convection is a precursor to RRWPs in the North Atlantic. The lagged OLR and VP composites show statistically significant negative anomalies over the Maritime Continent between lags 3 and 20 with largest values at lags 10 (exceeding -14 W m^{-2} and -1x10^6 m^2 s^{-1} respectively; Fig. 11b) and 15 (not shown). Convection in this area can trigger RWs (Röthlisberger et al., 2018) which can propagate over the Pacific and can force extratropical flow in the Atlantic (Hoskins and Sardeshmukh, 1987; Cassou, 2008; Barton et al., 2016). Therefore, an actor for convection over the Maritime Continent, $OLR_{Marit-cont}$ (Tab. 2), was created.
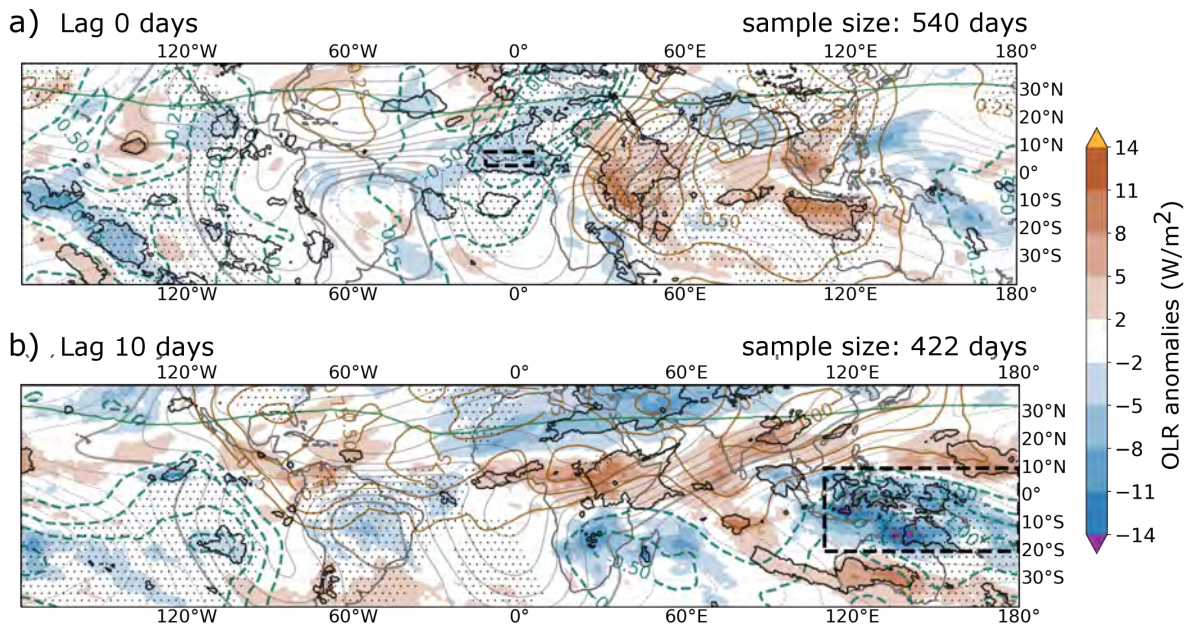
Figure 11: Composite of OLR (shaded) and VP anomalies (coloured contours at 0.25x10^6 m^2 s^{-1} intervals, green dashed lines denote negative values, brown solid lines denote positive values) and absolute VP values (grey contours at 1x10^6 m^2 s^{-1}, solid lines denote positive values, dashed lines denote negative values) a) during high R days and b) at lag 10 before high R days in the North Atlantic. Statistically significant anomalies are marked by black contours for OLR and by hatches for VP. The spatial extent of a) $OLR_{Gulf-Guinea}$ (at 5° N and 5° W) and b) $OLR_{Marit-cont}$ (at 5° S and 150° E) is indicated by rectangles of black dashed lines.
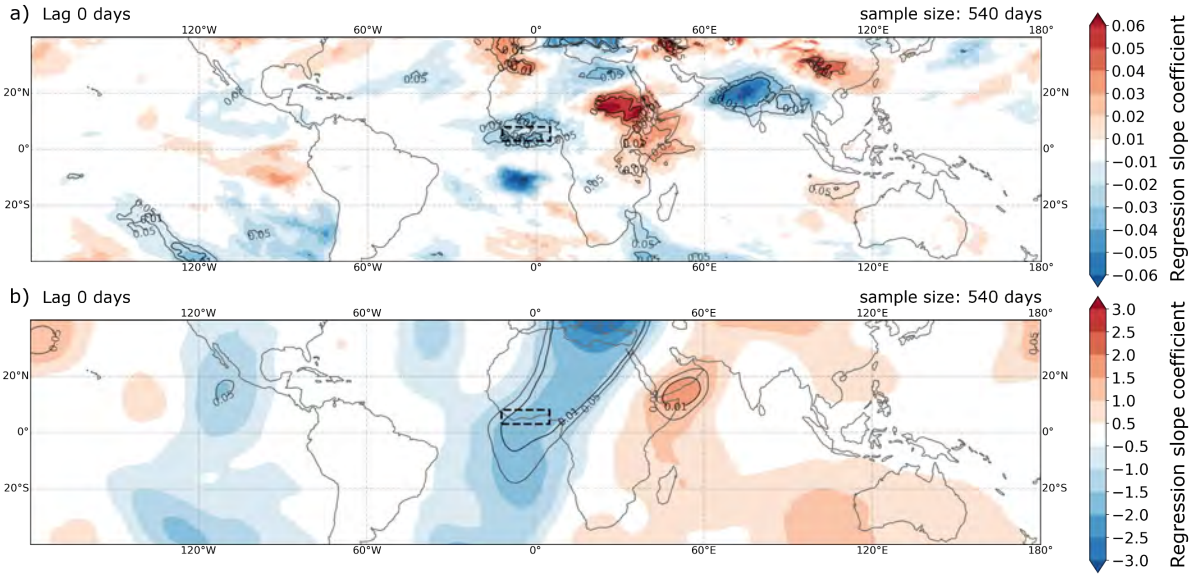
Figure 12: The slope coefficient β_1 of a regression of R_{N-Atl} on a) OLR at lag 0 and b) VP at lag 0. Shadings display the expected change in R_{N-Atl} for each a) 1 W m^{-2} change in OLR or b) 1x10^7 m^2 s^{-1} change in VP. Areas where β_1 is significantly different from 0 at the 0.01 and 0.05 significance level are marked by black solid lines. The spatial extent of $OLR_{Gulf-Guinea}$ (at 5° N and 5° W) is indicated by a rectangle of black dashed lines.

3.1.2 PCMCI

In summary, the following actors were created and analysed in a causal network for the North Atlantic at three different time scales (Figs. 13-15): R_{N-Atl}, $blocks_{N-Atl}$, $blocks_{Scand}$, $U250_{N-Eu}$, $U250_{N-Atl}$, $OLR_{Gulf-Guinea}$, and $OLR_{Marit-cont}$ (Tab. 2). In the following section the results from PCMCI are presented separately for each possible driver (atmospheric blocking, changes in the background flow, and forcing from deep convection) before they are discussed in section 3.1.3. Remember that the causal link strength given by PCMCI is in units of standard deviation (Kretschmer et al., 2016). The standard deviation of each time series is included in the tables describing the relevant actors for each ocean basin (Tabs. 2 and 3). Shown causal graphs follow the conventions described in section 2.2.3.3 and Figs. 6 and 7. In the text, links between actors are formulated in the following notation:

$$process\ 1_{area\ 1} \xrightarrow[\tau]{} process\ 2_{area\ 2}$$

, where τ denotes the time lag at which links were detected. Links strengths are given in brackets ().

3.1.2.1 Atmospheric blocking

PCMCI (Figs. 13-15) finds a close link between $blocks_{N-Atl}$ and R_{N-Atl}. There is a positive link $blocks_{N-Atl} \rightarrow R_{N-Atl}$ at lag of around one week. This link occurs in the daily model (Fig. 13) at lag 7 (0.074), in the 3-daily model (Fig. 14) at lag 2 (0.108), and is instantaneous in the 6-daily model (0.166; Fig. 15). Note that the link $blocks_{N-Atl} \xrightarrow[\tau=8]{} R_{N-Atl}$ in the daily model is negative (-0.066).

The reverse link, $R_{N-Atl} \rightarrow blocks_{N-Atl}$, is less consistent across time scales. The daily model shows a negative link at lag 8 (-0.073), but in the 3-daily model the link is positive at lag 1 (0.131). Generally, North Atlantic blocking and RRWPs positively reinforce each other. The negative influence of blocking over Scandinavia ($blocks_{Scand}$) on R_{N-Atl} is also captured by the model. At lag 7 in the daily model (-0.069) and at lag 2 in the 3-daily model (-0.101) there is a negative link $blocks_{Scand} \rightarrow R_{N-Atl}$. Finally, $blocks_{N-Atl}$ drives an increase in $blocks_{Scand}$. The daily model shows positive links at lags 2,3 (0.062, 0.061), with links at lag 1 in the 3-daily (0.107) and 6-daily model (0.145). Overall, it is concluded that R_{N-Atl} and $blocks_{N-Atl}$ reinforce each other and that a decrease in $blocks_{Scand}$, i.e., a more zonal or cyclonic flow, precedes RRWPs. Further, the increase in $blocks_{N-Atl}$ associated with RRWPs might also increase $blocks_{Scand}$ during RRWP episodes.

Table 2: List of actors in the causal networks for R in the North Atlantic.

Abbreviation	Actor	Variable [unit]	Region	Standard deviation
R_{N-Atl}	RRWPs in the North Atlantic	R [m s^{-1}]	35° N - 65° N, 50° W - 10° E	3.08
$blocks_{N-Atl}$	Blocking over the North Atlantic	Fraction of area blocked [%]	46° N - 56° N, 45° W - 25° W	0.17
$blocks_{Scand}$	Blocking over Scandinavia		60° N - 80° N, 15° W - 70° E	0.11
$U250_{N-Eu}$	Background flow over north-western Europe	Zonal wind U at 250 hPa, filtered for wavenumbers k 0-3 [m s^{-1}]	45° N – 60° N, 20° W – 20° E	9.42
$U250_{N-Atl}$	Background flow over the North Atlantic		38° N – 45° N, 60° W – 25° W	10.91
$OLR_{Gulf-Guinea}$	Convection over the Gulf of Guinea	Outgoing longwave radiation [W m^{-2}]	3° N - 8° N, 12° W - 5° E	19.98
$OLR_{Marit-cont}$	Convection over the Maritime Continent		20° S – 10° N, 110° E – 180° E	10.19

3.1.2.2 Changes in the background flow

Negative feedback between R_{N-Atl} and $U250_{N-Eu}$ at timescale of about 1 week is found. $U250_{N-Eu}$ increases R_{N-Atl}, which in turn decreases $U250_{N-Eu}$. A positive link $U250_{N-Eu} \rightarrow R_{N-Atl}$ is present in the daily model (Fig. 13) at lag 7 (0.076) and in the 6-daily model (Fig. 15) at lag 1 (0.140), whilst a negative link $R_{N-Atl} \rightarrow U250_{N-Eu}$ is present on all three timescales (-0.108 at lag 7, -0.138 at lag 2, and -0.149 at lag 1 for the daily, 3-daily, and 6-daily models). This confirms the hypothesis that a strong background flow causes an increase in R_{N-Atl} about a week later, which then decreases the strength of the background flow. Furthermore, $U250_{N-Eu}$ is strongly negatively linked to $blocks_{Scand}$. An instantaneous link is present at all time scales (-0.125, -0.296, -0.347, for the daily, 3-daily, and 6-daily model). In the daily and 3-daily model (Figs. 13 and 14) negative links $U250_{N-Eu} \underset{\tau=1}{\longrightarrow} blocks_{Scand}$ with strength -0.126 and -0.124 respectively are found. However, in the daily model a positive link $U250_{N-Eu} \underset{\tau=2}{\longrightarrow} blocks_{Scand}$ (0.075) is also found, showing the high variability in links at the daily scale. Overall, the negative instantaneous link between $U250_{N-Eu}$ and $blocks_{Scand}$ and the negative link $U250_{N-Eu} \underset{\tau=1}{\longrightarrow} blocks_{Scand}$ indicate that a decrease in background flow is strongly connected to an increase in the local blocking. Furthermore, the increase in $blocks_{Scand}$ seen during high R days (Figs. 8c and 9c) can be explained via the negative effect of R_{N-Atl} on $U250_{N-Eu}$. A decrease in $U250_{N-Eu}$ then causes an increase in $blocks_{Scand}$. Finally, PCMCI shows direct negative feedback between $U250_{N-Eu}$ and R_{N-Atl} where an increase in $U250_{N-Eu}$ increases R_{N-Atl}, which in turn causes lower $U250_{N-Eu}$.

R_{N-Atl} drives a decrease in $U250_{N-Atl}$ at a lag of about half a week. There is a negative link $R_{N-Atl} \xrightarrow[\tau=1]{} U250_{N-Atl}$ (-0.117) in the 3-daily model (Fig. 14), whilst the link is instantaneous in the 6-daily model (-0.137; Fig. 15). However, a positive link $R_{N-Atl} \xrightarrow[\tau=3]{} U250_{N-Atl}$ (0.100) was also found the 3-daily model, showing that R_{N-Atl} can also have a positive effect on the strength of the background flow at higher lags. Furthermore, $U250_{N-Atl}$ is closely linked to $blocks_{\text{N-Atl}}$. In the daily model, $U250_{N-Atl}$ negatively influences $blocks_{N-Atl}$ at lags 1 (-0.165), whilst $blocks_{N-Atl}$ negatively influences $U250_{N-Atl}$ at lag 1 (-0.079). The two actors are also connected by a negative instantaneous link at all time scales (-0.190, -0.371, -0.495, in the daily, 3-daily, and 6-daily model respectively). Both in the 3-daily and 6-daily model a negative link $U250_{N-Atl} \xrightarrow[\tau=1]{} blocks_{N-Atl}$ is present. In the daily model, the link $U250_{N-Atl} \xrightarrow[\tau=2]{} blocks_{N-Atl}$ is positive (0.096), again showing the high variability in links at the daily scale. $U250_{N-Eu}$ and $U250_{N-Atl}$ share a negative respectively positive instantaneous link in the daily and 6-daily model (Figs. 13 and 15), whilst links $U250_{N-Eu} \xrightarrow[\tau=1,2]{} U250_{N-Atl}$ (0.138 and -0.131) are detected in the daily model (Fig. 13).

3.1.2.3   *Forcing from deep convection*

Remember, that since negative OLR anomalies represent enhanced convection, a negative link away from OLR corresponds to a mechanism, where increasing convection causes an increase in another and vice versa. R_{N-Atl} drives a decrease in $OLR_{Gulf-Guinea}$, and hence an increase in convection, at a lag of about one week. The link is at lag 2 (-0.120) in the 3-daily model (Fig. 14) and at lag 1 (-0.140) in the 6-daily model (Fig. 15). Thus, the anomalous convection over the Gulf of Guinea is driven by RRWPs. Moreover, the background flow influences $OLR_{Gulf-Guinea}$, as $U250_{N-Eu}$ drives $OLR_{Gulf-Guinea}$ with about weekly lag at all time scales and is connected instantaneously in the 3 and 6 daily models. No direct links were found between $OLR_{Marit-cont}$ and R_{N-Atl}. However, $OLR_{Marit-cont}$ has a negative instantaneous link to $U250_{N-Atl}$ in the daily and 3-daily model (Figs. 13 and 14) and thus through $U250_{N-Atl}$ and $blocks_{N-Atl}$ an indirect link to R_{N-Atl} is present. Further, $OLR_{Marit-cont}$ is linked to $OLR_{Gulf-Guinea}$, however the link varies or disappears with changing time scales.
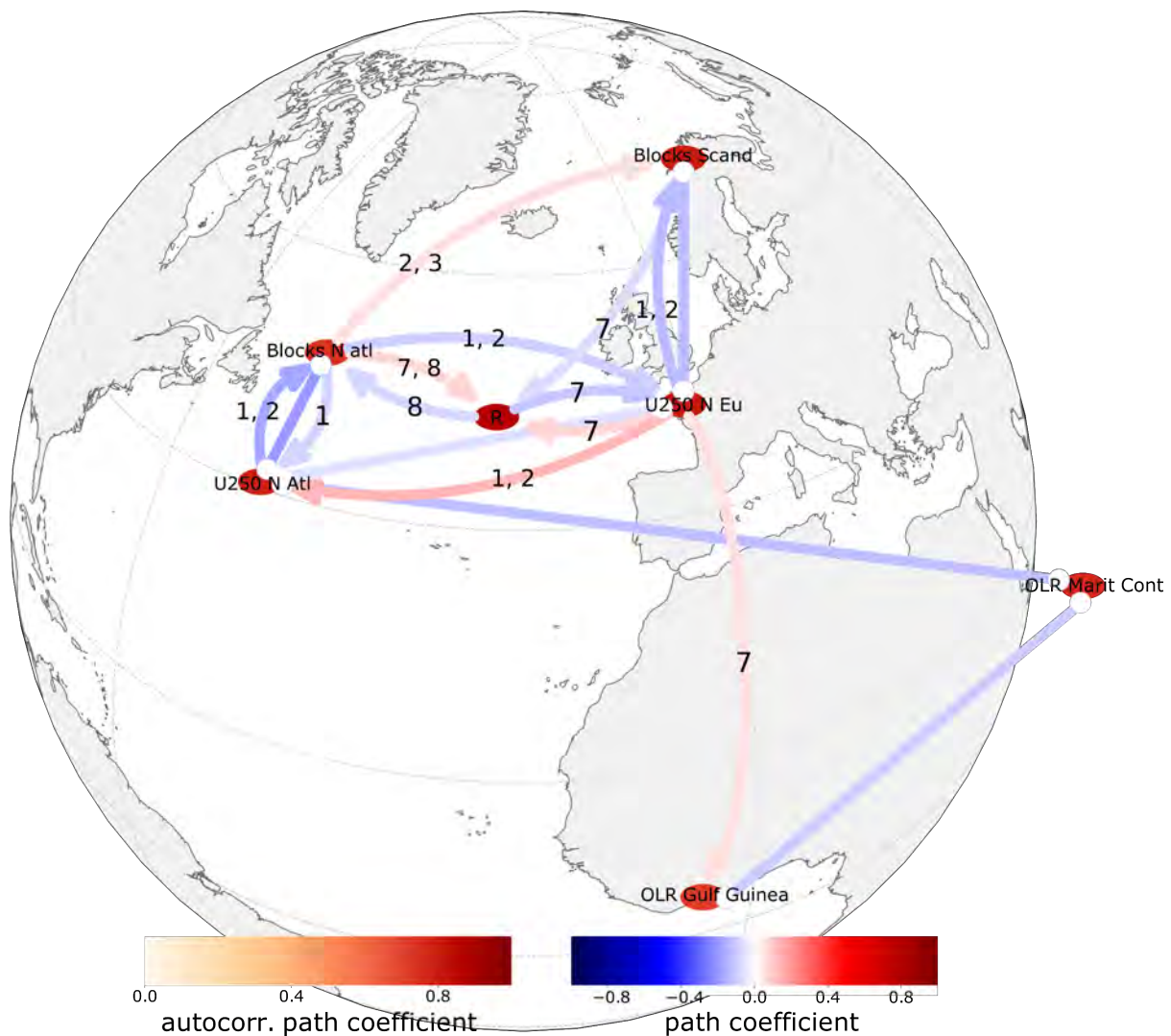
Figure 13: Causal network for the North Atlantic at daily time scale. The actors are centred on their approximate location. Symbols and colour scales are as in Fig. 6: The node colour represents the autocorrelation path coefficient (autocorrelation strength) and the link colour indicates the path coefficient (link strength) and sign. Blue denotes a negative link and red a positive link. Note the different colour scales for nodes and links. The numbers written in black on the links are the lags at which links were found. Note that the time lags refer to time steps for that specific model (see Tab. 1), e.g., for this model at daily time scale lags refer to days, whilst the model in Fig. 14 is at 3-daily time scale and thus lags refer to 3-day time steps. Directed links are visualised with arrows, whilst instantaneous links, where no direction of causality is derived, are visualised by lines with nodes at both ends, as the negative link $OLR_{Gulf-Guinea} \leftrightarrow OLR_{Marit-Cont}$ in this figure.
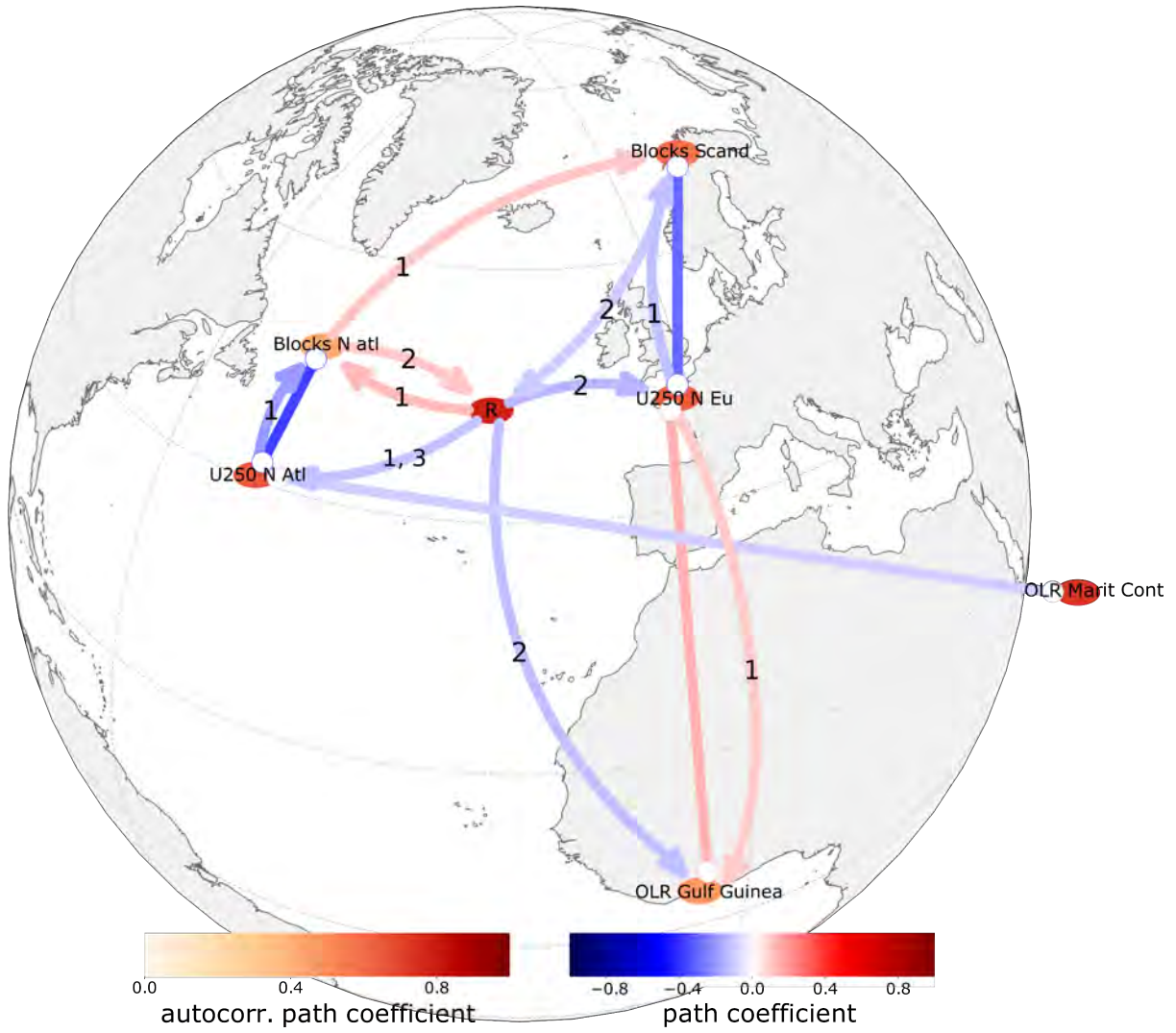
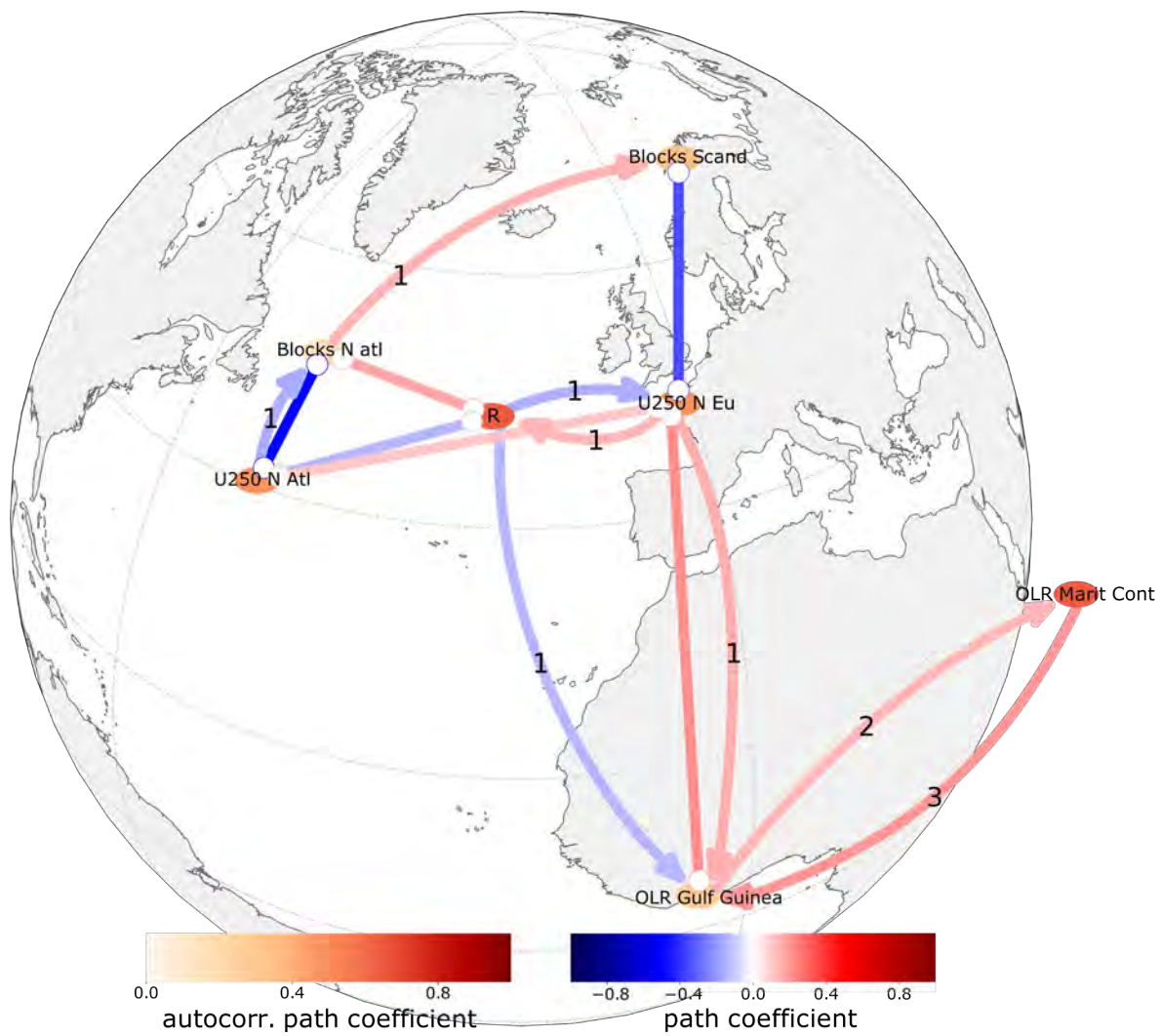**Figure 14: As Figure 13, but at 3-daily time scale.**

Figure 15: As Figure 13, but at 6-daily time scale.

3.1.3 Discussion

In the following section the results regarding drivers of R_{N-Atl} are discussed. Overall, a consistent pattern for the links between R_{N-Atl}, blocking, and the background flow is found, where R_{N-Atl} decreases the magnitude of the background flow, causing an increase the local blocking, which in turn affects R_{N-Atl} (Figs. 13-15). This is partially in agreement with Nakamura and Huang's (2017) findings on the relationship between high-frequency transient wave trains and a local deceleration of the background flow. Their interaction leads to wave convergence and large amplitude, i.e., wavey, flow and even blocking like patterns, a phenomenon already described by Shutts (1983).

More concretely, a change in atmospheric blocking is an important driver of R_{N-Atl}, with $blocks_{N-Atl}$ increasing R_{N-Atl} and a decrease in $blocks_{Scand}$ increasing R_{N-Atl}, both at weekly time lag (Figs. 13 and 14). Note that whilst $blocks_{N-Atl}$ is located geographically within the longitudes which define R_{N-Atl}, it is at the western, i.e., upstream, edge of the area denoting R_{N-Atl} (see Appendix A3.1). This confirms the hypothesis formulated by Röthlisberger et al. (2019), whereas blocking upstream, in this case $blocks_{N-Atl}$, can cause phasing of RWs downstream, thus causing RRWPs. The effect of R_{N-Atl} on $blocks_{N-Atl}$ is less clear, however, as the change from negative link in the daily model to positive link in the 3-daily model shows. Finally, the links from $blocks_{Scand}$ and $U250_{N-Eu}$ to R_{N-Atl} show that a more zonal flow regime over Scandinavia and north-western Europe can increase R_{N-Atl}, which then causes a less zonal and more blocked flow in that region (Figs. 13-15). The negative effect of $blocks_{Scand}$ on R_{N-Atl} might be linked to the preferred transition of the weather regimes in the North Atlantic. After a zonally oriented flow regime, qualitatively like the negative blocking anomalies 10 and 5 days before high R days (Figs. 8a and 8b), transitions into an Atlantic Ridge or Scandinavian blocking regime are most likely (Vautard, 1990; Cassou, 2008).

$OLR_{Marit-cont}$ is not a driver of RRWPs over the North Atlantic as no direct link to R_{N-Atl} was found. This does not exclude convection in this area as a driver for RRWPs in single cases or in season other than DJF, as the event in November 2002 studied by Barton et al. (2016) shows. An open question remains the instantaneous, negative link $OLR_{Marit-cont} \leftrightarrow U250_{N-Atl}$ at daily and 3 daily resolutions (Figs. 13 and 14). It is possible that this link results from a missing common or intermediary driver, e.g., a change in $U250_{N-Atl}$ causing a downstream effect which interacts with $OLR_{Marit-cont}$.

In addition to possible drivers of R_{N-Atl}, the causal network reveals that R_{N-Atl} acts as a driver of many processes. How R_{N-Atl} influences the background flow has been discussed above. R_{N-Atl} was further found to drive $OLR_{Gulf-Guinea}$. An increase in R_{N-Atl} causes lower $OLR_{Gulf-Guinea}$ values and hence increases convection directly (Figs. 14 and 15) or via $U250_{N-Eu}$ (Figs. 13-15). This might be related to eddy-mean flow interactions, where wave breaking associated with RRWPs distributes wave energy meridionally into the tropics (Wirth et al., 2018) and thus reinforces the tropical meridional circulation. Concretely, the large wave activity associated with high amplitude breaking RWs in RRWPs strengthen the so-called *residual* circulation (Vallis, 2007, p. 305), a thermally direct circulation with rising motion in the tropics. Wave breaking occurs when large amplitude RWs, as found in RRWPs, reach critical latitudes and break (Wolf and Wirth, 2017; Wirth et al., 2018). The associated wave energy is distributed meridionally and can strengthen the tropical meridional circulation triggering convection in the tropics (Slingo, 1998; Knippertz, 2007).
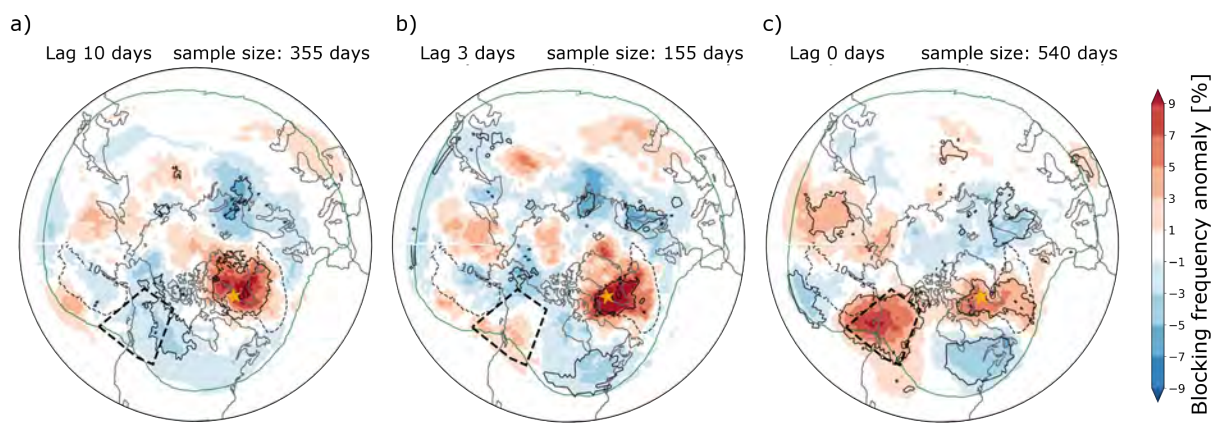
3.2 Eastern North Pacific

3.2.1 Composites and regression analysis

3.2.1.1 Atmospheric blocking

As for the North Atlantic, I follow Röthlisberger et al. (2019) regarding their results connecting R anomalies to blocking and focus on blocking within $60°$ up-or downstream of changes in R. Two main features are highlighted by the composites and regression analysis: Increased blocking frequency over the west coast of North America during high R days and increased blocking frequency over Greenland leading up to high R days. Both shall be discussed briefly. The composite of blocking frequency during high R days (Fig. 16c) shows positive anomalies exceeding 9 % over the west coast of North America ($53°$ N, $130°$ W) and exceeding 7 % over the area around Greenland ($65°$ N, $60°$ W), where blocking is

climatologically already frequent (>10 %). Leading up to high R days the blocking frequency anomalies over Greenland exceed 9 % over large areas (Figs. 16a and 16b). The regression confirms this (Fig. 17). Whilst blocking over the west coast of North America is the main signal during high R days (Fig. 17c), an increase in Greenland blocking at higher lags is linked to an increase in R (Figs. 17a and 17b). The composites also show other areas which exhibit positive or negative blocking frequency anomalies. However, these are weaker and not captured by the regression (Fig. 17) and are therefore not considered as potential drivers of RRWPs. An actor representing blocking over the west coast of North America ($blocks_{NA-wcoast}$) was created to test, whether RRWPs in the eastern North Pacific (R_{NE-Pac}) cause the increase in blocking. The blocking signal over Greenland is qualitatively alike the Atlantic European weather regime *Greenland blocking* (GL), as defined by Grams et al. (2017). Thus, an actor based on the GL index was used to characterize blocking over Greenland ($blocks_{WR-GL}$) to test if $blocks_{WR-GL}$ cause RRWPs in the eastern North Pacific. See Appendix A3.2 for a comparison of PCMCI analyses using $blocks_{WR-GL}$ and an actor based on fraction of area blocked.
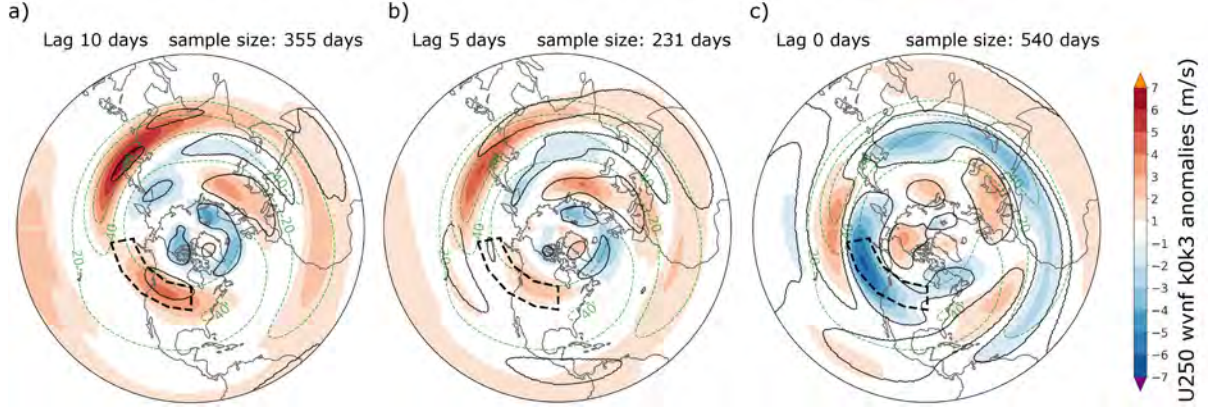

Figure 16: Composite of atmospheric blocking frequency anomalies as Figure 8, but leading up to high R days in the eastern North Pacific at lag a) 10 days, b) 3 days, and c) 0 days, i.e., during high R days. The spatial extent of $blocks_{NA-wcoast}$ (at 55° N and 125° W) is indicated by a rectangle of black dashed lines and the approximate area of the maximum 500 hPa geopotential height anomaly characterising $blocks_{WR-GL}$ as defined by Grams et al. (2017) is highlighted with an orange star (at 67° N and 54° W).
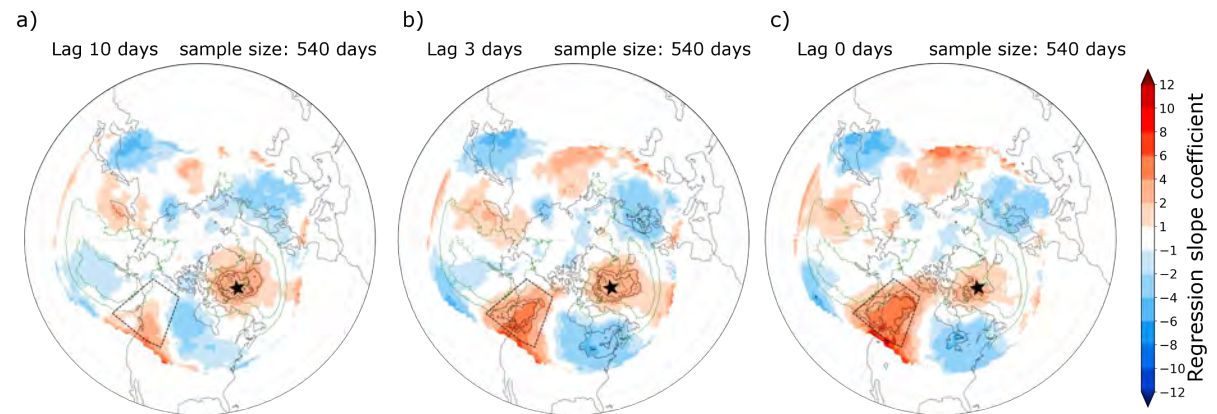
**Figure 17: As Figure 9 but for a regression of R_{NE-Pac} on blocks. The spatial extent of $blocks_{NA-wcoast}$ (at 55° N and 125° W) is indicated by a rectangle of black dashed lines and the approximate area of the maximum 500 hPa geopotential height anomaly characterising $blocks_{WR-GL}$ as defined by Grams et al. (2017) is highlighted with a black star (at 67° N and 54° W).**

29

3.2.1.2 *Changes in the background flow*

The background flow over the eastern North Pacific is characterized by a reversal from positive anomalies up to 5 m s^{-1} before high R days (Figs. 18a and 18b) to large negative anomalies reaching -7 m s^{-1} over the entire region during high R days (Fig. 18c). The regression analysis (Fig. 19) confirms this pattern, albeit with a weaker positive signal before changes in R (Figs. 19a and 19b). Therefore, $U250_{wvnf\,k0k3}$ anomalies averaged over the eastern North Pacific and western North America ($U250_{NE-Pac}$; Tab. 3) were analysed in PCMCI to test the connection of the reversal of the background flow to R_{NE-Pac}.

Figure 18: As Figure 10, but composite of $U250_{wvnf\,k0k3}$ anomalies leading up to high R days in the eastern North Pacific at lag a) 10 days, b) 5 days, and c) 0 days, i.e., during high R days. The spatial extent of $U250_{NE-Pac}$ (at 150° W) is indicated by a rectangle of black dashed lines.
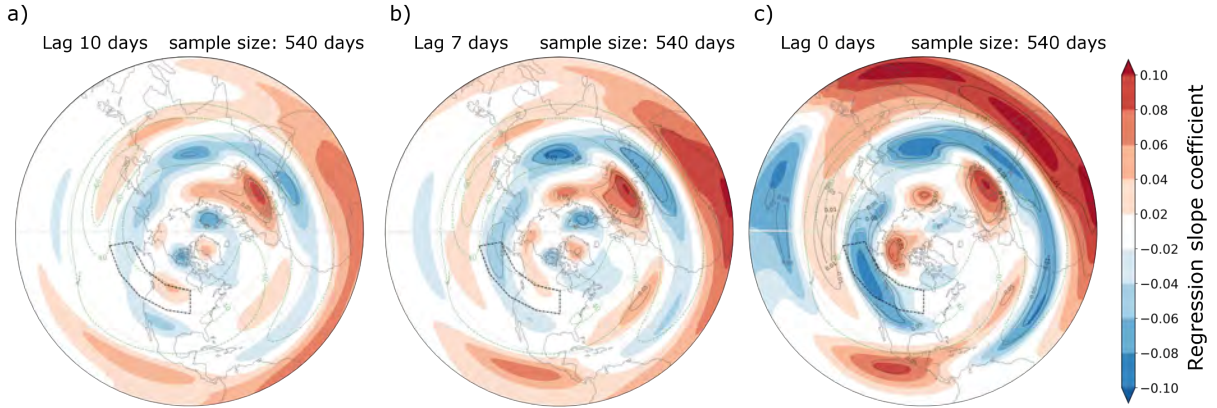
Figure 19: The slope coefficient β_1 of a regression of R_{NE-Pac} on $U250_{wvnf\,k0k3}$ at lag a) 10 days, b) 7 days, and c) 0 days. Shadings display the expected change in R_{NE-Pac} for each 1 m s^{-1} change in $U250_{wvnf\,k0k3}$. Areas where β_1 is significantly different from 0 at the 0.01 and 0.05 significance level are marked by black solid lines. The spatial extent of $U250_{NE-Pac}$ (at 150° W) is indicated by a rectangle of black dashed lines.

3.2.1.3 *Forcing from deep convection*

The composites and the regression analysis of OLR and VP (Figs. 20 and 21) reveal multiple areas where negative OLR and VP signals linked to high R days or R changes overlap. The OLR signal generally shows more statistically significant areas than VP. Two areas in the Pacific stand out: The eastern North Pacific and the Philippine Sea in the western Pacific.

At lag 0 significant OLR and VP anomalies (up to -11 W m^{-2} and exceeding -1x10^6 m^2 s^{-1} respectively; Fig. 20a) and a significant signal in the regression analysis of both OLR (Fig. 21a) and VP (Fig. 21b) are found in the eastern North Pacific around 30°N and 145° W. Therefore, OLR anomalies over the

eastern North Pacific were averaged (OLR_{NE-Pac}; Tab. 3) to investigate possible links to R_{NE-Pac}. At lag 0 (Figs. 20a and 21a), large negative significant OLR anomalies exceeding -14 W m^{-2} are also found in the western Pacific, in the Philippine Sea (around 25° N and 140° E). The VP signal is not significant in the regression or composites. Nonetheless, OLR anomalies over the Philippine Sea are investigated ($OLR_{Philip-Sea}$; Tab. 3) for links to R_{NE-Pac}.

Furthermore, the composite at lag 0 (Fig. 20a) shows statistically significant OLR and VP anomalies over the Caribbean and Central America (at 18° N and 95° W) of up to -8 W m^{-2} and -0.75x10^6 m^2 s^{-1} respectively. The regression of R onto OLR at lag 0 (Fig. 21a) also shows a signal in the Caribbean. However, preliminary analysis in PCMCI revealed that whilst OLR in the Caribbean is linked to R_{NE-Pac}, the link is instantaneous across all timescales except for a weak link at lag 9 in the daily model from R_{NE-Pac} to OLR in the Caribbean (see Appendix A3.3). It is possible that OLR in the Caribbean is driven by R_{NE-Pac} via eddy-mean flow interactions, where the wave energy from breaking RRWPs can drive the meridional circulation in the tropics (Vallis, 2007, p. 305), as for the links from R_{N-Atl} to $OLR_{Gulf-Guinea}$ (see section 3.1.3). Nonetheless, as even the daily model found an instantaneous link and directionality could not be well assessed, OLR in the Caribbean is not further investigated. Moreover, the composite at lag 10 (Fig. 20c) reveals negative OLR and VP anomalies in the Bay of Bengal (at 8° N and 97° E) exceeding -14 W m^{-2} and -0.5x10^6 m^2 s^{-1}, respectively. Note that whilst the regression analysis at lag 0 (Fig. 21a) shows a similar OLR signal north of the Bay of Bengal, they are spatially distinct. It is plausible that the anomalous convection in this area could trigger RW trains which might cause RRWPs. However, preliminary analysis in PCMCI revealed no direct links from OLR in the Bay of Bengal to R_{NE-Pac} (see Appendix A3.4). Only in the daily model is OLR in the Bay of Bengal linked to R_{NE-Pac} via $blocks_{WR-GL}$ at lags 2,1, and 3 and the sign of the link is not consistent across lags. Therefore, OLR in the Bay of Bengal was not further investigated. The choice to not further investigate these OLR actors was made to include only the most plausible actors in the causal model. Furthermore, limiting the number of actors included in the network increases legibility of the graphical causal model.

Since the Greenland blocking precedes RRWPs, this blocking feature is further investigated, especially regarding tropical forcing. Therefore, one theory, which is only partially motivated by the composites, and more by literature, is investigated. Cassou (2008) studied links between the MJO phases and North Atlantic weather regimes. He found an increase in occurrence of up to 60 % of the NAO- regime 10-15 days after MJO phase 6 and 4-15 days after MJO phase 7. In the more refined classification by Grams et al. (2017) the Greenland blocking regime, GL, is the analogue of the NAO-. Therefore, the links Cassou (2008) finds between the MJO and NAO- might be found between an OLR based actor and $blocks_{WR-GL}$. Cassou (2008) showed that convection and upper-level divergence in the eastern tropical Pacific at around 15° N and 120° W during MJO phase 6 leads to northwards advection of anticyclonic vorticity anomalies. These can propagate to Europe with the jet leading to anticyclonic anomalies over Greenland and thus preferred occurrence of NAO-. The composite analysis does not strongly discourage this hypothesis. The composites at lags 3 and 10 days (Fig. 20b and 20c) show negative, but non-statistically significant, OLR and VP anomalies in the eastern Pacific (up to -8 W m^{-2} and -0.25x10^6 m^2 s^{-1} respectively). Therefore, OLR anomalies in the eastern Pacific (OLR_{E-Pac}) are investigated in PCMCI.

3.2.2 PCMCI

In summary, the following actors were created and analysed in a causal network for the eastern North Pacific at three different time scales (Figs. 22-24): R_{NE-Pac}, $blocks_{NA-wcoast}$, $blocks_{WR-GL}$, $U250_{NE-Pac}$, OLR_{NE-Pac}, OLR_{E-Pac}, and $OLR_{Philip-Sea}$ (Tab. 3). In the following section the results from PCMCI are presented separately for each possible driver (atmospheric blocking, changes in the background flow, and forcing from deep convection) before they are discussed in section 3.2.3. Notation is as in section 3.1.2.
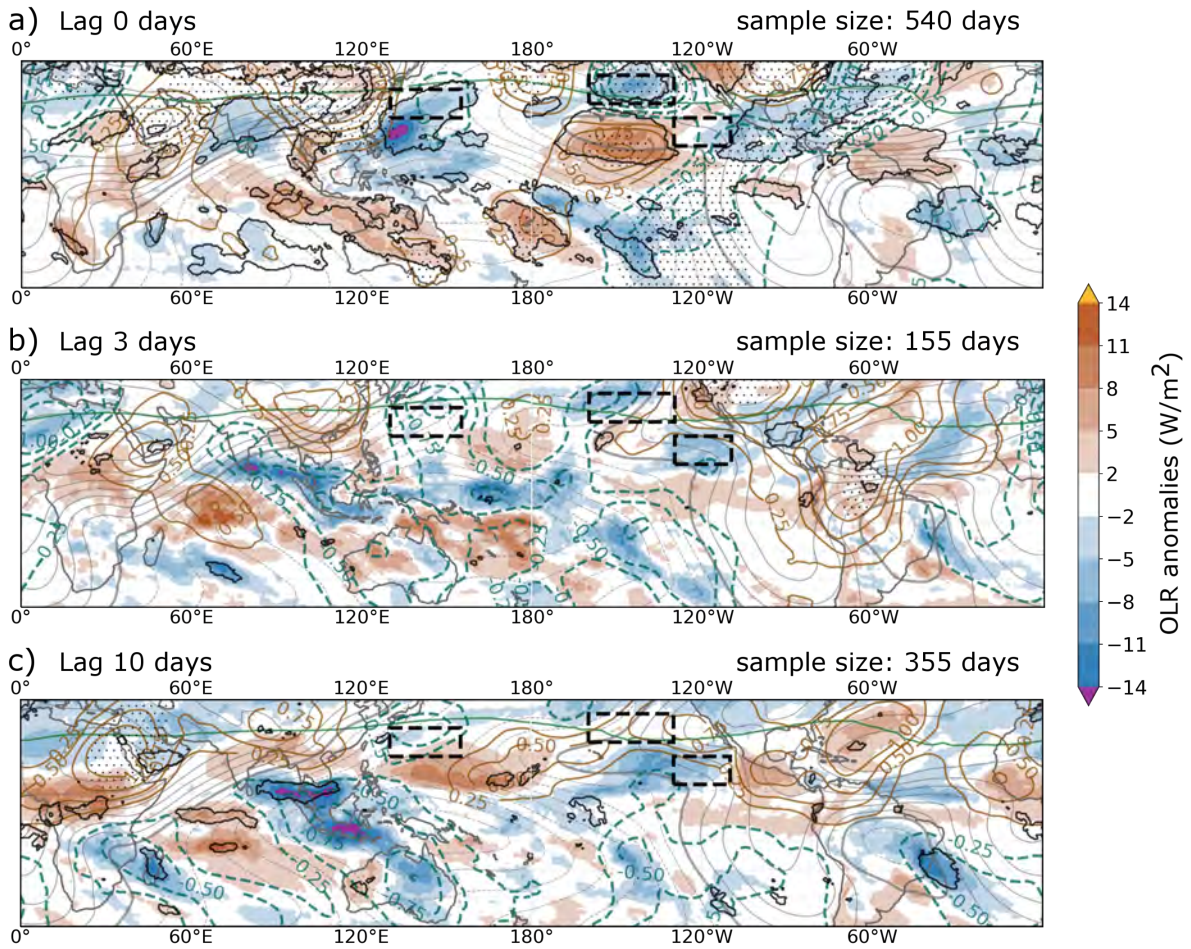
Figure 20: As Figure 11, but composites of OLR and VP anomalies leading up to high *R* days in the eastern North Pacific at lag a) 10 days, b) 3 days, and c) 0 days, i.e., during high *R* days. The spatial extent of $OLR_{Philip-Sea}$ (at 25° N and 125° E), OLR_{NE-Pac} (at 30° N and 145° W), and OLR_{E-Pac} (at 15° N and 120° W) is indicated by rectangles of black dashed lines.
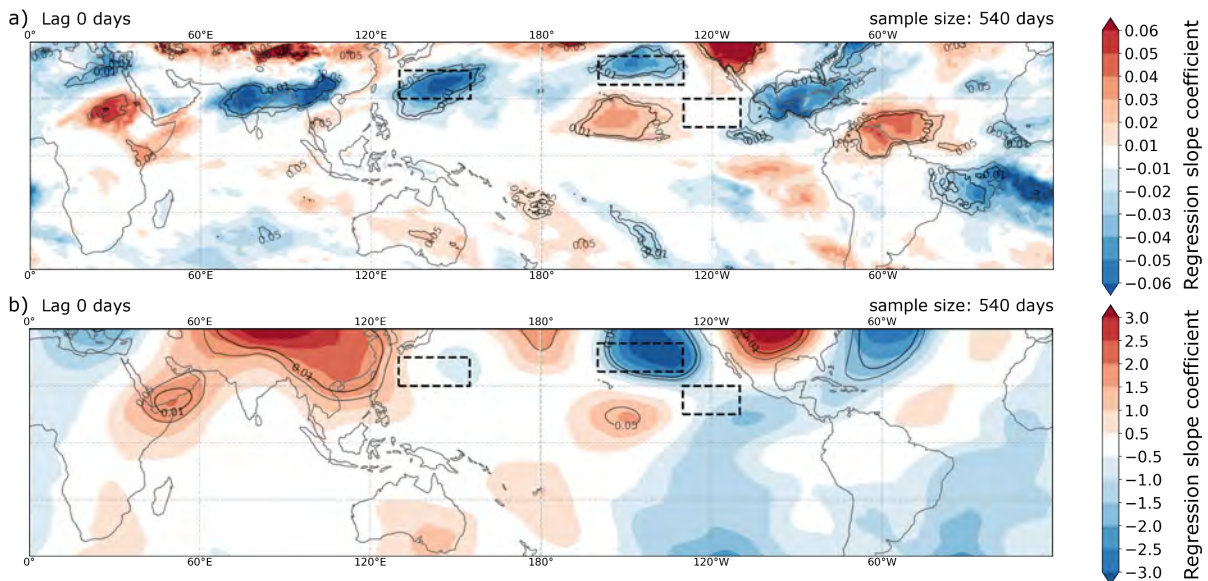

Figure 21: As Figure 12, but a) regression of R_{NE-Pac} on OLR at lag 0 and b) regression of R_{NE-Pac} on VP at lag 0. The spatial extent of $OLR_{Philip-Sea}$ (at 25° N and 125° E), OLR_{NE-Pac} (at 30° N and 145° W), and OLR_{E-Pac} (at 15° N and 120° W) is indicated by rectangles of black dashed lines.

32

Table 3: List of actors in the causal networks for *R* in the eastern North Pacific.

Abbreviation	Actor	Variable [unit]	Region	Standard deviation
R_{NE-Pac}	RRWPs in the eastern North Pacific	R [m s^{-1}]	35° N - 65° N, 175° W - 115° W	3.56
$blocks_{NA-wcoast}$	Blocking over the west coast of North America	Fraction of area blocked [%]	45° N - 65° N, 140° W - 110° W	0.13
$blocks_{WR-GL}$	Greenland blocking weather regime index	Correlation to Greenland blocking (Appendix A2.1)	NA	1.00
$U250_{NE-Pac}$	Background flow over the eastern North Pacific and western North America	Zonal wind U at 250 hPa, filtered for wavenumbers k 0-3 [m s^{-1}]	40° N - 53° N, 170° W - 130 ° W	7.10
OLR_{NE-Pac}	Convection over the eastern North Pacific		25° N - 35° N, 160° W - 130° W	12.97
$OLR_{Philip-Sea}$	Convection over the Philippine Sea	Outgoing longwave radiation [W m^{-2}]	20° N - 30° N, 130° E - 155° E	17.04
OLR_{E-Pac}	Convection over the tropical eastern Pacific		10° N - 20° N, 130° W - 110° W	19.53

3.2.2.1 *Atmospheric blocking*

Overall, an increase in $blocks_{WR-GL}$ is found to increase R_{NE-Pac} at weekly time lag. This is evident from the positive link $blocks_{WR-GL} \rightarrow R_{NE-Pac}$ at lag 7 (0.068) in the daily model (Fig. 22) and lag 1 (0.151) in the 6-daily model (Fig. 24). This matches the positive relationship between *R* and blocking around Greenland at time lags up to 10 days found in the composites and regression (Figs. 16 and 17). R_{NE-Pac} increases $blocks_{NA-wcoast}$ at time lag of about one week but decreases it at higher lags. The increase is seen in the daily model at lags 7,6 (0.085, 0.070) and the 6-daily model at lag 1 (0.196), whilst the decrease is captured by the 3-daily model (Fig. 23) at lag 3 (-0.099).

3.2.2.2 *Changes in the background flow*

$U250_{NE-Pac}$ and R_{NE-Pac} are linked with negative feedback on a 1 to 2 weekly scale, where an increase in $U250_{NE-Pac}$ increases R_{NE-Pac}, which successively causes a decrease in $U250_{NE-Pac}$. On the daily time scale a positive link $U250_{NE-Pac} \underset{\tau=7}{\longrightarrow} R_{NE-Pac}$ (0.065) and negative links in the opposite direction, $R_{NE-Pac} \underset{\tau=4,6}{\longrightarrow} U250_{NE-Pac}$ (-0.071 and -0.059), are detected. This pattern is also found in the 3-daily model with a positive link $U250_{NE-Pac} \underset{\tau=3}{\longrightarrow} R_{NE-Pac}$ (0.097) and a negative link R_{NE-Pac} $\underset{\tau=1}{\longrightarrow} U250_{NE-Pac}$ (-0.129). In the 6-daily model a negative link $R_{NE-Pac} \underset{\tau=1}{\longrightarrow} U250_{NE-Pac}$ (-0.211) and an instantaneous link (-0.162) are detected. As in the North Atlantic, a stronger zonal background flow can increase *R*, which then causes the background flow to decrease. However, the link $R_{NE-Pac} \rightarrow U250_{NE-Pac}$ at lag 2 (0.165) in the 6-daily model is positive, showing that at lags exceeding 1.5 weeks, high R_{NE-Pac} is again linked with higher $U250_{NE-Pac}$, i.e., increased zonal flow. Further, a negative instantaneous link $U250_{NE-Pac} \leftrightarrow blocks_{NA-wcoast}$ is present at all timescales (-0.189, -0.290, -0.308; for daily, 3-daily, and 6-daily model), with a negative lagged link U250

$\underset{\tau=1}{\longrightarrow} blocks_{NA-wcoast}$ (-0.094) in the daily model. Finally, there is also an instantaneous positive link $U250_{NE-Pac} \leftrightarrow blocks_{WR-GL}$ (0.094) in the 3-daily model, implying that Greenland blocking is associated with slightly increased background flow upstream.

3.2.2.3   *Forcing from deep convection*

OLR_{NE-Pac} drives actors on different time scales. It drives R_{NE-Pac} directly in the 6-daily model (Fig. 24) with a strong negative link $OLR_{NE-Pac} \underset{\tau=3}{\longrightarrow} R_{NE-Pac}$ (-0.136) and an instantaneous link (-0.147). Furthermore, OLR_{NE-Pac} drives R_{NE-Pac} indirectly through $U250_{NE-Pac}$ or $blocks_{WR-GL}$. In the daily model (Fig. 22) it drives $U250_{NE-Pac}$ at lag 2 (0.098) and a positive instantaneous link is present at 3-daily (0.137) and 6-daily timescales (0.240). On the daily timescale (Fig. 22) a negative link from OLR_{NE-Pac} to $blocks_{WR-GL}$ at lag 2 (-0.074) is present with positive links at lag 1 (0.071) and 3 (0.064). Remember that the blue arrow refers only to the strongest detected lag, which is negative. Overall, increased convection in the eastern North Pacific can increase R_{NE-Pac} at the sub weekly scale by modulating the background flow (Figs. 22-24), but can also directly increase R_{NE-Pac} at longer timescales exceeding 2 weeks (Fig. 24).

$OLR_{Philip-Sea}$ is not found as a direct or indirect driver of R_{NE-Pac}, but is driven by R_{NE-Pac} and $blocks_{WR-GL}$. R_{NE-Pac} decreases $OLR_{Philip-Sea}$ at lags 1 (-0.135) in the 3-daily model (Fig. 23) and is instantaneously connected to $OLR_{Philip-Sea}$ in the 6-daily model (-0.173). There is a negative link from $OLR_{Philip-Sea}$ to $blocks_{NA-wcoast}$ at lag of 3 days (-0.062) in the daily model and lag 1 (-0.119) in the 3-daily model. These pathways suggest that R_{NE-Pac} and $OLR_{Philip-Sea}$ contribute to an increase in $blocks_{NA-wcoast}$ directly, but R_{NE-Pac} can also modulate the blocking via $OLR_{Philip-Sea}$. Finally, the role of $blocks_{WR-GL}$ as a driver of North Pacific processes is again highlighted. It has a negative link to $OLR_{Philip-Sea}$ at lag 3 (-0.124) in the 3-daily model and lag 1 (-0.181) in the 6-daily model. In summary, R_{NE-Pac} drives a decrease in $OLR_{Philip-Sea}$ at the weekly scale, whilst $blocks_{WR-GL}$ drives a decrease in $OLR_{Philip-Sea}$ at around 2 weeks lag. Furthermore, $OLR_{Philip-Sea}$ is identified as a driver of $blocks_{NA-wcoast}$.

OLR_{E-Pac} has a negative link to R_{NE-Pac} on the daily scale at lag 6 (-0.087). Otherwise, OLR_{E-Pac} is not linked to an increase in R_{NE-Pac} directly or indirectly with mostly negative instantaneous links to dynamical actors in the eastern North Pacific, such as a negative instantaneous link to $blocks_{NA-wcoast}$ (-0.117) in the 6-daily model (Fig. 24). In the 3-daily and 6-daily model OLR_{E-Pac} is driven by $U250_{NE-Pac}$ at lags 2 (-0.112) and 1 (-0.194) respectively.
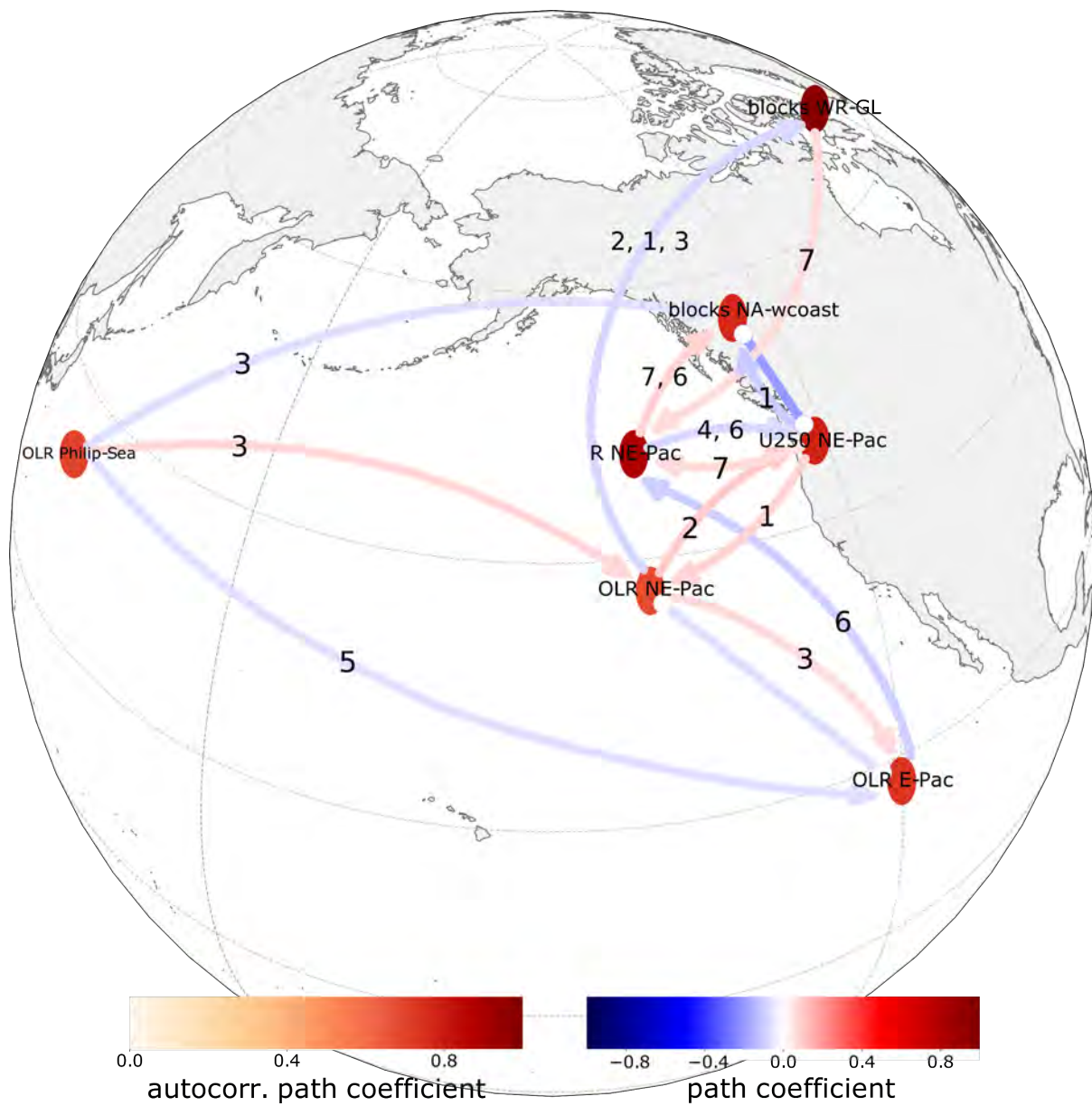
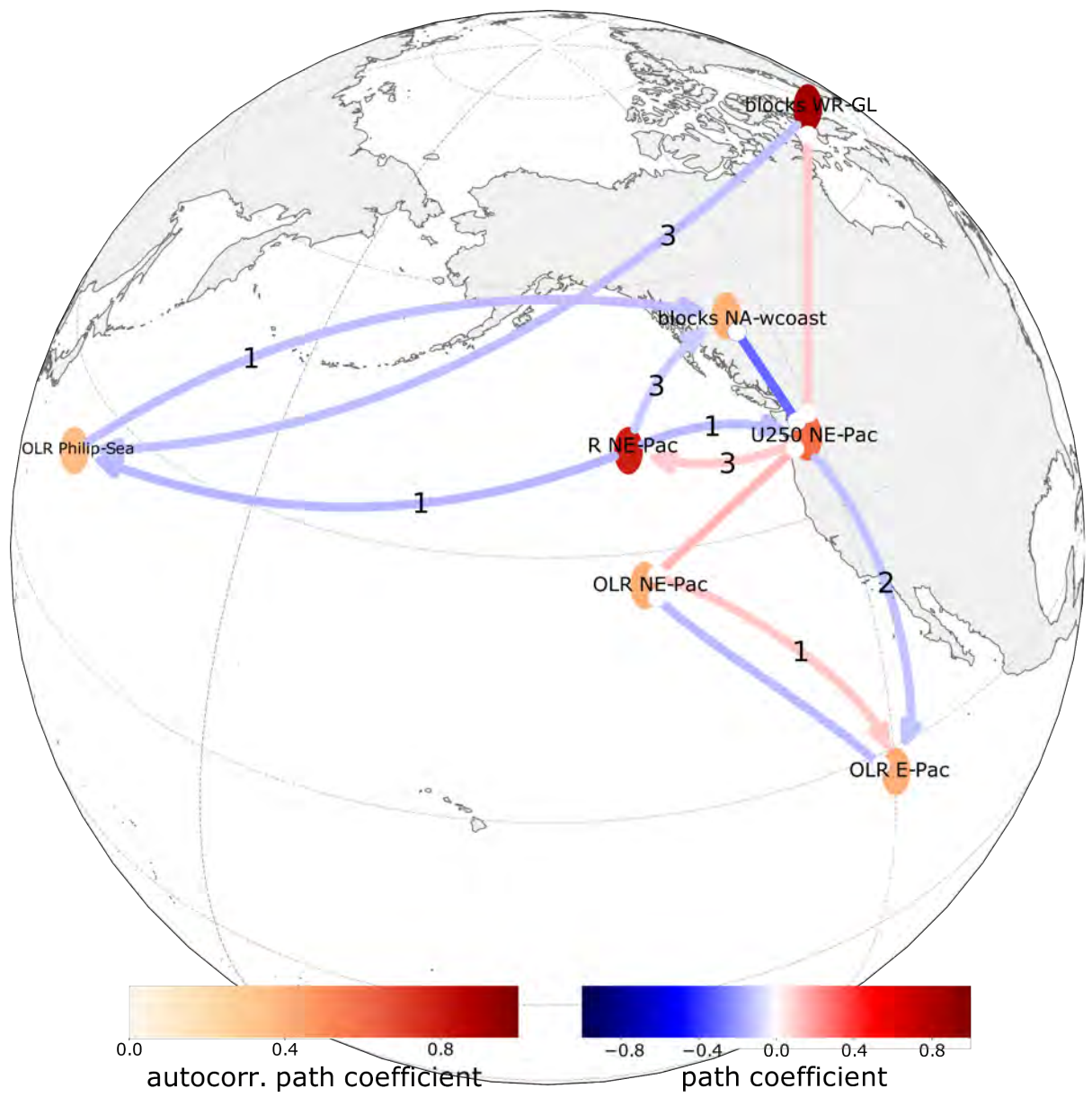**Figure 22: As Figure 13, but for the eastern North Pacific at daily time scale.**

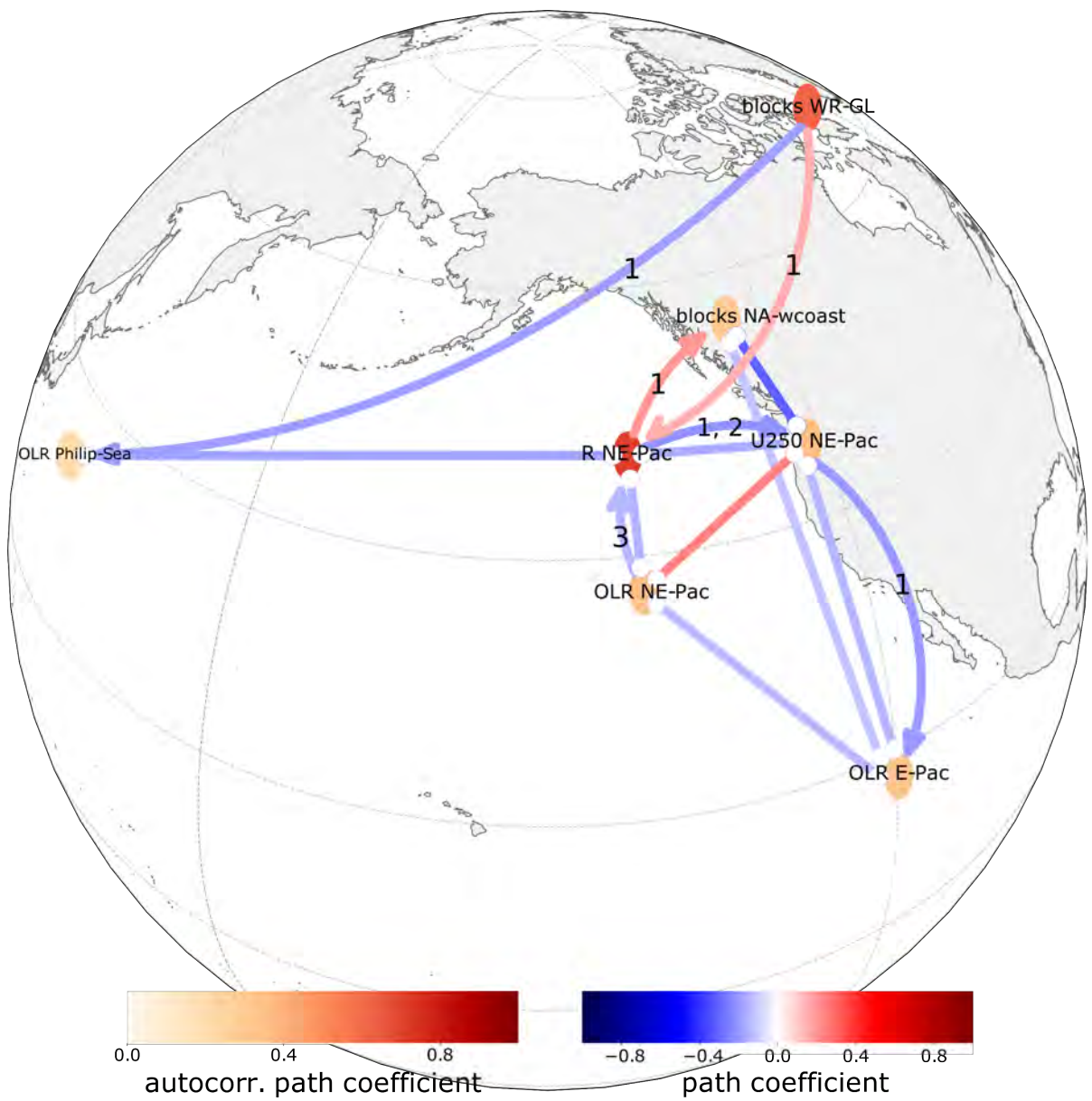**Figure 23: As Figure 22, but at 3-daily time scale.**

Figure 24: As Figure 22, but at 6-daily time scale.

3.2.3 Discussion

In the following section the results regarding drivers of R_{NE-Pac} are discussed. An increase of R_{NE-Pac} is driven at weekly time lag by an increase in the zonal background flow (Figs. 22 and 23). This was also found in the North Atlantic, but whilst there it was speculated to be due to the preferred regime transition (NAO+ and zonal flow transitioning preferably into blocked regimes), here the mechanism is unclear. As in the North Atlantic, the background flow and blocking are very closely linked, as the negative instantaneous link $U250_{NE-Pac} \leftrightarrow blocks_{NA-wcoast}$ at all timescales shows (Figs. 22-24). This implies that a reduction in the background flow relates to an increase of the fraction of area blocked, an effect described by Nakamura and Huang (2017).

Moreover, Greenland blocking, $blocks_{WR-GL}$, is identified as a direct positive driver of R_{NE-Pac} (Figs. 22 and 24) and it is mostly independent of processes in the North Pacific. Röthlisberger et al. (2019) show, that positive R anomalies occur up to 6 days after and up to 60° upstream of blocking in the North Pacific. However, their results are calculated across all seasons and thus not perfectly comparable to DJF as used in this work. Moreover, the statistically significant Greenland blocking signal extends no further than 65° W and R_{NE-Pac} is defined as westwards of 115° W, so that at least 50° longitude lie between the signals. The physical mechanism for how blocking might cause RRWP activity far upstream is unclear, as upstream disturbances from perturbations to the background flow are generally of small magnitude (Simmons and Hoskins, 1979). However, one possibility is that the diffluent flow upstream of $blocks_{WR-GL}$ increases the amplitude of the upstream RWs (Shutts, 1983; Nakamura and Huang, 2017). This pathway is hinted at in the 3-daily model (Fig. 23), where the link from $blocks_{WR-GL}$ to R_{NE-Pac} goes through $U250_{NE-Pac}$. Another possibility might be, that the Greenland blocking triggers RW trains on the Arctic waveguide. Martius et al. (2010) present a case study, where a breaking wave on the extratropical waveguide, associated with a strong ridge qualitatively not unlike Greenland blocking, initiated a wave train on the Arctic waveguide. Wave trains on the Arctic waveguide can propagate across Asia and foster RW initiation in the North Pacific (Röthlisberger et al., 2018) and could thus cause RRWPs. A further explanation is a missing driver, which modulates the effect of $blocks_{WR-GL}$ on R_{NE-Pac} or affects both variables.

Assuming no missing driver for the link $blocks_{WR-GL} \rightarrow R_{NE-Pac}$, what causes an increase of Greenland blocking is of interest, as this might improve prediction of RRWPs in the eastern North Pacific. In this work, the excitation of an NAO- phase (which is similar to Greenland blocking) by forcing from convection in the eastern tropical Pacific (Cassou, 2008) was investigated. However, the selected actor, OLR_{E-Pac}, shows no links to $blocks_{WR-GL}$, nor a robust link to R_{NE-Pac} (Figs. 22-24). PCMCI not showing a link, does not exclude the mechanism proposed by Cassou (2008). The mechanism can still be present in single cases, $blocks_{WR-GL}$ is not identical to NAO-, and the OLR signal might not adequately represent the full tropical forcing, which will be discussed in section 3.3.2 on limitations. Alternatively, the Greenland blocking develops locally (Feldstein, 2003; Cassou, 2008) or could be forced by diabatic processes in the Caribbean, which are known to influence the North Atlantic circulation (Hoskins and Sardeshmukh, 1987; Manola et al., 2013; Knight et al., 2017; Li et al., 2020). However, no consistent directed links from an actor representing OLR in the western Caribbean and Central America to either R_{NE-Pac} or $blocks_{WR-GL}$ could be identified (see Appendix A3.3).

Overall, the pattern linking R_{NE-Pac} and blocking is less consistent across models than in the North Atlantic, due to the different links detected between R_{NE-Pac} and blocks in the 3-daily model (Fig. 23) compared to the daily and 6-daily models. Concretely, the 3-daily model shows no link between $blocks_{WR-GL}$ and R_{NE-Pac} and a negative link $R_{NE-Pac} \xrightarrow{\tau=3} blocks_{NA-wcoast}$. Whilst a strong positive link $R_{NE-Pac} \rightarrow blocks_{NA-wcoast}$ is present at weekly lag, detected by the daily and 6-daily model (Figs. 22 and 24), a negative link is present at about two weekly lag, detected by the 3-daily model at lag 3 (Fig. 23). This highlights the advantage of investigating processes using multiple time scales, as done by Kretschmer et al. (2016). Doing so can help uncover links not detected at other scales and therefore provides a fuller view of the causal network.

Additionally, convection in the eastern North Pacific (OLR_{NE-Pac}) and to a lesser degree in the eastern Pacific (OLR_{E-Pac}) influence R_{NE-Pac} directly or via $U250_{NE-Pac}$. However, most links are not consistent across time scales and some links show that increased convection can decrease R_{NE-Pac}. OLR_{NE-Pac} is linked to R_{NE-Pac} via $U250_{NE-Pac}$ with positive links (Figs. 22-24), indicating that an increase in convection (decrease in OLR) reduces $U250_{NE-Pac}$ which reduces R_{NE-Pac}. However, the composites and regression analysis of OLR and VP (Figs. 20 and 21) show the opposite relationship, i.e., that increased convection is linked to an increase in R_{NE-Pac}. This is only found in the 6-daily model (Fig. 24), with an instantaneous and lag 3 negative link $OLR_{NE-Pac} \rightarrow R_{NE-Pac}$. Whilst OLR_{E-Pac} drives R_{NE-Pac} at lag 6 in the daily model (Fig. 22), it is otherwise mostly related to $U250_{NE-Pac}$ and OLR_{NE-Pac}.

Generally, R_{NE-Pac} is identified as an important driver of North Pacific processes. The short-term increase in $blocks_{NA-wcoast}$ is driven by R_{NE-Pac} both directly and via a decrease in $U250_{NE-Pac}$ (Figs. 22-24). This matches well with previous observations that positive R anomalies occur before and upstream of blocking in the North Pacific (Röthlisberger et al., 2019) and that blocking is often preceded by a wave train upstream, which can act to strengthen the blocking (Altenhoff et al., 2008). The negative effect of R_{NE-Pac} on $blocks_{NA-wcoast}$ at higher lags (lag 3 in the 3-daily model; Fig. 23) could be explained by the rapid decay of the blocking signal after high R days seen in the composites (see Appendix A3.5). If RRWPs only occur for a few days, the associated increase in R and blocking over the west coast of the US, is likely to be followed by a decrease in blocked area and zonal flow. As the mean length of consecutive high R days in DJF for the eastern North Pacific is 9.45 days (median 7 days) such cases can exist. Whether this is indeed the mechanism behind the negative effect of R_{NE-Pac} on $blocks_{NA-wcoast}$ at higher lags is unclear, however.

Finally, $OLR_{Philip-Sea}$ is driven by R_{NE-Pac} (Fig. 23) and $blocks_{WR-GL}$ (Figs. 23 and 24) at 1-2 weeks lag, although these links are inconsistent across time scales. The latter is difficult to explain. It might be linked to RWs on the Arctic waveguide initiated by blocking over Greenland, which can initiate RWs in the western Pacific (Röthlisberger et al., 2018) and lead to convection. Alternatively, another mediating or common driver could explain the link. The former might be a signal connected to co-occurrence of RRWPs in the western North Pacific and RRWPs in the eastern North Pacific. R values in the western North Pacific are increased during high R days in the eastern North Pacific by 2-5 m s^{-1} (Appendix A3.6). Furthermore, the composite of OLR and VP during high R days in the western North Pacific also shows large magnitude OLR and VP anomalies over the Philippine Sea (Appendix A3.7). Thus, it can be imagined that R in the western North Pacific is a missing driver explaining the link $R_{NE-Pac} \rightarrow OLR_{Philip-Sea}$.

3.3 General discussion, limitations, and outlook

In this section, the main findings across basins, but also important differences between them, as well as results regarding the application of PCMCI to analyse the drivers of RRWPs are discussed (3.3.1). Then, limitations of this study as well as an outlook are given.

3.3.1 General discussion

In both studied basins, blocks could be identified as a driver of R, although the mechanisms differ. Blocking in the central North Atlantic ($blocks_{N-Atl}$), so co-located or slightly upstream of the area defined for R_{N-Atl}, increases R_{N-Atl} (Figs. 13 and 14). This is further evidence that blocks can initiate RRWPs downstream (Röthlisberger et al., 2019; Ali et al., 2021). In the eastern North Pacific, Greenland blocking ($blocks_{WR-GL}$), downstream of the area defined for R_{NE-Pac}, was found to drive R_{NE-Pac} (Figs. 22 and 24). The physical mechanism here is unclear, as signals propagating upstream from an initial perturbation are generally weak (Simmons and Hoskins, 1979). However, the 3-daily model (Fig. 23) shows a positive link between $blocks_{WR-GL}$ and R_{NE-Pac} going through $U250_{NE-Pac}$. It is possible that the blocks influence the upstream background flow, which can affect the amplitude of the upstream RWs (Shutts, 1983; Nakamura and Huang, 2017), and thereby foster RRWPs. Moreover, the influence of $blocks_{WR-GL}$ on R_{NE-Pac} could be due to either the Greenland blocking exciting waves on the Arctic waveguide (Martius et al., 2010), which can propagate over Asia into the

North Pacific (Röthlisberger et al., 2018), or perhaps from an unobserved driver, which mediates the link or acts as a common driver.

The zonal background flow is a driver of R in both basins (Figs. 13, 15, 22, and 23). A distinct pattern of a reversal from an increased zonal flow before RRWPs to decreased background flow magnitude during RRWPs is discovered. A positive anomaly in the background flow drives an increase in R one week later and R then causes a decrease in the background flow. Long-lived RWPs are known to affect the background flow, mostly close to the location of the RWP (Wirth et al., 2018), and RRWPs could have a similar effect.

In both basins, R was found to drive an increase in downstream blocking: Over the west coast of North America for R_{NE-Pac} (Fig. 22 and 24) and over Scandinavia for R_{N-Atl} (Figs. 13-15). This mechanism was also suggested by Röthlisberger et al. (2019) and in general the contribution of transient waves to stationary or blocked flow is well established (Shutts, 1983; Nakamura and Huang, 2017; Ma and Franzke, 2021). Note that in the North Atlantic this link goes via the effect of R_{N-Atl} on the background flow over north-western Europe or blocking in the central North Atlantic, which then modulate Scandinavian blocking.

Overall, this leads to a distinctive causal pathway with an increase of R decreasing the local background flow which fosters blocks. This could be related to the findings of Nakamura and Huang (2017), who found that transient wave trains in a diffluent, decelerating flow can lead to wavey flow and blocking like patterns, explaining the link between R and blocks as well as the modulating effect of the decreased background flow. This is further complemented by Huang and Nakamura (2017) who find that advection of large LWA, as is the case in RRWPs, and the deceleration and diffluence of the background flow can reinforce each other. This might explain the feedback between R and the background flow.

RW forcing from deep convection was not found as a major driver of RRWPs. Despite some links from OLR actors to R, no links could be detected consistently across time scales. Whilst convection in the eastern Pacific and eastern North Pacific showed some direct links to R_{NE-Pac} (Figs. 22 and 24), convection in the Philippine Sea did not drive R_{NE-Pac}, nor was OLR over the Maritime Continent connected to R_{N-Atl}. However, the forcing from (tropical) deep convection on the extratropical atmosphere in general, and RW dynamics specifically, is well established (Jin and Hoskins, 1995; Wheeler and Hendon, 2004; Cassou, 2008; Moore et al., 2010; Röthlisberger et al., 2018) and the connection to RRWPs has been established in case studies (Davies, 2015; Barton et al., 2016). It is possible that no links were found because the OLR drivers in this study did not fully represent the effect of forcing from deep convection. Nonetheless, these results provide some evidence that dynamical processes within the extratropics, rather than tropical forcing through deep convection, drive RRWPs.

In both basins, R is a driver of deep convection in the tropics. This is clearest in the North Atlantic where R_{N-Atl} drives convection over the Gulf of Guinea (Figs. 14 and 15). In the eastern North Pacific, the links are less consistent and change or disappear depending on the investigated time scale. Nevertheless, R_{NE-Pac} directly increases convection over the Philippine Sea (Figs. 23 and 24) and indirectly influences convection in the eastern Pacific and eastern North Pacific.

With few recent exceptions (Saggioro and Shepherd, 2019; Hirt et al., 2020; Samarasinghe et al., 2020), most studies in climate sciences using causal inference methods investigated lower frequency interactions, e.g., monthly teleconnections (Kretschmer et al., 2016; Di Capua et al., 2020a), where interactions are more linear, and autocorrelation is lower. This study provides further evidence that linear causal inference algorithms can capture synoptic-scale links. Finally, deriving causal networks for multiple time scales can be treated as a sensitivity test for the robustness of links. Here, links were mostly consistent across time scales, showing that the investigated causal links are robust. Where this was not the case, different time scales can reveal links which would otherwise have been missed, as the negative link $R_{NE-Pac} \xrightarrow[\tau=3]{} blocks_{NA-wcoast}$ in the 3-daily model.

3.3.2 Limitations and outlook

Although the detection power of PCMCI increased when using coarser resolution time-averaged data, many instantaneous links with no direction of causality were detected (Figs. 15 and 24), as PCMCI uses information on time order to derive the direction of causality (Runge et al., 2019b). The newest working version of PCMCI, PCMCI+ (Runge, 2020), could be used here. It can detect the direction of instantaneous relationships and has improved handling of autocorrelation. Additionally, PCMCI rests on the assumption of causal sufficiency, which means that all common drivers are included in the network (Runge et al., 2019b). This assumption is always violated to a varying degree in complex systems like the climate system. In this work, certain links, e.g., $blocks_{WR-GL} \rightarrow R_{NE-Pac}$, were also speculated to be due to a common or mediating driver, but no quantitative statements on the presence or magnitude of this missing driver can be made. A novel adaptation to PCMCI, Latent-PCMCI (LPCMCI; Gerhardus and Runge, 2020), can quantify this contribution from unknown drivers (and detect instantaneous relationships as PCMCI+ does). Quantifying the contribution of unknown drivers can help to understand links for which no well-established physical mechanism exists and validate how well the constructed causal networks explain the observed variability in the investigated variables. However, at the time of writing LPCMCI is not yet publicly available.

The topic of missing drivers was especially relevant to this work, as the drivers of RRWPs have not been firmly established in previous studies. Recent studies have shown that the assumption of Causal Sufficiency, i.e., that no unobserved drivers exist, can be relaxed (Runge et al., 2019a). Applying PCMCI nevertheless necessitates strong knowledge of the system to select appropriate time series, or actors, so that robust and established hypotheses can be tested (Kretschmer et al., 2016; Runge et al., 2019b), which was not fully given in this case. Therefore, the results of this more exploratory analysis should be treated with a certain caution. Whilst some potential drivers of RRWPs could be identified and their contributions quantified, the completeness of the causal network is not given, as RRWPs are not yet well understood. Specifically, the process of defining latitude-longitude boxes over which to average variables to create actors, whilst based on the results of the composites and regression analysis, is somewhat subjective. Therefore, future investigations on the drivers of RRWPs might very well lead to a slightly different set of actors and links. An interesting alternative to selecting areas of interest manually is response guided causal precursor detection (RG-CPD). It can identify relevant (i.e., correlating) and spatially coherent areas in gridded data as causal parents of a process, whilst considering autocorrelation, common drivers, or mediated links (Di Capua et al., 2020a). Thus, it allows for a more accurate definition of precursor areas than manually defining a latitude-longitude box as done in this work. PCMCI can then be applied to time series generated from spatial averages over these regions.

A further issue faced in this work is the high autocorrelation of the time series, leading to generally low detection power of PCMCI (Runge, 2020), as much of the variance in the time series can be explained by autocorrelation rather than cross correlation. Note that the autocorrelation path coefficient is generally higher than the path coefficient (Figs. 13-15 and 22-14). Link strength increased with decreasing temporal resolution, i.e., it is lowest in the daily model. Variability in links is also largest in the daily model, where links of the opposite sign were detected at subsequent time lags. Time-averaging to 3-daily or 6-daily scales removes this effect and produces more robust causal networks with the downside of more instantaneous links. This shows the synoptic nature of RRWPs and the other studied actors and highlights two connected issues: (1) Capturing links well within the synoptic time scale (e.g., daily or 3-daily in this work) could be of interest to better understand what causes RRWPs. This is difficult due to the large autocorrelation inherent to variables in the climate system, and especially for R, which is a time-averaged variable. Here, time series modelling approaches might be used to reduce autocorrelation. Alternatively, time-averaging leads to higher detection power, but with the downside of increased instantaneous links. (2) Thus, whilst investigations into precursors of RRWPs on larger timescales (sub-seasonal or seasonal) are also of interest from a forecasting perspective, simply time-averaging the actors, e.g., using 30-day means, will not produce good results. In a causal network for R_{N-Atl} at the monthly scale (Appendix. A3.8) all links are instantaneous, except for links between OLR actors, which can act on these lower frequency time scales (Wheeler and Hendon, 2004; Moore et al.,

2010). Thus, for the seasonal to sub-seasonal scale, different techniques to transform the dynamical actors (R, blocks, background flow) into time series at lower temporal resolution must be investigated.

Moreover, the composite and regression analysis only capture changes over a mean state. Neither can consider separate pathways leading to RRWPs, e.g., for an individual event, high values in R_{N-Atl} might be entirely related to Atlantic blocking, with no influence from Scandinavian blocking. Case studies can complement climatological analyses (Moore et al., 2010) and further case studies on RRWPs could illuminate the causal pathways discovered in this work. Alternatively to case studies, separating contributions to the observed variance in RRWPs explained by different variables using principal component analysis or maximum covariance analysis would be interesting. This has been used in conjunction with causal inference methods before (Di Capua et al., 2020a and 2020b). Finally, some very concrete limitations are the focus on DJF and the two basins in the northern hemisphere only. Other potential drivers of RRWPs could be studied (Röthlisberger et al., 2019). Despite no robust results on RW forcing from deep convection, this should be further investigated, as the actors derived from OLR anomalies do most likely not capture the full RW forcing exercised by deep convection and RRWPs have been shown to be forced by deep convection (Barton et al., 2016).

4. Conclusion

In this work, potential causal drivers of boreal winter recurrent Rossby wave packets (RRWPs) in the North Atlantic and eastern North Pacific basins are investigated using the causal inference method PCMCI. RRWPs were measured using the R-metric (R) and the investigated drivers are atmospheric blocking, changes in the zonal background flow, and forcing from deep convection measured by anomalous outgoing longwave radiation (OLR). Concretely, the goals of this thesis were (1) to identify regions where these potential drivers might modulate R and (2) to quantify these links in terms of time lag and strength using causal networks created with PCMCI.

Anomalous patterns in the investigated drivers during RRWP events, defined as days with high R values, were investigated using composite maps. Hereby, mean anomalies of the drivers during and leading up to days with high R were studied. Furthermore, regressions of R on the various drivers were carried out to quantify and map the mean change of R over a basin associated with changes in the drivers at each gridpoint and at different time lags. From the composite and regression maps, areas and time lags where changes in potential drivers are linked to high R days or changes in R could be derived. The causal inference method PCMCI uses two phases of iterative partial correlation tests to establish and quantify statistically significant links between time series as well as their time lags. In other words, it derives (lagged) correlations between variables which cannot be explained by any other confounding variable included in the analysis and are therefore assumed causal in nature. The variables in areas identified as relevant from the composites and regression analysis were spatially averaged to time series and PCMCI applied to them. To investigate the different time scales at which processes act, PCMCI was applied to daily, 3-daily, and 6-daily data resulting in three different causal networks.

R in the North Atlantic (R_{N-Atl}) is increased within one week after co-located or slightly upstream blocking in the central North Atlantic, which is partially driven by a decrease in the central North Atlantic background flow. Furthermore, a more zonally oriented state over north-western Europe and Scandinavia, with a stronger zonal background flow over north-western Europe and a decrease in Scandinavian blocking, can increase R_{N-Atl} one week later. An increase in R_{N-Atl} in turn has a negative effect on the strength of the background flow. Moreover, R_{N-Atl} directly drives an increase in blocking and a decrease in the background flow in the central North Atlantic and drives a decrease in the background flow over north-western Europe, thus also increasing blocking over Scandinavia. Anomalous deep convection could not be identified as a direct driver of R_{N-Atl}. However, an increase in R_{N-Atl} causes increased tropical convection, indicated by lower OLR values, over the Gulf of Guinea at a lag of one week. This is hypothesized to be explainable by eddy-mean flow interactions, where the wave energy from breaking RRWPs drives an increased meridional circulation in the tropics.

R in the eastern North Pacific (R_{NE-Pac}) is increased with a lag of one week by an increase in blocking over Greenland. The physical mechanism behind this link is unclear. It is speculated that the Greenland blocking could initiate disturbances on the Arctic waveguide, which can propagate into the Pacific, or that the Greenland blocking influences R_{NE-Pac} via the diffluent background flow upstream of the block, or that an unobserved driver mediates the link or drives both variables. An increase in the local background flow causes an increase in R_{NE-Pac} which, as in the North Atlantic, has a negative effect on the strength of the background flow. Furthermore, an increase in R_{NE-Pac} causes increased blocking over the west coast of North America at lag of 1 week. At higher lag this positive link is reversed and R_{NE-Pac} has a negative effect on blocking over the west coast of North America. A decrease in OLR, signifying increased convection, in areas of the eastern and north-eastern Pacific can increase R_{NE-Pac}, but these links are inconsistent across the different temporal resolutions studied. Finally, despite OLR signals in the composites and regression analysis, anomalous deep convection in the Philippine Sea could not be identified as a direct driver of R_{NE-Pac}.

Applying PCMCI to high resolution synoptic-scale data showed that most links are robust across the different (synoptic) timescales investigated here (daily, 3-daily, and 6-daily). However, a few links did change and show different causal connections, highlighting the advantage of investigating one causal network across multiple time scales. At the 6-daily time scale, many links became instantaneous, confirming that RRWPs and the investigated drivers act largely within the weekly time scale.

In conclusion, in both studied basins, an increase in R is driven by a prominent blocking feature. Meanwhile, increasing R increases blocking downstream, although this effect is not necessarily direct, but through the negative influence of R on the local background flow. Furthermore, a conspicuous pattern of a more zonal flow before an increase in R emerges, which subsequently decreases due to the increase in R. Deep convection could not robustly be identified as a driver of R, although links are present in some time lags. However, R was found to drive tropical OLR changes. Overall, this work could identify and confirm atmospheric blocking and changes in the local background flow as drivers of RRWPs which should be investigated in future research to improve the prediction of RRWPs.

Appendix

A1 Supplementary material – Introduction

A1.1 – Basic Rossby wave theory

RWs exist due to the meridional gradient of potential vorticity (PV) and can be viewed as perturbations of PV propagating eastwards (Hoskins et al., 1985) along an area of enhanced PV gradient, often described as the (Rossby) waveguide (Martius et al., 2010). RWs adhere the following dispersion relation

$$w = u_0 k - \frac{k\,\beta}{k^2 + l^2}$$

(Eq. 16)

, where w is the angular frequency, u_0 the constant zonal mean background flow, k and l the zonal and meridional wavenumbers, and β is the northward gradient of planetary vorticity (Rossby, 1945). The amplitude of Rossby waves can vary across longitude and time. Local maxima of Rossby wave amplitudes are termed a Rossby wave packet (Fig. 1; Wirth et al., 2018). From the dispersion relation *(Eq. 16)* two terms can be derived: The zonal phase speed, $c = w/k$, describing the propagation of the individual troughs and ridges forming the waves, and the zonal group velocity, $c_g = \partial w / \partial k$, describing the propagation of the envelope of the waves, i.e., the RWP. As β is positive, it follows that $c_g > c$, and hence the envelope of Rossby waves, or RWP, moves eastwards faster than the Rossby waves. Troughs and ridges at the upstream end of the envelope dissipate, whilst new troughs and ridges form at the downstream end, giving rise to the notion of "downstream development" (Fig. 1; Wirth et al., 2018).

A1.2 – 2002 extreme precipitation over Switzerland described in Barton et al. (2016)
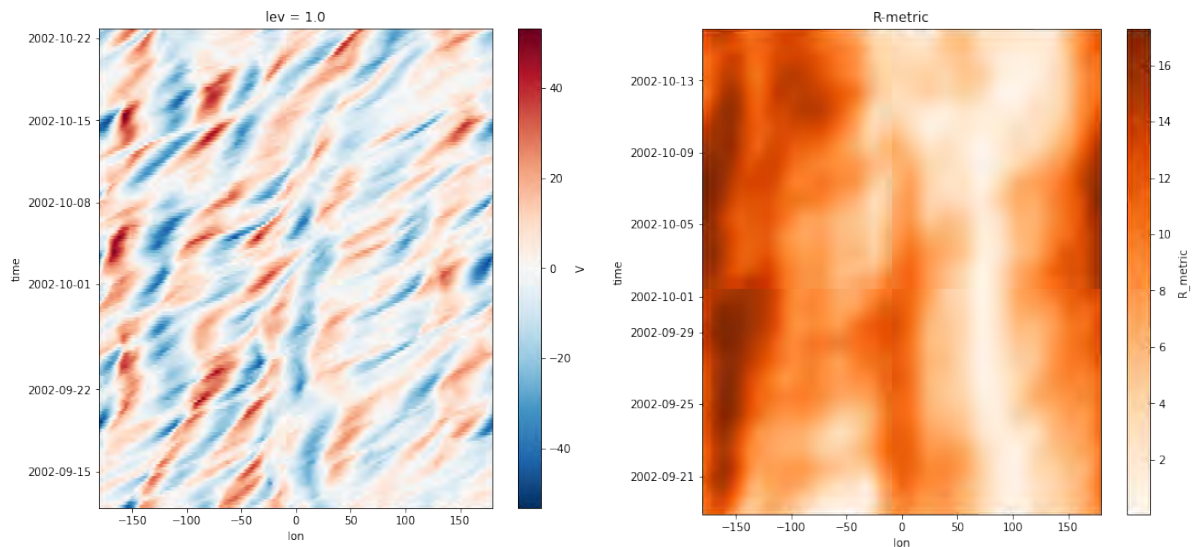
Fig. A1.2: a) Hovmöller Diagram showing the 35° N to 65° N averaged meridional wind V_{ma} at 250 hPa and b) R during the 2002 clustered extreme precipitation event over Switzerland described by Barton et al. (2016).

A2 Supplementary material – Data and Methods

A2.1 – Atlantic European weather regimes

The 7 Atlantic European weather regimes (*AE wr*) are calculated using empirical orthogonal function (EOF) analysis and k-means clustering (Grams et al., 2017). This process is briefly outlined below. For an in-depth description, consult Grams et al. (2017). Anomalies of 10-day-low-pass-filtered geopotential height at 500 hPa (Z500) with regard to a 90-day running mean centred on the respective day are derived. EOF analysis is then applied to these anomalies within 30° N to 90° N and 80° W to 40° E. These anomalies are corrected for a seasonal cycle. This is done by calculating a 30-day running window standard deviation at each gridpoint and for each time step. Then the spatial average, within the domain specified above, of the 30-day running window standard deviation is calculated per timestep and every anomaly is corrected using this spatial average for the respective date. EOF analysis is applied and the first 7 EOFs, which explain 74,4 % of variance, and k-mean-clustering is applied to them. This results in 7 clusters, which correspond to the 7 *AE wr*: Atlantic trough, Zonal regime, Scandinavian trough, Atlantic ridge, European blocking, Scandinavian blocking, Greenland blocking, and no regime.

A daily weather regime index is calculated by projecting the daily Z500 anomaly field (as derived above) onto the clusters (Michel and Rivière, 2011). Higher (positive) values indicate that the spatial correlation of the Z500 anomaly field on a given day to the Z500 field of a given *AE wr* is high, e.g., that day is similar to the Z500 field of a given *AE wr*. Values around 0 indicate that a day is similar to the mean conditions, and lower (negative) values correspond to an opposite pattern. Note that the *AR wr* are valid year-round.
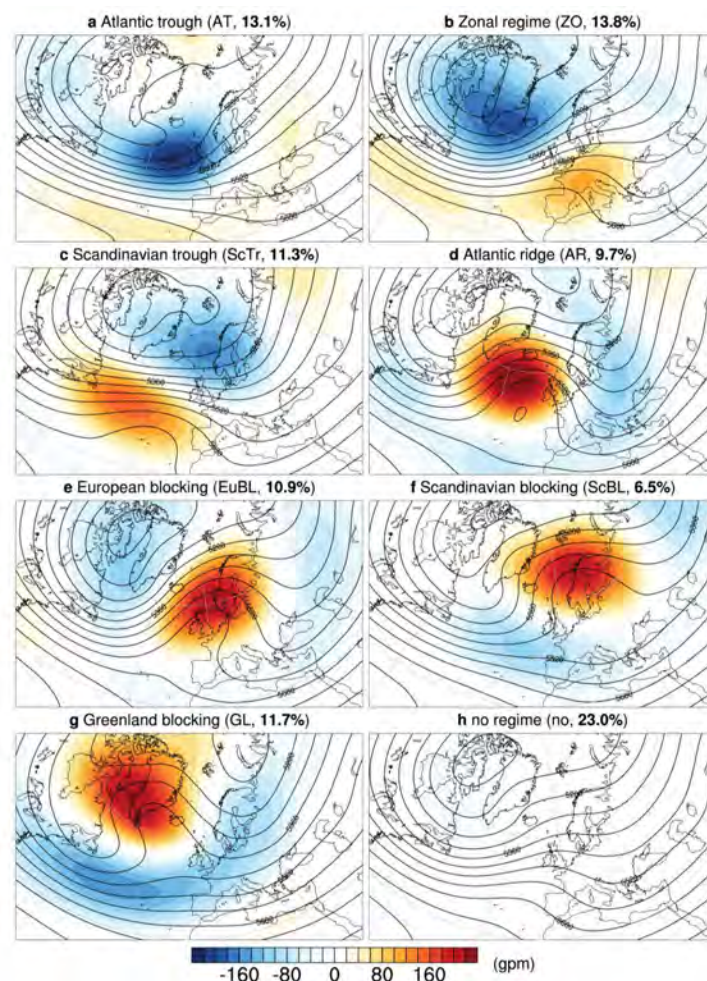
Fig. A2.1: The 7 Atlantic European weather regimes and associated Z500 anomalies as defined by Grams et al. (2017).

A2.2 – Sensitivity tests for α_{PC} in the eastern North Pacific causal network

In this section an insight into the choice of α_{PC} should be given by presenting causal networks for the eastern North Pacific for $\alpha_{PC} = 0.025$ and $\alpha_{PC} = 0.05$. These values can be compared to section A4, which shows the final results used in this work for the causal models in Figs. 13-15 and Figs. 22-24.

This chapter contains the output of PCMCI after the MCI stage and FDR correction of p-values. Presented are the uncorrected p-values from the significance tests of MCI stage (*pval*), the FDR corrected p-values (*qval*), and the link strength (*val*).

Notation is as follows:
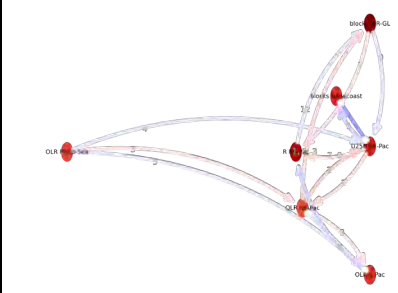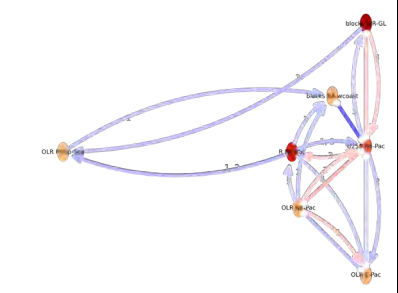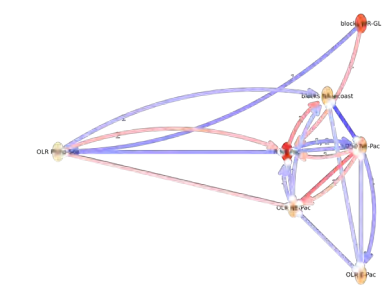
> *Variable R has 12 link(s):*
>
> *(R -1): pval = 0.00000 | qval = 0.00000 | val = 0.887*
>
> *(R -2): pval = 0.00000 | qval = 0.00000 | val = -0.580*
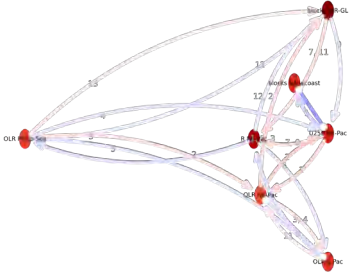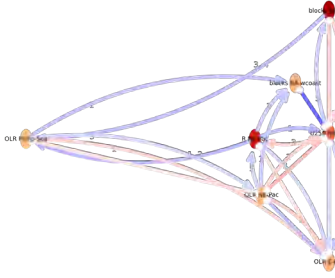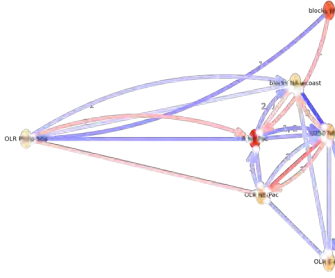
means that *R* has 12 statistically significant links and that the strongest 2 links (the other 10 are not shown here) of the actor *R* are *R* at lag 1 (R -1) and lag 2 (R -2) with *pval*, *qval*, *val* defined as above.

$\alpha_{PC} = 0.025$

Daily	**3-daily**	**6-daily**

## Significant links at alpha = 0.025:	## Significant links at alpha = 0.025:	## Significant links at alpha = 0.025:
Variable R NE-Pac has 12 link(s): 　(R NE-Pac -1): pval = 0.00000 | qval = 0.00000 | val = 0.887 　(R NE-Pac -2): pval = 0.00000 | qval = 0.00000 | val = -0.580 　(R NE-Pac -3): pval = 0.00000 | qval = 0.00000 | val = 0.351 　(R NE-Pac -4): pval = 0.00000 | qval = 0.00000 | val = -0.216 　(R NE-Pac -14): pval = 0.00000 | qval = 0.00000 | val = -0.136 　(R NE-Pac -5): pval = 0.00000 | qval = 0.00000 | val = 0.118 　(OLR E-Pac -6): pval = 0.00000 | qval = 0.00001 | val = -0.087 　(blocks WR-GL -7): pval = 0.00004 | qval = 0.00105 | val = 0.069 　(R NE-Pac -6): pval = 0.00005 | qval = 0.00118 | val = -0.068 　(R NE-Pac -7): pval = 0.00005 | qval = 0.00124 | val = -0.068 　(U250 NE-Pac -7): pval = 0.00011 | qval = 0.00252 | val = 0.065 　(U250 NE-Pac -9): pval = 0.00110 | qval = 0.02165 | val = -0.055 Variable blocks NA-wcoast has 4 link(s): 　(blocks NA-wcoast -1): pval = 0.00000 | qval = 0.00000 | val = 0.761	Variable R NE-Pac has 6 link(s): 　(R NE-Pac -1): pval = 0.00000 | qval = 0.00000 | val = 0.792 　(R NE-Pac -2): pval = 0.00000 | qval = 0.00000 | val = -0.354 　(R NE-Pac -6): pval = 0.00001 | qval = 0.00013 | val = 0.130 　(R NE-Pac -3): pval = 0.00010 | qval = 0.00154 | val = 0.112 　(U250 NE-Pac -3): pval = 0.00078 | qval = 0.00918 | val = 0.097 　(OLR NE-Pac -5): pval = 0.00174 | qval = 0.01709 | val = -0.091 Variable blocks NA-wcoast has 5 link(s): 　(blocks NA-wcoast -1): pval = 0.00000 | qval = 0.00000 | val = 0.395 　(U250 NE-Pac 0): pval = 0.00000 | qval = 0.00000 | val = -0.297 　(OLR Philip-Sea -1): pval = 0.00003 | qval = 0.00044 | val = -0.121 　(R NE-Pac -3): pval = 0.00035 | qval = 0.00450 | val = -0.104 　(OLR NE-Pac -1): pval = 0.00037 | qval = 0.00457 | val = -0.103 Variable blocks WR-GL has 8 link(s): 　(blocks WR-GL -1): pval = 0.00000 | qval = 0.00000 | val = 0.912	Variable R NE-Pac has 10 link(s): 　(R NE-Pac -1): pval = 0.00000 | qval = 0.00000 | val = 0.713 　(R NE-Pac -2): pval = 0.00000 | qval = 0.00000 | val = -0.428 　(R NE-Pac -3): pval = 0.00000 | qval = 0.00000 | val = 0.285 　(OLR Philip-Sea 0): pval = 0.00001 | qval = 0.00001 | val = -0.184 　(U250 NE-Pac 0): pval = 0.00007 | qval = 0.00007 | val = -0.162 　(OLR NE-Pac 0): pval = 0.00034 | qval = 0.00034 | val = -0.147 　(blocks WR-GL -1): pval = 0.00047 | qval = 0.00432 | val = 0.143 　(OLR Philip-Sea -2): pval = 0.00173 | qval = 0.01338 | val = 0.129 　(OLR NE-Pac -3): pval = 0.00214 | qval = 0.01576 | val = -0.126 　(U250 NE-Pac -1): pval = 0.00355 | qval = 0.02267 | val = 0.120 Variable blocks NA-wcoast has 6 link(s): 　(U250 NE-Pac 0): pval = 0.00000 | qval = 0.00000 | val = -0.306 　(blocks NA-wcoast -1): pval = 0.00000 | qval = 0.00000 | val = 0.303 　(R NE-Pac -1): pval = 0.00000 | qval = 0.00005 | val = 0.189

(blocks NA-wcoast -2): pval = 0.00000 | qval = 0.00000 | val = -0.324
(U250 NE-Pac 0) pval = 0.00000 | qval = 0.00000 | val = -0.188
(U250 NE-Pac -1) pval = 0.00000 | qval = 0.00000 | val = -0.092

Variable blocks WR-GL has 14 link(s):
(blocks WR-GL -1): pval = 0.00000 | qval = 0.00000 | val = 0.978
(blocks WR-GL -2): pval = 0.00000 | qval = 0.00000 | val = -0.882
(blocks WR-GL -3): pval = 0.00000 | qval = 0.00000 | val = 0.628
(blocks WR-GL -4): pval = 0.00000 | qval = 0.00000 | val = -0.175
(blocks WR-GL -7): pval = 0.00000 | qval = 0.00000 | val = 0.151
(blocks WR-GL -5): pval = 0.00000 | qval = 0.00000 | val = -0.141
(blocks WR-GL -6): pval = 0.00000 | qval = 0.00000 | val = 0.100
(blocks WR-GL -19): pval = 0.00000 | qval = 0.00001 | val = -0.087
(blocks WR-GL -9): pval = 0.00000 | qval = 0.00001 | val = -0.086
(OLR NE-Pac -1): pval = 0.00000 | qval = 0.00005 | val = 0.081
(OLR NE-Pac -2): pval = 0.00000 | qval = 0.00010 | val = -0.078
(blocks WR-GL -8): pval = 0.00008 | qval = 0.00196 | val = -0.066
(OLR NE-Pac -3): pval = 0.00009 | qval = 0.00212 | val = 0.066
(R NE-Pac -12): pval = 0.00084 | qval = 0.01719 | val = -0.056

Variable U250 NE-Pac has 8 link(s):
(U250 NE-Pac -1): pval = 0.00000 | qval = 0.00000 | val = 0.781
(U250 NE-Pac -2): pval = 0.00000 | qval = 0.00000 | val = -0.347
(blocks NA-wcoast 0): pval = 0.00000 | qval = 0.00000 | val = -0.188
(U250 NE-Pac -3): pval = 0.00000 | qval = 0.00000 | val = 0.155
(OLR NE-Pac -2): pval = 0.00000 | qval = 0.00000 | val = 0.095
(U250 NE-Pac -4): pval = 0.00004 | qval = 0.00111 | val = -0.069
(OLR Philip-Sea -4): pval = 0.00081 | qval = 0.01683 | val = -0.056
(blocks WR-GL -9): pval = 0.00108 | qval = 0.02151 | val = -0.055

Variable OLR Philip-Sea has 4 link(s):
(OLR Philip-Sea -1): pval = 0.00000 | qval = 0.00000 | val = 0.700
(OLR Philip-Sea -2): pval = 0.00000 | qval = 0.00000 | val = -0.303
(OLR Philip-Sea -3): pval = 0.00000 | qval = 0.00000 | val = 0.141
(OLR Philip-Sea -4): pval = 0.00023 | qval = 0.00504 | val = -0.062

Variable OLR NE-Pac has 6 link(s):
(OLR NE-Pac -1): pval = 0.00000 | qval = 0.00000 | val = 0.677
(OLR NE-Pac -2): pval = 0.00000 | qval = 0.00000 | val = -0.241
(OLR NE-Pac -3): pval = 0.00000 | qval = 0.00000 | val = 0.091
(U250 NE-Pac -1): pval = 0.00001 | qval = 0.00017 | val = 0.076
(OLR Philip-Sea -3): pval = 0.00005 | qval = 0.00119 | val = 0.068
(OLR E-Pac 0): pval = 0.00029 | qval = 0.00029 | val = -0.061

Variable OLR E-Pac has 6 link(s):
(OLR E-Pac -1): pval = 0.00000 | qval = 0.00000 | val = 0.738
(OLR E-Pac -2): pval = 0.00000 | qval = 0.00000 | val = -0.360
(OLR E-Pac -3): pval = 0.00000 | qval = 0.00000 | val = 0.169
(OLR Philip-Sea -5): pval = 0.00023 | qval = 0.00511 | val = -0.062
(OLR NE-Pac 0): pval = 0.00029 | qval = 0.00029 | val = -0.061
(OLR NE-Pac -3): pval = 0.00030 | qval = 0.00633 | val = 0.061

(blocks WR-GL -2): pval = 0.00000 | qval = 0.00000 | val = -0.774
(blocks WR-GL -3): pval = 0.00000 | qval = 0.00000 | val = 0.669
(blocks WR-GL -4): pval = 0.00000 | qval = 0.00000 | val = -0.567
(blocks WR-GL -5): pval = 0.00000 | qval = 0.00000 | val = 0.495
(blocks WR-GL -6): pval = 0.00000 | qval = 0.00000 | val = 0.322
(U250 NE-Pac 0): pval = 0.00047 | qval = 0.00047 | val = 0.101
(U250 NE-Pac -5): pval = 0.00154 | qval = 0.01561 | val = -0.092

Variable U250 NE-Pac has 10 link(s):
(U250 NE-Pac -1): pval = 0.00000 | qval = 0.00000 | val = 0.600
(blocks NA-wcoast 0): pval = 0.00000 | qval = 0.00000 | val = -0.297
(U250 NE-Pac -2): pval = 0.00000 | qval = 0.00000 | val = -0.172
(OLR NE-Pac 0): pval = 0.00000 | qval = 0.00000 | val = 0.137
(R NE-Pac -1): pval = 0.00001 | qval = 0.00013 | val = -0.129
(blocks WR-GL 0): pval = 0.00047 | qval = 0.00047 | val = 0.101
(R NE-Pac -3): pval = 0.00109 | qval = 0.01228 | val = 0.095
(OLR NE-Pac -1): pval = 0.00208 | qval = 0.01973 | val = 0.089
(blocks WR-GL -3): pval = 0.00261 | qval = 0.02396 | val = 0.087
(OLR E-Pac 0): pval = 0.01180 | qval = 0.01180 | val = -0.073

Variable OLR Philip-Sea has 4 link(s):
(OLR Philip-Sea -1): pval = 0.00000 | qval = 0.00000 | val = 0.366
(R NE-Pac -1): pval = 0.00000 | qval = 0.00006 | val = -0.135
(blocks WR-GL -3): pval = 0.00000 | qval = 0.00009 | val = -0.132
(R NE-Pac -2): pval = 0.00142 | qval = 0.01491 | val = 0.093

Variable OLR NE-Pac has 3 link(s):
(OLR NE-Pac -1): pval = 0.00000 | qval = 0.00000 | val = 0.399
(U250 NE-Pac 0): pval = 0.00000 | qval = 0.00000 | val = 0.137
(OLR E-Pac 0): pval = 0.00001 | qval = 0.00001 | val = -0.130

Variable OLR E-Pac has 6 link(s):
(OLR E-Pac -1): pval = 0.00000 | qval = 0.00000 | val = 0.407
(OLR NE-Pac 0): pval = 0.00001 | qval = 0.00001 | val = -0.130
(U250 NE-Pac -2): pval = 0.00011 | qval = 0.00159 | val = -0.112
(OLR NE-Pac -1): pval = 0.00024 | qval = 0.00324 | val = 0.106
(R NE-Pac -2): pval = 0.00115 | qval = 0.01247 | val = -0.094
(U250 NE-Pac 0): pval = 0.01180 | qval = 0.01180 | val = -0.073

(OLR Philip-Sea -1): pval = 0.00069 | qval = 0.00600 | val = -0.139
(OLR NE-Pac -1): pval = 0.00267 | qval = 0.01784 | val = -0.123
(OLR E-Pac 0): pval = 0.00598 | qval = 0.00598 | val = -0.113

Variable blocks WR-GL has 3 link(s):
(blocks WR-GL -1): pval = 0.00000 | qval = 0.00000 | val = 0.620
(blocks WR-GL -2): pval = 0.00000 | qval = 0.00000 | val = -0.217
(blocks WR-GL -3): pval = 0.00257 | qval = 0.01784 | val = 0.124

Variable U250 NE-Pac has 7 link(s):
(U250 NE-Pac -1): pval = 0.00000 | qval = 0.00000 | val = 0.351
(blocks NA-wcoast 0): pval = 0.00000 | qval = 0.00000 | val = -0.306
(OLR NE-Pac 0): pval = 0.00000 | qval = 0.00000 | val = 0.240
(R NE-Pac -1): pval = 0.00000 | qval = 0.00001 | val = -0.200
(R NE-Pac 0): pval = 0.00007 | qval = 0.00007 | val = -0.162
(R NE-Pac -2): pval = 0.00017 | qval = 0.00168 | val = 0.154
(OLR E-Pac 0): pval = 0.00241 | qval = 0.00241 | val = -0.124

Variable OLR Philip-Sea has 4 link(s):
(blocks WR-GL -1): pval = 0.00000 | qval = 0.00002 | val = -0.198
(R NE-Pac 0): pval = 0.00001 | qval = 0.00001 | val = -0.184
(OLR Philip-Sea -1): pval = 0.00001 | qval = 0.00015 | val = 0.178
(OLR NE-Pac 0): pval = 0.01119 | qval = 0.01119 | val = 0.104

Variable OLR NE-Pac has 6 link(s):
(OLR NE-Pac -1): pval = 0.00000 | qval = 0.00000 | val = 0.341
(U250 NE-Pac 0): pval = 0.00000 | qval = 0.00000 | val = 0.240
(R NE-Pac 0): pval = 0.00034 | qval = 0.00034 | val = -0.147
(OLR E-Pac 0): pval = 0.00118 | qval = 0.00118 | val = -0.133
(U250 NE-Pac -1): pval = 0.00130 | qval = 0.01062 | val = 0.132
(OLR Philip-Sea 0): pval = 0.01119 | qval = 0.01119 | val = 0.104

Variable OLR E-Pac has 5 link(s):
(OLR E-Pac -1): pval = 0.00000 | qval = 0.00000 | val = 0.314
(U250 NE-Pac -1): pval = 0.00002 | qval = 0.00020 | val = -0.175
(OLR NE-Pac 0): pval = 0.00118 | qval = 0.00118 | val = -0.133
(U250 NE-Pac 0): pval = 0.00241 | qval = 0.00241 | val = -0.124
(blocks NA-wcoast 0): pval = 0.00598 | qval = 0.00598 | val = -0.113

$\alpha_{PC} = 0.05$

Daily	3-daily	6-daily

Daily

Significant links at alpha = 0.05:

Variable R NE-Pac has 13 link(s):
    (R NE-Pac -1): pval = 0.00000 | qval = 0.00000 | val = 0.887
    (R NE-Pac -2): pval = 0.00000 | qval = 0.00000 | val = -0.580
    (R NE-Pac -3): pval = 0.00000 | qval = 0.00000 | val = 0.349
    (R NE-Pac -4): pval = 0.00000 | qval = 0.00000 | val = -0.216
    (R NE-Pac -14): pval = 0.00000 | qval = 0.00000 | val = -0.135
    (R NE-Pac -5): pval = 0.00000 | qval = 0.00000 | val = 0.119
    (blocks WR-GL -7): pval = 0.00003 | qval = 0.00073 | val = 0.071
    (R NE-Pac -6): pval = 0.00004 | qval = 0.00108 | val = -0.069
    (R NE-Pac -7): pval = 0.00005 | qval = 0.00120 | val = -0.068
    (OLR E-Pac -6): pval = 0.00009 | qval = 0.00211 | val = -0.066
    (U250 NE-Pac -7): pval = 0.00010 | qval = 0.00216 | val = 0.066
    (U250 NE-Pac -9): pval = 0.00123 | qval = 0.02297 | val = -0.054
    (blocks WR-GL -11): pval = 0.00188 | qval = 0.03286 | val = 0.052

Variable blocks NA-wcoast has 5 link(s):
    (blocks NA-wcoast -1): pval = 0.00000 | qval = 0.00000 | val = 0.760
    (blocks NA-wcoast -2): pval = 0.00000 | qval = 0.00000 | val = -0.324
    (U250 NE-Pac 0): pval = 0.00000 | qval = 0.00000 | val = -0.189
    (U250 NE-Pac -1): pval = 0.00000 | qval = 0.00000 | val = -0.093
    (blocks NA-wcoast -3): pval = 0.00175 | qval = 0.03125 | val = 0.053

Variable blocks WR-GL has 17 link(s):
    (blocks WR-GL -1): pval = 0.00000 | qval = 0.00000 | val = 0.978
    (blocks WR-GL -2): pval = 0.00000 | qval = 0.00000 | val = -0.882
    (blocks WR-GL -3): pval = 0.00000 | qval = 0.00000 | val = 0.628
    (blocks WR-GL -4): pval = 0.00000 | qval = 0.00000 | val = -0.175
    (blocks WR-GL -7): pval = 0.00000 | qval = 0.00000 | val = 0.151
    (blocks WR-GL -5): pval = 0.00000 | qval = 0.00000 | val = -0.141
    (blocks WR-GL -6): pval = 0.00000 | qval = 0.00000 | val = 0.100
    (blocks WR-GL -19): pval = 0.00000 | qval = 0.00001 | val = -0.087
    (blocks WR-GL -9): pval = 0.00000 | qval = 0.00001 | val = -0.086
    (OLR NE-Pac -1): pval = 0.00000 | qval = 0.00004 | val = 0.081
    (OLR NE-Pac -2): pval = 0.00001 | qval = 0.00017 | val = -0.076
    (OLR NE-Pac -3): pval = 0.00006 | qval = 0.00154 | val = 0.067
    (blocks WR-GL -8): pval = 0.00008 | qval = 0.00191 | val = -0.066
    (R NE-Pac -12): pval = 0.00115 | qval = 0.02244 | val = -0.055
    (blocks WR-GL -11): pval = 0.00140 | qval = 0.02545 | val = 0.054
    (OLR Philip-Sea -13): pval = 0.00240 | qval = 0.03979 | val = 0.051
    (R NE-Pac -2): pval = 0.00290 | qval = 0.04665 | val = -0.050

3-daily

Significant links at alpha = 0.05:

Variable R NE-Pac has 7 link(s):
    (R NE-Pac -1): pval = 0.00000 | qval = 0.00000 | val = 0.791
    (R NE-Pac -2): pval = 0.00000 | qval = 0.00000 | val = -0.352
    (R NE-Pac -6): pval = 0.00001 | qval = 0.00016 | val = 0.128
    (R NE-Pac -3): pval = 0.00012 | qval = 0.00183 | val = 0.111
    (OLR NE-Pac -5): pval = 0.00206 | qval = 0.02085 | val = -0.090
    (U250 NE-Pac -3): pval = 0.00225 | qval = 0.02190 | val = 0.089
    (OLR E-Pac 0): pval = 0.03558 | qval = 0.03558 | val = 0.061

Variable blocks NA-wcoast has 5 link(s):
    (blocks NA-wcoast -1): pval = 0.00000 | qval = 0.00000 | val = 0.395
    (U250 NE-Pac 0): pval = 0.00000 | qval = 0.00000 | val = -0.296
    (OLR Philip-Sea -1): pval = 0.00004 | qval = 0.00057 | val = -0.120
    (OLR NE-Pac -1): pval = 0.00040 | qval = 0.00513 | val = -0.103
    (R NE-Pac -3): pval = 0.00045 | qval = 0.00557 | val = -0.102

Variable blocks WR-GL has 8 link(s):
    (blocks WR-GL -1): pval = 0.00000 | qval = 0.00000 | val = 0.912
    (blocks WR-GL -2): pval = 0.00000 | qval = 0.00000 | val = -0.774
    (blocks WR-GL -3): pval = 0.00000 | qval = 0.00000 | val = 0.669
    (blocks WR-GL -4): pval = 0.00000 | qval = 0.00000 | val = -0.567
    (blocks WR-GL -5): pval = 0.00000 | qval = 0.00000 | val = 0.495
    (blocks WR-GL -6): pval = 0.00000 | qval = 0.00000 | val = 0.322
    (U250 NE-Pac 0): pval = 0.00057 | qval = 0.00057 | val = 0.100
    (U250 NE-Pac -5): pval = 0.00087 | qval = 0.01023 | val = -0.097

Variable U250 NE-Pac has 9 link(s):
    (U250 NE-Pac -1): pval = 0.00000 | qval = 0.00000 | val = 0.592
    (blocks NA-wcoast 0): pval = 0.00000 | qval = 0.00000 | val = -0.296
    (U250 NE-Pac -2): pval = 0.00000 | qval = 0.00000 | val = -0.175
    (OLR NE-Pac 0): pval = 0.00000 | qval = 0.00000 | val = 0.137
    (R NE-Pac -1): pval = 0.00001 | qval = 0.00014 | val = -0.129
    (blocks WR-GL 0): pval = 0.00057 | qval = 0.00057 | val = 0.100
    (blocks WR-GL -3): pval = 0.00231 | qval = 0.02190 | val = 0.089
    (OLR NE-Pac -1): pval = 0.00300 | qval = 0.02677 | val = 0.086
    (OLR E-Pac 0): pval = 0.00968 | qval = 0.00968 | val = -0.075

Variable OLR Philip-Sea has 6 link(s):
    (OLR Philip-Sea -1): pval = 0.00000 | qval = 0.00000 | val = 0.359
    (R NE-Pac -1): pval = 0.00000 | qval = 0.00006 | val = -0.135
    (blocks WR-GL -3): pval = 0.00000 | qval = 0.00009 | val = -0.132
    (blocks WR-GL -4): pval = 0.00109 | qval = 0.01232 | val = 0.095

6-daily

Significant links at alpha = 0.05:

Variable R NE-Pac has 10 link(s):
    (R NE-Pac -1): pval = 0.00000 | qval = 0.00000 | val = 0.712
    (R NE-Pac -2): pval = 0.00000 | qval = 0.00000 | val = -0.426
    (R NE-Pac -3): pval = 0.00000 | qval = 0.00000 | val = 0.275
    (OLR Philip-Sea 0): pval = 0.00001 | qval = 0.00001 | val = -0.184
    (U250 NE-Pac 0): pval = 0.00004 | qval = 0.00004 | val = -0.169
    (OLR NE-Pac 0): pval = 0.00035 | qval = 0.00035 | val = -0.146
    (blocks WR-GL -1): pval = 0.00046 | qval = 0.00422 | val = 0.144
    (OLR NE-Pac -3): pval = 0.00214 | qval = 0.01659 | val = -0.126
    (OLR Philip-Sea -2): pval = 0.00234 | qval = 0.01717 | val = 0.125
    (blocks NA-wcoast 0): pval = 0.02097 | qval = 0.02097 | val = 0.095

Variable blocks NA-wcoast has 9 link(s):
    (U250 NE-Pac 0): pval = 0.00000 | qval = 0.00000 | val = -0.323
    (blocks NA-wcoast -1): pval = 0.00000 | qval = 0.00000 | val = 0.257
    (R NE-Pac -2): pval = 0.00007 | qval = 0.00071 | val = -0.164
    (R NE-Pac -1): pval = 0.00027 | qval = 0.00263 | val = 0.150
    (U250 NE-Pac -2): pval = 0.00382 | qval = 0.02554 | val = 0.119
    (OLR Philip-Sea -1): pval = 0.00780 | qval = 0.04776 | val = -0.109
    (OLR E-Pac 0): pval = 0.01172 | qval = 0.01172 | val = -0.104
    (R NE-Pac 0): pval = 0.02097 | qval = 0.02097 | val = 0.095
    (OLR Philip-Sea 0): pval = 0.04293 | qval = 0.04293 | val = -0.083

Variable blocks WR-GL has 3 link(s):
    (blocks WR-GL -1): pval = 0.00000 | qval = 0.00000 | val = 0.620
    (blocks WR-GL -2): pval = 0.00000 | qval = 0.00000 | val = -0.217
    (blocks WR-GL -3): pval = 0.00257 | qval = 0.01799 | val = 0.124

Variable U250 NE-Pac has 8 link(s):
    (U250 NE-Pac -1): pval = 0.00000 | qval = 0.00000 | val = 0.341
    (blocks NA-wcoast 0): pval = 0.00000 | qval = 0.00000 | val = -0.323
    (OLR NE-Pac 0): pval = 0.00000 | qval = 0.00000 | val = 0.237
    (R NE-Pac -1): pval = 0.00000 | qval = 0.00001 | val = -0.205
    (R NE-Pac 0): pval = 0.00004 | qval = 0.00004 | val = -0.169
    (R NE-Pac -2): pval = 0.00065 | qval = 0.00559 | val = 0.140
    (OLR E-Pac 0): pval = 0.00440 | qval = 0.00440 | val = -0.117
    (OLR NE-Pac -2): pval = 0.00656 | qval = 0.04191 | val = -0.112

Variable OLR Philip-Sea has 5 link(s):
    (blocks WR-GL -1): pval = 0.00000 | qval = 0.00002 | val = -0.198
    (R NE-Pac 0): pval = 0.00001 | qval = 0.00001 | val = -0.184
    (OLR Philip-Sea -1): pval = 0.00001 | qval = 0.00017 | val = 0.178

Variable U250 NE-Pac has 8 link(s):
    (U250 NE-Pac -1): pval = 0.00000 | qval = 0.00000 | val = 0.781
    (U250 NE-Pac -2): pval = 0.00000 | qval = 0.00000 | val = -0.345
    (blocks NA-wcoast 0): pval = 0.00000 | qval = 0.00000 | val = -0.189
    (U250 NE-Pac -3): pval = 0.00000 | qval = 0.00000 | val = 0.155
    (OLR NE-Pac -2): pval = 0.00000 | qval = 0.00000 | val = 0.098
    (U250 NE-Pac -4): pval = 0.00004 | qval = 0.00096 | val = -0.069
    (OLR Philip-Sea -4): pval = 0.00081 | qval = 0.01621 | val = -0.056
    (blocks WR-GL -9): pval = 0.00123 | qval = 0.02297 | val = -0.054

Variable OLR Philip-Sea has 7 link(s):
    (OLR Philip-Sea -1): pval = 0.00000 | qval = 0.00000 | val = 0.700
    (OLR Philip-Sea -2): pval = 0.00000 | qval = 0.00000 | val = -0.304
    (OLR Philip-Sea -3): pval = 0.00000 | qval = 0.00000 | val = 0.142
    (R NE-Pac -2): pval = 0.00004 | qval = 0.00104 | val = -0.069
    (OLR Philip-Sea -4): pval = 0.00023 | qval = 0.00498 | val = -0.062
    (OLR Philip-Sea -9): pval = 0.00196 | qval = 0.03375 | val = -0.052
    (blocks WR-GL -12): pval = 0.00206 | qval = 0.03485 | val = -0.052

Variable OLR NE-Pac has 7 link(s):
    (OLR NE-Pac -1): pval = 0.00000 | qval = 0.00000 | val = 0.676
    (OLR NE-Pac -2): pval = 0.00000 | qval = 0.00000 | val = -0.240
    (OLR NE-Pac -3): pval = 0.00000 | qval = 0.00000 | val = 0.091
    (U250 NE-Pac -1): pval = 0.00000 | qval = 0.00006 | val = 0.080
    (OLR Philip-Sea -3): pval = 0.00003 | qval = 0.00090 | val = 0.070
    (OLR E-Pac 0): pval = 0.00018 | qval = 0.00018 | val = -0.063
    (OLR E-Pac -11): pval = 0.00269 | qval = 0.04393 | val = 0.050

Variable OLR E-Pac has 8 link(s):
    (OLR E-Pac -1): pval = 0.00000 | qval = 0.00000 | val = 0.735
    (OLR E-Pac -2): pval = 0.00000 | qval = 0.00000 | val = -0.359
    (OLR E-Pac -3): pval = 0.00000 | qval = 0.00000 | val = 0.168
    (OLR NE-Pac 0): pval = 0.00018 | qval = 0.00018 | val = -0.063
    (OLR NE-Pac -3): pval = 0.00025 | qval = 0.00522 | val = 0.062
    (OLR Philip-Sea -5): pval = 0.00043 | qval = 0.00905 | val = -0.059
    (R NE-Pac -6): pval = 0.00069 | qval = 0.01418 | val = -0.057
    (OLR NE-Pac -4): pval = 0.00124 | qval = 0.02297 | val = 0.054

    (R NE-Pac -2): pval = 0.00146 | qval = 0.01583 | val = 0.092
    (OLR NE-Pac 0): pval = 0.03414 | qval = 0.03414 | val = 0.062

Variable OLR NE-Pac has 5 link(s):
    (OLR NE-Pac -1): pval = 0.00000 | qval = 0.00000 | val = 0.399
    (U250 NE-Pac 0): pval = 0.00000 | qval = 0.00000 | val = 0.137
    (OLR E-Pac 0): pval = 0.00000 | qval = 0.00000 | val = -0.133
    (OLR Philip-Sea -3): pval = 0.00351 | qval = 0.03037 | val = -0.085
    (OLR Philip-Sea 0): pval = 0.03414 | qval = 0.03414 | val = 0.062

Variable OLR E-Pac has 8 link(s):
    (OLR E-Pac -1): pval = 0.00000 | qval = 0.00000 | val = 0.407
    (OLR NE-Pac 0): pval = 0.00000 | qval = 0.00000 | val = -0.133
    (OLR NE-Pac -1): pval = 0.00028 | qval = 0.00397 | val = 0.105
    (U250 NE-Pac -2): pval = 0.00040 | qval = 0.00513 | val = -0.103
    (R NE-Pac -2): pval = 0.00151 | qval = 0.01583 | val = -0.092
    (OLR Philip-Sea -1): pval = 0.00244 | qval = 0.02238 | val = 0.088
    (U250 NE-Pac 0): pval = 0.00968 | qval = 0.00968 | val = -0.075
    (R NE-Pac 0): pval = 0.03558 | qval = 0.03558 | val = 0.061

    (OLR NE-Pac 0): pval = 0.01119 | qval = 0.01119 | val = 0.104
    (blocks NA-wcoast 0): pval = 0.04293 | qval = 0.04293 | val = -0.083

Variable OLR NE-Pac has 6 link(s):
    (OLR NE-Pac -1): pval = 0.00000 | qval = 0.00000 | val = 0.341
    (U250 NE-Pac 0): pval = 0.00000 | qval = 0.00000 | val = 0.237
    (R NE-Pac 0): pval = 0.00035 | qval = 0.00035 | val = -0.146
    (OLR E-Pac 0): pval = 0.00064 | qval = 0.00064 | val = -0.140
    (U250 NE-Pac -1): pval = 0.00135 | qval = 0.01104 | val = 0.132
    (OLR Philip-Sea 0): pval = 0.01119 | qval = 0.01119 | val = 0.104

Variable OLR E-Pac has 5 link(s):
    (OLR E-Pac -1): pval = 0.00000 | qval = 0.00000 | val = 0.308
    (U250 NE-Pac -1): pval = 0.00002 | qval = 0.00028 | val = -0.173
    (OLR NE-Pac 0): pval = 0.00064 | qval = 0.00064 | val = -0.140
    (U250 NE-Pac 0): pval = 0.00440 | qval = 0.00440 | val = -0.117
    (blocks NA-wcoast 0): pval = 0.01172 | qval = 0.01172 | val = -0.104

A3 – Supplementary material – Results and Discussion

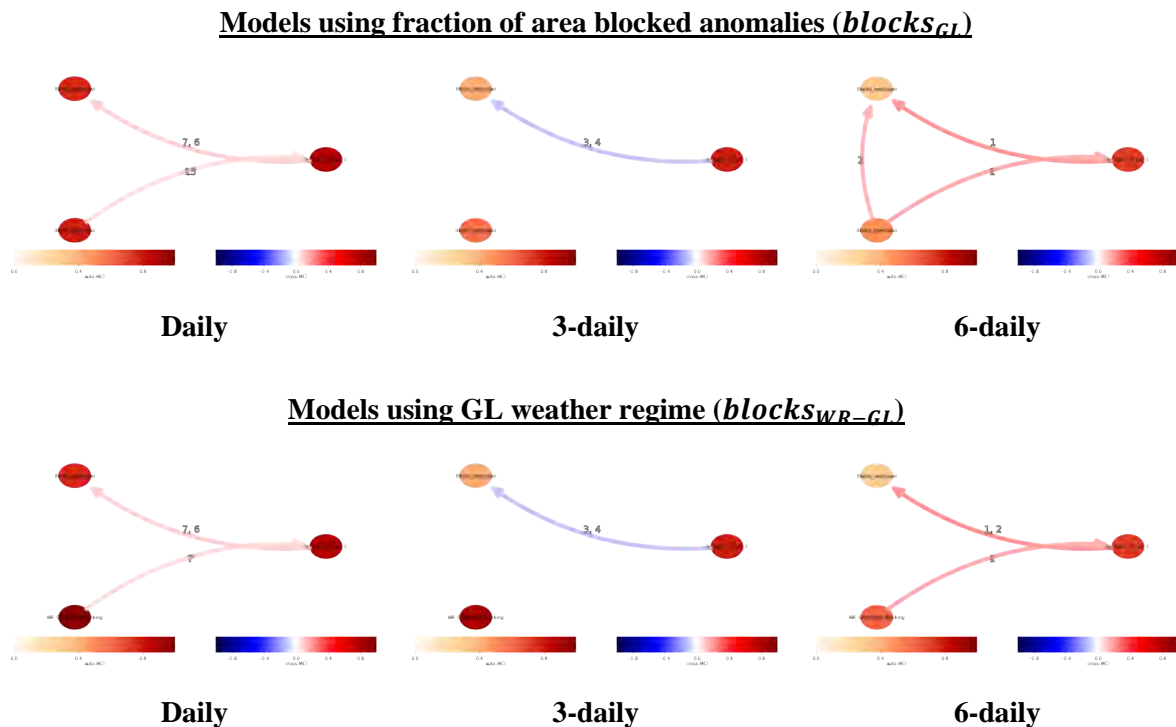## A3.1 – *R* anomalies during high and extremely high *R* days in the North Atlantic
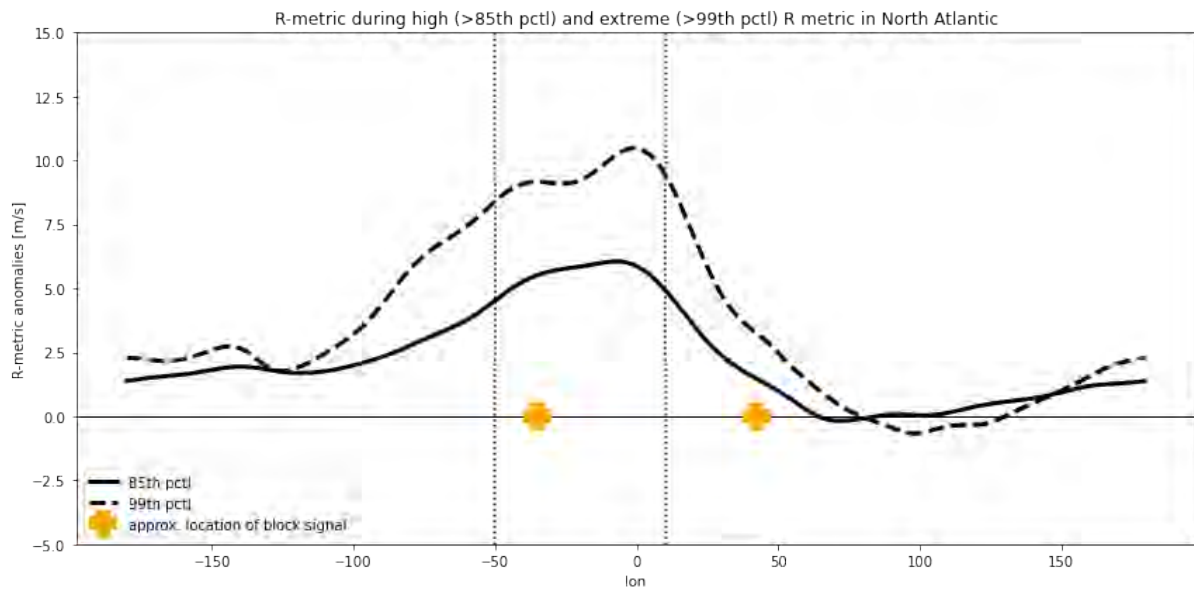
Fig. A3.1: *R* anomalies during high (85th percentile; solid line) and extremely high (99th percentile; dashed line) *R* values in the North Atlantic basin (50° W to 10° E; longitudes marked in vertical dotted lines). The approximate location of the two blocking features examined in this work ($blocks_{N-Atl}$ at 40° W and $blocks_{Scand}$ at 40° E) are marked by orange crosses. This shows that $blocks_{N-Atl}$ is to a large degree upstream of the highest *R* anomalies during high *R* events in the North Atlantic.

A3.2 – R anomalies during high and extremely high R days in studied basins

To test whether using the *GL* weather regime instead of an actor based on anomaly of fraction of area blocked would provide similar results, PCMCI models for the eastern North Pacific using both options were run. These smaller models included R_{NE-Pac}, $blocks_{NA-wcoast}$, and either $blocks_{WR-GL}$ or $blocks_{GL}$, which is an actor derived from anomaly of fraction of area blocked over 58° N to 75° N, 70° W to 25° W. All PCMCI runs used $\alpha_{PC} = 0.01$, $\alpha_{FDR} = 0.01$, and $\tau_{max} = 20$, 6, or 3 for the daily, 3-daily, or 6-daily model respectively.

The causal networks based on the fraction of area blocked actor ($blocks_{GL}$) and the Greenland blocking weather regime ($blocks_{WR-GL}$) are very similar. The main differences are the higher autocorrelation in the GL weather regime and that in the daily model with $blocks_{WR-GL}$ the link $blocks_{WR-GL}$ to R_{NE-Pac} is at 7 days with strength 0.070 (compared to 15 days and 0.064 using $blocks_{GL}$). There is also the absence of a link from $blocks_{WR-GL}$ to $blocks_{NA-wcoast}$ in the 6-daily model. The 6-daily model using $blocks_{WR-GL}$ shows a negative link $R_{NE-Pac} \rightarrow blocks_{NA-wcoast}$ at lag 2 (-0.184). This agrees with the negative links at lags 3,4 detected in the 3-daily model. Therefore, for further analyses the GL weather regime was used instead of the fraction of area blocked anomalies over Greenland. Using a defined index should facilitate comparisons to other studies using the weather regimes and helps to explore their use in causal inference methods.

Models using fraction of area blocked anomalies ($\boldsymbol{blocks_{GL}}$)

| **Daily** | **3-daily** | **6-daily** |

Models using GL weather regime ($\boldsymbol{blocks_{WR-GL}}$)

| **Daily** | **3-daily** | **6-daily** |

Figure A3.3: Comparison of causal models using $blocks_{GL}$ (top row) and $blocks_{WR-GL}$ (bottom row) for daily (1st column), 3-daily (2nd column), and 6-daily (3rd column) models.

A3.3 – Preliminary testing of OLR_{Carib} in smaller models

To examine whether an actor should be considered in the full model of PCMCI, preliminary examination in PCMCI using only R_{NE-Pac}, the blocking actors, and the investigated actor was carried out. In this section a preliminary analysis of OLR in the Caribbean, OLR_{Carib}, is shown to support the decision of not including it in the full causal model presented in Figs. 22 – 24. Coordinates over which OLR was averaged to derive OLR_{Carib} are 13° N - 23° N, 105° W - 75° W. All PCMCI runs used α_{PC} = 0.01, α_{FDR} = 0.01, and τ_{max} = 20, 6, or 3 for the daily, 3-daily, or 6-daily model respectively. Notation is as in A2.2.

Daily model

Significant links at alpha = 0.01:

Variable R NE-Pac has 10 link(s):
    (R NE-Pac -1): pval = 0.00000 | qval = 0.00000 | val = 0.888
    (R NE-Pac -2): pval = 0.00000 | qval = 0.00000 | val = -0.580
    (R NE-Pac -3): pval = 0.00000 | qval = 0.00000 | val = 0.352
    (R NE-Pac -4): pval = 0.00000 | qval = 0.00000 | val = -0.216
    (R NE-Pac -14): pval = 0.00000 | qval = 0.00000 | val = -0.142
    (R NE-Pac -5): pval = 0.00000 | qval = 0.00000 | val = 0.119
    (OLR_carib 0): pval = 0.00000 | qval = 0.00000 | val = -0.083
    (R NE-Pac -7): pval = 0.00003 | qval = 0.00037 | val = -0.070
    (blocks WR-GL -7): pval = 0.00003 | qval = 0.00037 | val = 0.070
    (R NE-Pac -6): pval = 0.00005 | qval = 0.00052 | val = -0.068

Variable blocks NA-wcoast has 4 link(s):
    (blocks NA-wcoast -1): pval = 0.00000 | qval = 0.00000 | val = 0.765
    (blocks NA-wcoast -2): pval = 0.00000 | qval = 0.00000 | val = -0.325
    (R NE-Pac -7): pval = 0.00000 | qval = 0.00000 | val = 0.089
    (R NE-Pac -6): pval = 0.00001 | qval = 0.00010 | val = 0.075

Variable blocks WR-GL has 14 link(s):
    (blocks WR-GL -1): pval = 0.00000 | qval = 0.00000 | val = 0.978
    (blocks WR-GL -2): pval = 0.00000 | qval = 0.00000 | val = -0.882
    (blocks WR-GL -3): pval = 0.00000 | qval = 0.00000 | val = 0.628
    (OLR_carib -2): pval = 0.00000 | qval = 0.00000 | val = 0.216
    (blocks WR-GL -4): pval = 0.00000 | qval = 0.00000 | val = -0.175
    (blocks WR-GL -7): pval = 0.00000 | qval = 0.00000 | val = 0.151
    (OLR_carib -1): pval = 0.00000 | qval = 0.00000 | val = -0.148
    (blocks WR-GL -5): pval = 0.00000 | qval = 0.00000 | val = -0.141
    (OLR_carib -3): pval = 0.00000 | qval = 0.00000 | val = -0.109
    (blocks WR-GL -6): pval = 0.00000 | qval = 0.00000 | val = 0.100
    (blocks WR-GL -19): pval = 0.00000 | qval = 0.00000 | val = -0.087
    (blocks WR-GL -9): pval = 0.00000 | qval = 0.00000 | val = -0.086
    (OLR_carib 0): pval = 0.00001 | qval = 0.00001 | val = 0.075
    (blocks WR-GL -8): pval = 0.00008 | qval = 0.00090 | val = -0.066

Variable OLR_carib has 6 link(s):
    (OLR_carib -1): pval = 0.00000 | qval = 0.00000 | val = 0.731
    (OLR_carib -2): pval = 0.00000 | qval = 0.00000 | val = -0.269
    (OLR_carib -3): pval = 0.00000 | qval = 0.00000 | val = 0.119
    (R NE-Pac 0): pval = 0.00000 | qval = 0.00000 | val = -0.083
    (blocks WR-GL 0): pval = 0.00001 | qval = 0.00001 | val = 0.075
    (R NE-Pac -9): pval = 0.00090 | qval = 0.00957 | val = -0.056
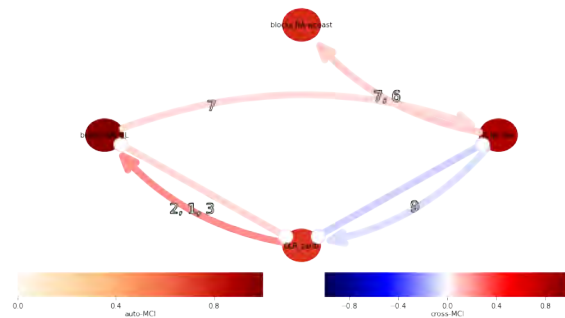
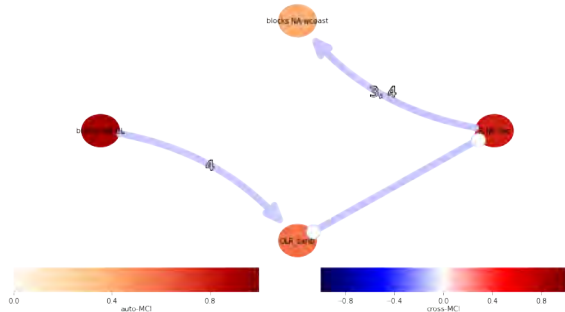**3-daily model**

Significant links at alpha = 0.01:

Variable R NE-Pac has 5 link(s):
    (R NE-Pac -1): pval = 0.00000 | qval = 0.00000 | val = 0.792
    (R NE-Pac -2): pval = 0.00000 | qval = 0.00000 | val = -0.354
    (R NE-Pac -6): pval = 0.00001 | qval = 0.00006 | val = 0.130
    (R NE-Pac -3): pval = 0.00010 | qval = 0.00077 | val = 0.112
    (OLR_carib 0): pval = 0.00020 | qval = 0.00020 | val = -0.108

Variable blocks NA-wcoast has 3 link(s):
    (blocks NA-wcoast -1): pval = 0.00000 | qval = 0.00000 | val = 0.410
    (R NE-Pac -3): pval = 0.00031 | qval = 0.00213 | val = -0.105
    (R NE-Pac -4): pval = 0.00158 | qval = 0.00945 | val = -0.092

Variable blocks WR-GL has 6 link(s):
    (blocks WR-GL -1): pval = 0.00000 | qval = 0.00000 | val = 0.913
    (blocks WR-GL -2): pval = 0.00000 | qval = 0.00000 | val = -0.775
    (blocks WR-GL -3): pval = 0.00000 | qval = 0.00000 | val = 0.668
    (blocks WR-GL -4): pval = 0.00000 | qval = 0.00000 | val = -0.566
    (blocks WR-GL -5): pval = 0.00000 | qval = 0.00000 | val = 0.495
    (blocks WR-GL -6): pval = 0.00000 | qval = 0.00000 | val = 0.324

Variable OLR_carib has 4 link(s):
    (OLR_carib -1): pval = 0.00000 | qval = 0.00000 | val = 0.579
    (OLR_carib -2): pval = 0.00000 | qval = 0.00000 | val = -0.151
    (R NE-Pac 0): pval = 0.00020 | qval = 0.00020 | val = -0.108
    (blocks WR-GL -4): pval = 0.00059 | qval = 0.00377 | val = -0.100
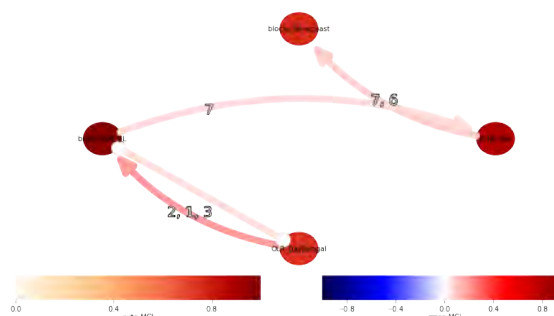
6-daily model

Significant links at alpha = 0.01:

Variable R NE-Pac has 5 link(s):
    (R NE-Pac -1): pval = 0.00000 | qval = 0.00000 | val = 0.712
    (R NE-Pac -2): pval = 0.00000 | qval = 0.00000 | val = -0.438
    (R NE-Pac -3): pval = 0.00000 | qval = 0.00000 | val = 0.289
    (blocks WR-GL -1): pval = 0.00022 | qval = 0.00104 | val = 0.151
    (OLR_carib 0): pval = 0.00181 | qval = 0.00181 | val = -0.128

Variable blocks NA-wcoast has 3 link(s):
    (blocks NA-wcoast -1): pval = 0.00000 | qval = 0.00000 | val = 0.278
    (R NE-Pac -1): pval = 0.00000 | qval = 0.00001 | val = 0.196
    (R NE-Pac -2): pval = 0.00001 | qval = 0.00004 | val = -0.184

Variable blocks WR-GL has 3 link(s):
    (blocks WR-GL -1): pval = 0.00000 | qval = 0.00000 | val = 0.623
    (blocks WR-GL -2): pval = 0.00000 | qval = 0.00000 | val = -0.225
    (blocks WR-GL -3): pval = 0.00184 | qval = 0.00802 | val = 0.128

Variable OLR_carib has 2 link(s):
    (OLR_carib -1): pval = 0.00000 | qval = 0.00000 | val = 0.431
    (R NE-Pac 0): pval = 0.00181 | qval = 0.00181 | val = -0.128
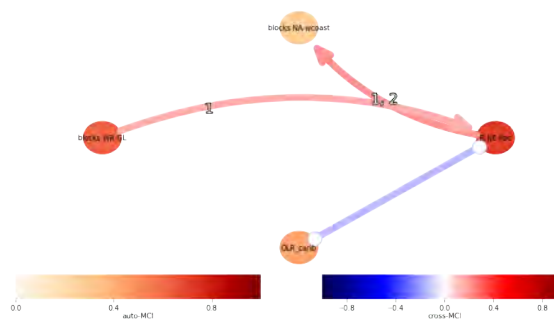
A3.4 – Preliminary testing of $OLR_{Bay-Bengal}$ in smaller models

To examine whether an actor should be considered in the full model of PCMCI, preliminary examination in PCMCI using only R_{NE-Pac}, the blocking actors, and the investigated actor was carried out. In this section a preliminary analysis of OLR over the Bay of Bengal, $OLR_{Bay-Bengal}$, is shown to support the decision of not including it in the full causal model presented in Figs. 22 – 24. Coordinates over which OLR was averaged to derive $OLR_{Bay-Bengal}$ are 3° N – 13° N, 80° E – 115° E. All PCMCI runs used $\alpha_{PC} = 0.01$, $\alpha_{FDR} = 0.01$, and τ_{max} = 20, 6, or 3 for the daily, 3-daily, or 6-daily model respectively. Notation is as in A2.2.

Daily model

Significant links at alpha = 0.01:

Variable R NE-Pac has 9 link(s):
    (R NE-Pac -1): pval = 0.00000 | qval = 0.00000 | val = 0.888
    (R NE-Pac -2): pval = 0.00000 | qval = 0.00000 | val = -0.580
    (R NE-Pac -3): pval = 0.00000 | qval = 0.00000 | val = 0.352
    (R NE-Pac -4): pval = 0.00000 | qval = 0.00000 | val = -0.216
    (R NE-Pac -14): pval = 0.00000 | qval = 0.00000 | val = -0.142
    (R NE-Pac -5): pval = 0.00000 | qval = 0.00000 | val = 0.119
    (R NE-Pac -7): pval = 0.00003 | qval = 0.00038 | val = -0.070
    (blocks WR-GL -7): pval = 0.00003 | qval = 0.00038 | val = 0.070
    (R NE-Pac -6): pval = 0.00005 | qval = 0.00054 | val = -0.068

Variable blocks NA-wcoast has 4 link(s):
    (blocks NA-wcoast -1): pval = 0.00000 | qval = 0.00000 | val = 0.765
    (blocks NA-wcoast -2): pval = 0.00000 | qval = 0.00000 | val = -0.325
    (R NE-Pac -7): pval = 0.00000 | qval = 0.00000 | val = 0.086
    (R NE-Pac -6): pval = 0.00002 | qval = 0.00021 | val = 0.073

Variable blocks WR-GL has 14 link(s):
    (blocks WR-GL -1): pval = 0.00000 | qval = 0.00000 | val = 0.978
    (blocks WR-GL -2): pval = 0.00000 | qval = 0.00000 | val = -0.882
    (blocks WR-GL -3): pval = 0.00000 | qval = 0.00000 | val = 0.628
    (OLR_BayBengal -2): pval = 0.00000 | qval = 0.00000 | val = 0.180
    (blocks WR-GL -4): pval = 0.00000 | qval = 0.00000 | val = -0.175
    (blocks WR-GL -7): pval = 0.00000 | qval = 0.00000 | val = 0.151
    (blocks WR-GL -5): pval = 0.00000 | qval = 0.00000 | val = -0.141
    (OLR_BayBengal -1): pval = 0.00000 | qval = 0.00000 | val = -0.127
    (blocks WR-GL -6): pval = 0.00000 | qval = 0.00000 | val = 0.100
    (OLR_BayBengal -3): pval = 0.00000 | qval = 0.00000 | val = -0.090
    (blocks WR-GL -19): pval = 0.00000 | qval = 0.00000 | val = -0.087
    (blocks WR-GL -9): pval = 0.00000 | qval = 0.00000 | val = -0.086
    (blocks WR-GL -8): pval = 0.00008 | qval = 0.00094 | val = -0.066
    (OLR_BayBengal 0): pval = 0.00059 | qval = 0.00059 | val = 0.058

Variable OLR_BayBengal has 4 link(s):
    (OLR_BayBengal -1): pval = 0.00000 | qval = 0.00000 | val = 0.746
    (OLR_BayBengal -2): pval = 0.00000 | qval = 0.00000 | val = -0.185
    (blocks WR-GL 0): pval = 0.00059 | qval = 0.00059 | val = 0.058
    (OLR_BayBengal -3): pval = 0.00082 | qval = 0.00908 | val = 0.056

3-daily model

Significant links at alpha = 0.01:

Variable R NE-Pac has 4 link(s):
  (R NE-Pac -1): pval = 0.00000 | qval = 0.00000 | val = 0.792
  (R NE-Pac -2): pval = 0.00000 | qval = 0.00000 | val = -0.354
  (R NE-Pac -6): pval = 0.00001 | qval = 0.00006 | val = 0.130
  (R NE-Pac -3): pval = 0.00010 | qval = 0.00077 | val = 0.112
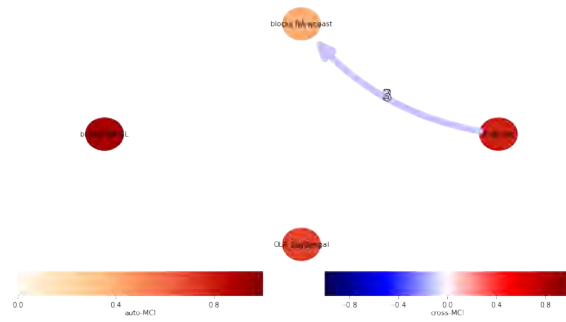
Variable blocks NA-wcoast has 2 link(s):
  (blocks NA-wcoast -1): pval = 0.00000 | qval = 0.00000 | val = 0.410
  (R NE-Pac -3): pval = 0.00031 | qval = 0.00213 | val = -0.105

Variable blocks WR-GL has 6 link(s):
  (blocks WR-GL -1): pval = 0.00000 | qval = 0.00000 | val = 0.913
  (blocks WR-GL -2): pval = 0.00000 | qval = 0.00000 | val = -0.775
  (blocks WR-GL -3): pval = 0.00000 | qval = 0.00000 | val = 0.668
  (blocks WR-GL -4): pval = 0.00000 | qval = 0.00000 | val = -0.566
  (blocks WR-GL -5): pval = 0.00000 | qval = 0.00000 | val = 0.495
  (blocks WR-GL -6): pval = 0.00000 | qval = 0.00000 | val = 0.324

Variable OLR_BayBengal has 2 link(s):
  (OLR_BayBengal -1): pval = 0.00000 | qval = 0.00000 | val = 0.702
  (OLR_BayBengal -2): pval = 0.00000 | qval = 0.00000 | val = -0.185

6-daily model

Significant links at alpha = 0.01:

Variable R NE-Pac has 4 link(s):
  (R NE-Pac -1): pval = 0.00000 | qval = 0.00000 | val = 0.712
  (R NE-Pac -2): pval = 0.00000 | qval = 0.00000 | val = -0.438
  (R NE-Pac -3): pval = 0.00000 | qval = 0.00000 | val = 0.289
  (blocks WR-GL -1): pval = 0.00022 | qval = 0.00104 | val = 0.151

Variable blocks NA-wcoast has 4 link(s):
  (blocks NA-wcoast -1): pval = 0.00000 | qval = 0.00000 | val = 0.278
  (R NE-Pac -1): pval = 0.00001 | qval = 0.00004 | val = 0.185
  (R NE-Pac -2): pval = 0.00001 | qval = 0.00005 | val = -0.181
  (OLR_BayBengal -2): pval = 0.00101 | qval = 0.00442 | val = -0.135

Variable blocks WR-GL has 3 link(s):
  (blocks WR-GL -1): pval = 0.00000 | qval = 0.00000 | val = 0.623
  (blocks WR-GL -2): pval = 0.00000 | qval = 0.00000 | val = -0.225
  (blocks WR-GL -3): pval = 0.00184 | qval = 0.00735 | val = 0.128

Variable OLR_BayBengal has 3 link(s):
  (OLR_BayBengal -1): pval = 0.00000 | qval = 0.00000 | val = 0.625
  (R NE-Pac -1): pval = 0.00201 | qval = 0.00742 | val = 0.127
  (OLR_BayBengal -2): pval = 0.00260 | qval = 0.00891 | val = -0.123
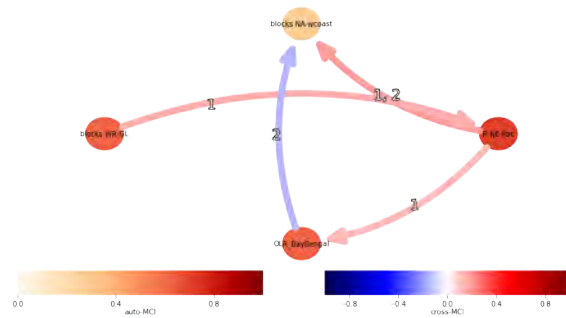
A3.5 – Composites of blocking frequency anomalies leading up to, during, and after high *R* days in the eastern North Pacific

Blocking frequency anomalies (shaded) wrt season and seasonal climatology (dashed line)
2 PVU line at 320K (green line). Areas where anomalies differ significantly at alpha 0.01 (FDR corrected) are marked with black solid lines
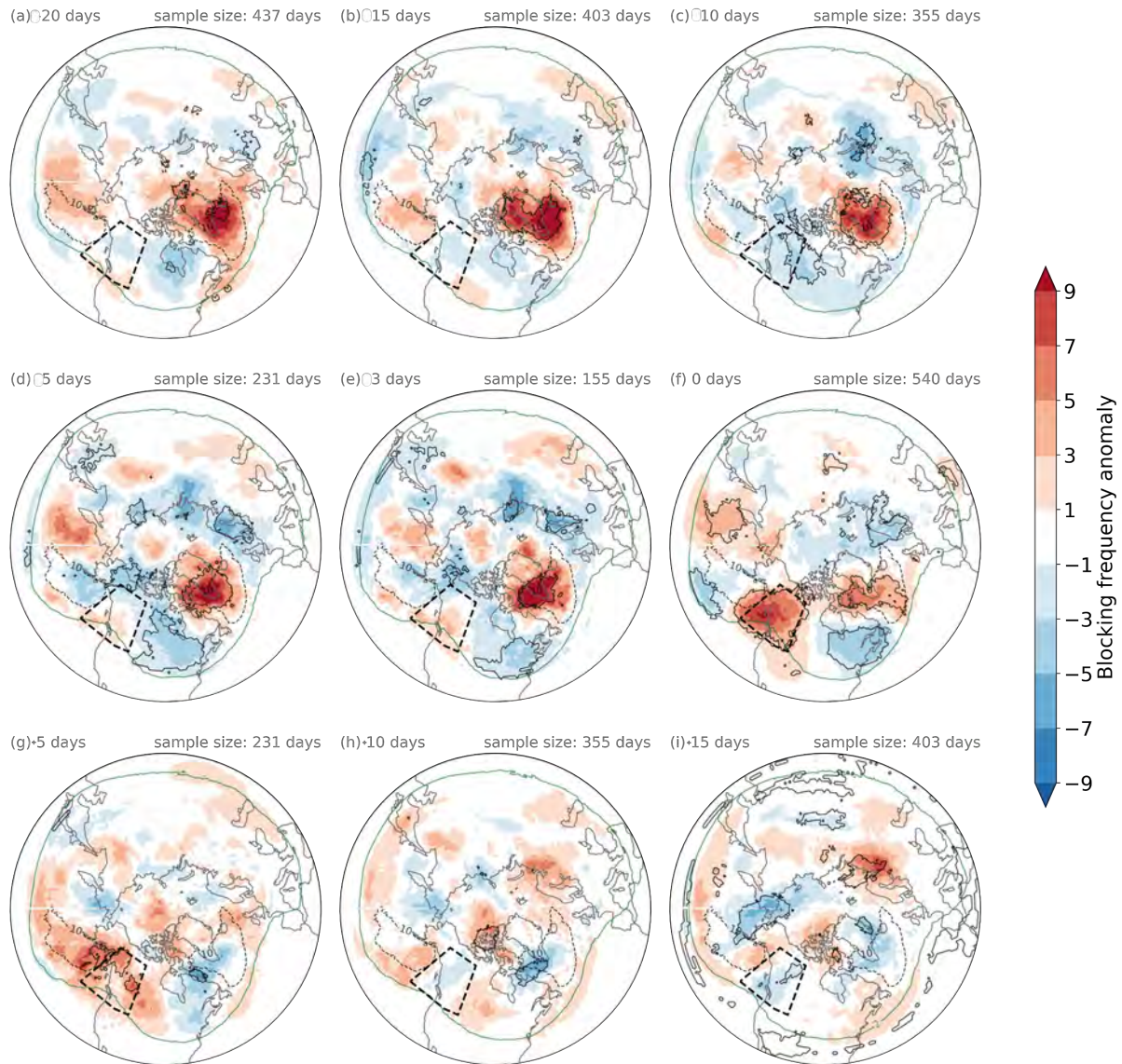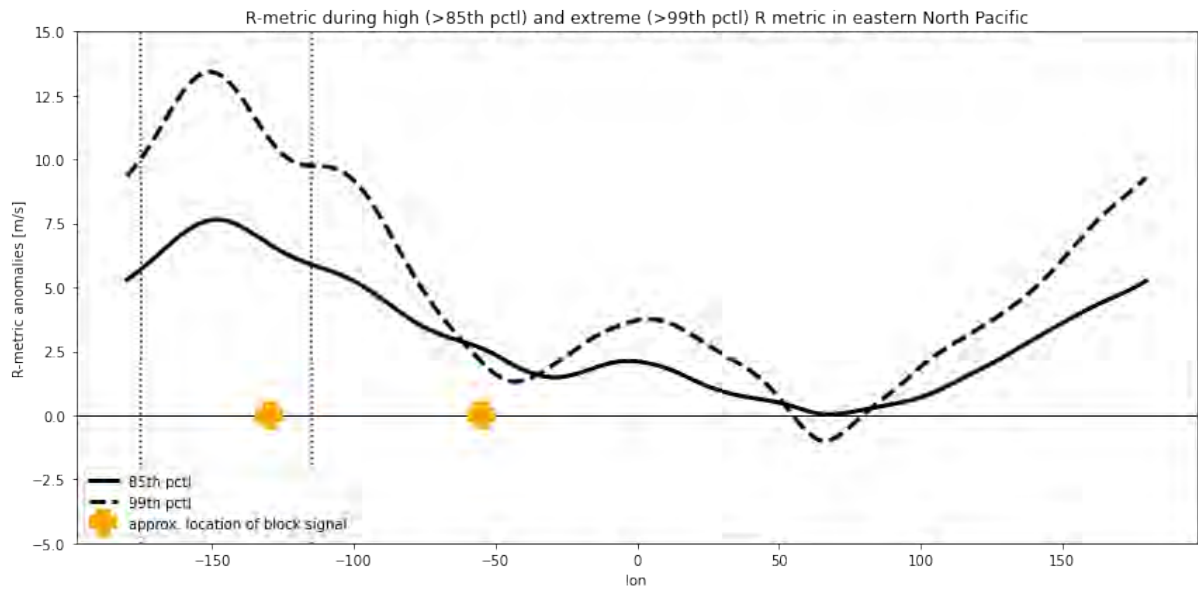*Composite of Lon -175 to -115 DJF_0.85to1.0_pctl_R_metric . Days with high R were removed from the lagged composite.*

Figure A3.6: As Figure 16, but for time lags a) 20, b) 15, c) 10, d) 5, e) 3 before high *R* days, f) during high *R* days, and g) 5, h) 10, i) 15 days after high *R* days.

A3.6 – *R* anomalies during high and extremely high *R* days in the eastern North Pacific

Fig. A3.7: As figure A3.1, but for high and extremely high *R* in the eastern North Pacific. The approximate locations of the two blocking features ($blocks_{NA-wcoast}$ at 120° W and $blocks_{WR-GL}$ at 60° W) are marked by orange crosses.

A3.7 – OLR and VP composite during high *R* days in the western North Pacific
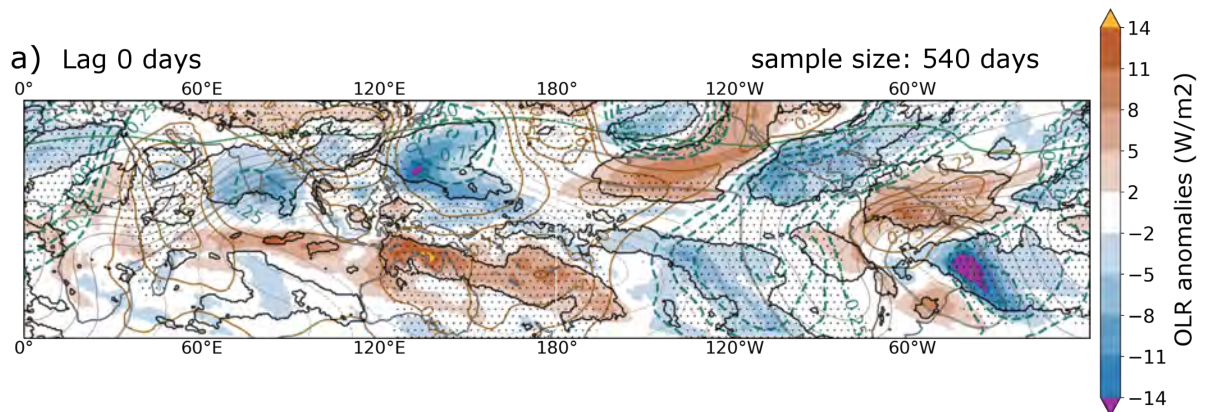
Fig. A3.8: As Figure 11 but OLR and VP anomalies during (lag 0) high *R* days in the western North Pacific (115° E to 175° E).

A3.8 – North Atlantic causal network using 1 monthly data
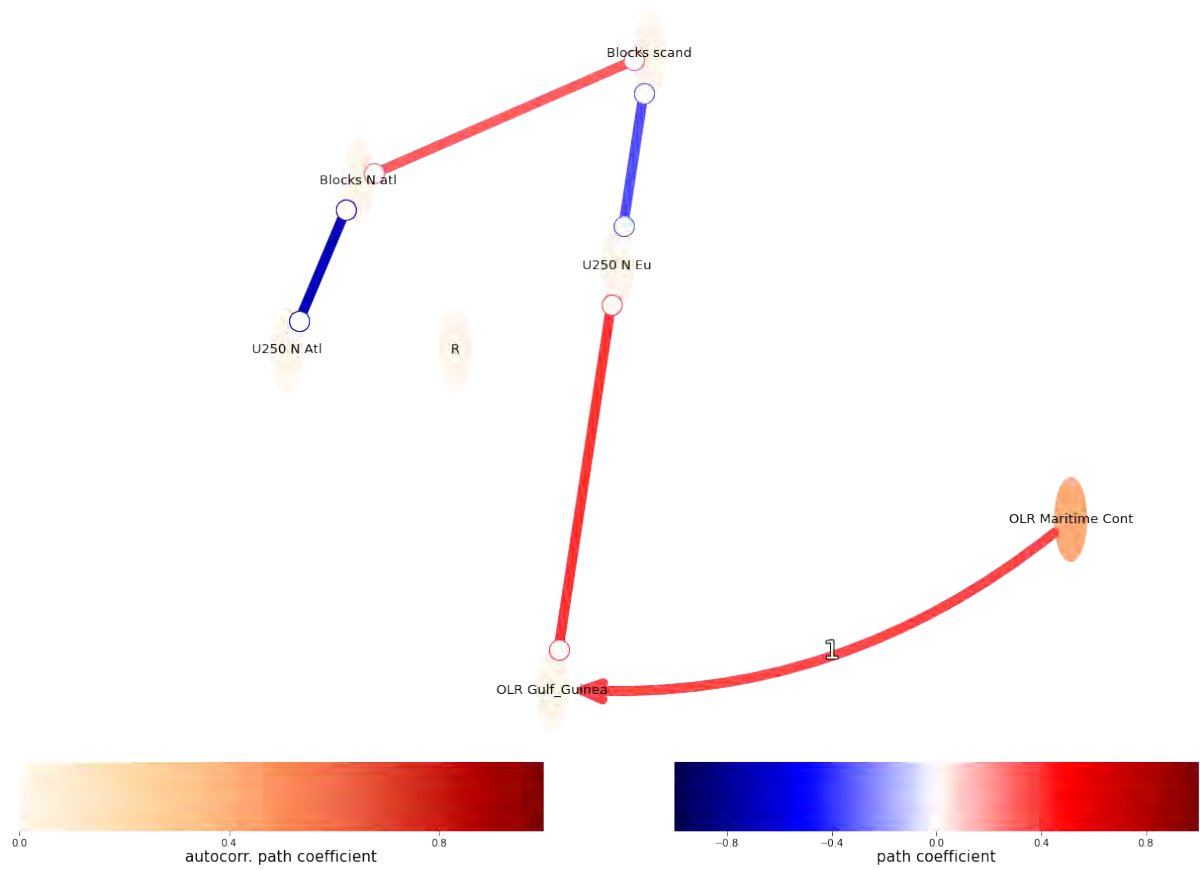
Figure A3.8: As figure 13, but using 30-day mean data with $\tau_{max} = 3$, $\alpha_{PC} = 0.01$, and $\alpha_{FDR} = 0.01$.

A4 p-values, q-values, and test statistics of PCMCI analyses

The table outputs of PCMCI for the "main" causal networks showed in this work (Figs. 13-15 for North Atlantic and Figs. 22-24 for eastern North Pacific). Notation is as in section A2.2.

A4.1 – North Atlantic causal network

Daily timescale

```
## Significant links at alpha = 0.01:

    Variable R has 9 link(s):
      (R -1): pval = 0.00000 | qval = 0.00000 | val =  0.871
      (R -2): pval = 0.00000 | qval = 0.00000 | val = -0.533
      (R -3): pval = 0.00000 | qval = 0.00000 | val =  0.302
      (R -4): pval = 0.00000 | qval = 0.00000 | val = -0.173
      (R -5): pval = 0.00000 | qval = 0.00000 | val =  0.100
      (U250 N Eu -7): pval = 0.00001 | qval = 0.00019 | val =  0.076
      (Blocks N atl -7): pval = 0.00001 | qval = 0.00032 | val =  0.074
      (Blocks Scand -7): pval = 0.00004 | qval = 0.00101 | val = -0.069
      (Blocks N atl -8): pval = 0.00009 | qval = 0.00227 | val = -0.066

    Variable Blocks N atl has 7 link(s):
      (Blocks N atl -1): pval = 0.00000 | qval = 0.00000 | val =  0.742
      (Blocks N atl -2): pval = 0.00000 | qval = 0.00000 | val = -0.336
      (U250 N Atl  0): pval = 0.00000 | qval = 0.00000 | val = -0.190
      (U250 N Atl -1): pval = 0.00000 | qval = 0.00000 | val = -0.165
      (U250 N Atl -2): pval = 0.00000 | qval = 0.00000 | val =  0.096
      (Blocks N atl -3): pval = 0.00000 | qval = 0.00000 | val =  0.092
      (R -8): pval = 0.00001 | qval = 0.00035 | val = -0.073

    Variable Blocks Scand has 8 link(s):
      (Blocks Scand -1): pval = 0.00000 | qval = 0.00000 | val =  0.799
      (Blocks Scand -2): pval = 0.00000 | qval = 0.00000 | val = -0.365
      (U250 N Eu -1): pval = 0.00000 | qval = 0.00000 | val = -0.126
      (U250 N Eu  0): pval = 0.00000 | qval = 0.00000 | val = -0.125
      (Blocks Scand -3): pval = 0.00000 | qval = 0.00000 | val =  0.099
      (U250 N Eu -2): pval = 0.00001 | qval = 0.00025 | val =  0.075
      (Blocks N atl -2): pval = 0.00022 | qval = 0.00580 | val =  0.062
      (Blocks N atl -3): pval = 0.00027 | qval = 0.00668 | val =  0.061

    Variable OLR Gulf Guinea has 5 link(s):
      (OLR Gulf Guinea -1): pval = 0.00000 | qval = 0.00000 | val =  0.716
      (OLR Gulf Guinea -2): pval = 0.00000 | qval = 0.00000 | val = -0.245
      (OLR Marit Cont  0): pval = 0.00000 | qval = 0.00000 | val = -0.095
      (OLR Gulf Guinea -3): pval = 0.00000 | qval = 0.00004 | val =  0.081
      (U250 N Eu -7): pval = 0.00039 | qval = 0.00921 | val =  0.060

    Variable OLR Marit Cont has 4 link(s):
      (OLR Marit Cont -1): pval = 0.00000 | qval = 0.00000 | val =  0.763
      (OLR Marit Cont -2): pval = 0.00000 | qval = 0.00000 | val = -0.169
      (U250 N Atl  0): pval = 0.00000 | qval = 0.00000 | val = -0.118
      (OLR Gulf Guinea  0): pval = 0.00000 | qval = 0.00000 | val = -0.095

    Variable U250 N Atl has 10 link(s):
      (U250 N Atl -1): pval = 0.00000 | qval = 0.00000 | val =  0.781
      (U250 N Atl -2): pval = 0.00000 | qval = 0.00000 | val = -0.321
      (Blocks N atl  0): pval = 0.00000 | qval = 0.00000 | val = -0.190
      (U250 N Atl -3): pval = 0.00000 | qval = 0.00000 | val =  0.160
      (U250 N Eu -1): pval = 0.00000 | qval = 0.00000 | val =  0.138
      (U250 N Eu -2): pval = 0.00000 | qval = 0.00000 | val = -0.131
      (OLR Marit Cont  0): pval = 0.00000 | qval = 0.00000 | val = -0.118
      (Blocks N atl -1): pval = 0.00000 | qval = 0.00008 | val = -0.079
      (U250 N Eu  0): pval = 0.00022 | qval = 0.00022 | val = -0.062
      (U250 N Atl -4): pval = 0.00033 | qval = 0.00810 | val = -0.060

    Variable U250 N Eu has 9 link(s):
      (U250 N Eu -1): pval = 0.00000 | qval = 0.00000 | val =  0.807
      (U250 N Eu -2): pval = 0.00000 | qval = 0.00000 | val = -0.383
      (U250 N Eu -3): pval = 0.00000 | qval = 0.00000 | val =  0.187
      (Blocks Scand  0): pval = 0.00000 | qval = 0.00000 | val = -0.125
      (R -7): pval = 0.00000 | qval = 0.00000 | val = -0.108
      (U250 N Eu -4): pval = 0.00000 | qval = 0.00000 | val = -0.101
      (Blocks N atl -1): pval = 0.00000 | qval = 0.00000 | val = -0.091
      (U250 N Atl  0): pval = 0.00022 | qval = 0.00022 | val = -0.062
      (Blocks N atl -2): pval = 0.00039 | qval = 0.00921 | val =  0.059
```

3-daily timescale

```
## Significant links at alpha = 0.01:

    Variable R has 5 link(s):
      (R -1): pval = 0.00000 | qval = 0.00000 | val =  0.779
      (R -2): pval = 0.00000 | qval = 0.00000 | val = -0.339
      (R -6): pval = 0.00010 | qval = 0.00141 | val =  0.113
      (Blocks N atl -2): pval = 0.00019 | qval = 0.00256 | val =  0.108
      (Blocks Scand -2): pval = 0.00047 | qval = 0.00575 | val = -0.101

    Variable Blocks N atl has 5 link(s):
      (Blocks N atl -1): pval = 0.00000 | qval = 0.00000 | val =  0.416
      (U250 N Atl  0): pval = 0.00000 | qval = 0.00000 | val = -0.371
      (U250 N Atl -1): pval = 0.00000 | qval = 0.00000 | val = -0.193
      (Blocks N atl -2): pval = 0.00000 | qval = 0.00001 | val = -0.143
      (R -1): pval = 0.00001 | qval = 0.00010 | val =  0.131

    Variable Blocks Scand has 6 link(s):
      (Blocks Scand -1): pval = 0.00000 | qval = 0.00000 | val =  0.589
      (U250 N Eu  0): pval = 0.00000 | qval = 0.00000 | val = -0.296
      (Blocks Scand -2): pval = 0.00000 | qval = 0.00000 | val = -0.215
      (U250 N Eu -1): pval = 0.00002 | qval = 0.00029 | val = -0.124
      (Blocks Scand -3): pval = 0.00014 | qval = 0.00193 | val =  0.110
      (Blocks N atl -1): pval = 0.00021 | qval = 0.00272 | val =  0.107
    Variable OLR Gulf Guinea has 4 link(s):
      (OLR Gulf Guinea -1): pval = 0.00000 | qval = 0.00000 | val =  0.466
      (U250 N Eu  0): pval = 0.00000 | qval = 0.00000 | val =  0.142
      (R -2): pval = 0.00004 | qval = 0.00058 | val = -0.120
      (U250 N Eu -1): pval = 0.00054 | qval = 0.00608 | val =  0.100

    Variable OLR Marit Cont has 3 link(s):
      (OLR Marit Cont -1): pval = 0.00000 | qval = 0.00000 | val =  0.735
      (OLR Marit Cont -2): pval = 0.00000 | qval = 0.00000 | val = -0.215
      (U250 N Atl  0): pval = 0.00132 | qval = 0.00132 | val = -0.093

    Variable U250 N Atl has 6 link(s):
      (U250 N Atl -1): pval = 0.00000 | qval = 0.00000 | val =  0.650
      (Blocks N atl  0): pval = 0.00000 | qval = 0.00000 | val = -0.371
      (U250 N Atl -2): pval = 0.00000 | qval = 0.00000 | val = -0.186
      (R -1): pval = 0.00005 | qval = 0.00083 | val = -0.117
      (R -3): pval = 0.00054 | qval = 0.00608 | val =  0.100
      (OLR Marit Cont  0): pval = 0.00132 | qval = 0.00132 | val = -0.093

    Variable U250 N Eu has 5 link(s):
      (U250 N Eu -1): pval = 0.00000 | qval = 0.00000 | val =  0.639
      (Blocks Scand  0): pval = 0.00000 | qval = 0.00000 | val = -0.296
      (U250 N Eu -2): pval = 0.00000 | qval = 0.00000 | val = -0.171
      (OLR Gulf Guinea  0): pval = 0.00000 | qval = 0.00000 | val =  0.142
      (R -2): pval = 0.00000 | qval = 0.00004 | val = -0.138
```

6-daily timescale

```
## Significant links at alpha = 0.01:

    Variable R has 6 link(s):
      (R -1): pval = 0.00000 | qval = 0.00000 | val =  0.643
      (R -2): pval = 0.00000 | qval = 0.00000 | val = -0.326
      (R -3): pval = 0.00000 | qval = 0.00002 | val =  0.198
      (Blocks N atl  0): pval = 0.00005 | qval = 0.00005 | val =  0.166
      (U250 N Eu -1): pval = 0.00063 | qval = 0.00552 | val =  0.140
      (U250 N Atl  0): pval = 0.00085 | qval = 0.00085 | val = -0.137

    Variable Blocks N atl has 4 link(s):
      (U250 N Atl  0): pval = 0.00000 | qval = 0.00000 | val = -0.495
      (Blocks N atl -1): pval = 0.00004 | qval = 0.00055 | val =  0.167
      (R  0): pval = 0.00005 | qval = 0.00005 | val =  0.166
      (U250 N Atl -1): pval = 0.00010 | qval = 0.00125 | val = -0.159

    Variable Blocks Scand has 3 link(s):
      (U250 N Eu  0): pval = 0.00000 | qval = 0.00000 | val = -0.347
      (Blocks Scand -1): pval = 0.00000 | qval = 0.00000 | val =  0.345
      (Blocks N atl -1): pval = 0.00038 | qval = 0.00370 | val =  0.145

    Variable OLR Gulf Guinea has 5 link(s):
      (OLR Gulf Guinea -1): pval = 0.00000 | qval = 0.00000 | val =  0.292
      (U250 N Eu  0): pval = 0.00000 | qval = 0.00000 | val =  0.214
      (OLR Marit Cont -3): pval = 0.00000 | qval = 0.00001 | val =  0.201
      (U250 N Eu -1): pval = 0.00016 | qval = 0.00184 | val =  0.154
      (R -1): pval = 0.00064 | qval = 0.00552 | val = -0.140

    Variable OLR Marit Cont has 3 link(s):
      (OLR Marit Cont -1): pval = 0.00000 | qval = 0.00000 | val =  0.647
      (OLR Marit Cont -2): pval = 0.00000 | qval = 0.00001 | val = -0.205
      (OLR Gulf Guinea -2): pval = 0.00072 | qval = 0.00558 | val =  0.139

    Variable U250 N Atl has 4 link(s):
      (Blocks N atl  0): pval = 0.00000 | qval = 0.00000 | val = -0.495
      (U250 N Atl -1): pval = 0.00000 | qval = 0.00000 | val =  0.487
      (R  0): pval = 0.00085 | qval = 0.00085 | val = -0.137
      (U250 N Eu  0): pval = 0.00914 | qval = 0.00914 | val =  0.107

    Variable U250 N Eu has 6 link(s):
      (U250 N Eu -1): pval = 0.00000 | qval = 0.00000 | val =  0.472
      (Blocks Scand  0): pval = 0.00000 | qval = 0.00000 | val = -0.347
      (OLR Gulf Guinea  0): pval = 0.00000 | qval = 0.00000 | val =  0.214
      (R -1): pval = 0.00026 | qval = 0.00278 | val = -0.149
      (U250 N Eu -2): pval = 0.00072 | qval = 0.00558 | val = -0.139
      (U250 N Atl  0): pval = 0.00914 | qval = 0.00914 | val =  0.107
```

A4.2 – Eastern North Pacific causal network

Daily timescale

```
## Significant links at alpha = 0.01:

Variable R NE-Pac has 11 link(s):
    (R NE-Pac -1): pval = 0.00000 | qval = 0.00000 | val =  0.887
    (R NE-Pac -2): pval = 0.00000 | qval = 0.00000 | val = -0.581
    (R NE-Pac -3): pval = 0.00000 | qval = 0.00000 | val =  0.351
    (R NE-Pac -4): pval = 0.00000 | qval = 0.00000 | val = -0.216
    (R NE-Pac -14): pval = 0.00000 | qval = 0.00000 | val = -0.135
    (R NE-Pac -5): pval = 0.00000 | qval = 0.00000 | val =  0.118
    (OLR E-Pac -6): pval = 0.00000 | qval = 0.00001 | val = -0.087
    (blocks WR-GL -7): pval = 0.00005 | qval = 0.00109 | val =  0.068
    (R NE-Pac -6): pval = 0.00005 | qval = 0.00109 | val = -0.068
    (R NE-Pac -7): pval = 0.00005 | qval = 0.00113 | val = -0.068
    (U250 NE-Pac -7): pval = 0.00011 | qval = 0.00226 | val =  0.065

Variable blocks NA-wcoast has 7 link(s):
    (blocks NA-wcoast -1): pval = 0.00000 | qval = 0.00000 | val =  0.764
    (blocks NA-wcoast -2): pval = 0.00000 | qval = 0.00000 | val = -0.324
    (U250 NE-Pac 0): pval = 0.00000 | qval = 0.00000 | val = -0.189
    (U250 NE-Pac -1): pval = 0.00000 | qval = 0.00000 | val = -0.094
    (R NE-Pac -7): pval = 0.00000 | qval = 0.00001 | val =  0.085
    (R NE-Pac -6): pval = 0.00003 | qval = 0.00073 | val =  0.070
    (OLR Philip-Sea -3): pval = 0.00023 | qval = 0.00457 | val = -0.062

Variable blocks WR-GL has 13 link(s):
    (blocks WR-GL -1): pval = 0.00000 | qval = 0.00000 | val =  0.978
    (blocks WR-GL -2): pval = 0.00000 | qval = 0.00000 | val = -0.882
    (blocks WR-GL -3): pval = 0.00000 | qval = 0.00000 | val =  0.628
    (blocks WR-GL -4): pval = 0.00000 | qval = 0.00000 | val = -0.175
    (blocks WR-GL -7): pval = 0.00000 | qval = 0.00000 | val =  0.151
    (blocks WR-GL -5): pval = 0.00000 | qval = 0.00000 | val = -0.141
    (blocks WR-GL -6): pval = 0.00000 | qval = 0.00000 | val =  0.100
    (blocks WR-GL -19): pval = 0.00000 | qval = 0.00001 | val = -0.087
    (blocks WR-GL -9): pval = 0.00000 | qval = 0.00001 | val = -0.086
    (OLR NE-Pac -2): pval = 0.00001 | qval = 0.00028 | val = -0.074

    (OLR NE-Pac -1): pval = 0.00002 | qval = 0.00055 | val =  0.071
    (blocks WR-GL -8): pval = 0.00008 | qval = 0.00179 | val = -0.066
    (OLR NE-Pac -3): pval = 0.00013 | qval = 0.00264 | val =  0.064

Variable U250 NE-Pac has 8 link(s):
    (U250 NE-Pac -1): pval = 0.00000 | qval = 0.00000 | val =  0.784
    (U250 NE-Pac -2): pval = 0.00000 | qval = 0.00000 | val = -0.347
    (blocks NA-wcoast 0): pval = 0.00000 | qval = 0.00000 | val = -0.189
    (U250 NE-Pac -3): pval = 0.00000 | qval = 0.00000 | val =  0.156
    (OLR NE-Pac -2): pval = 0.00000 | qval = 0.00000 | val =  0.098
    (R NE-Pac -4): pval = 0.00002 | qval = 0.00054 | val = -0.071
    (U250 NE-Pac -4): pval = 0.00004 | qval = 0.00099 | val = -0.069
    (R NE-Pac -6): pval = 0.00047 | qval = 0.00895 | val = -0.059

Variable OLR Philip-Sea has 4 link(s):
    (OLR Philip-Sea -1): pval = 0.00000 | qval = 0.00000 | val =  0.700
    (OLR Philip-Sea -2): pval = 0.00000 | qval = 0.00000 | val = -0.303
    (OLR Philip-Sea -3): pval = 0.00000 | qval = 0.00000 | val =  0.143
    (OLR Philip-Sea -4): pval = 0.00034 | qval = 0.00655 | val = -0.060

Variable OLR NE-Pac has 7 link(s):
    (OLR NE-Pac -1): pval = 0.00000 | qval = 0.00000 | val =  0.681
    (OLR NE-Pac -2): pval = 0.00000 | qval = 0.00000 | val = -0.239
    (OLR NE-Pac -3): pval = 0.00000 | qval = 0.00000 | val =  0.095
    (U250 NE-Pac -1): pval = 0.00000 | qval = 0.00002 | val =  0.084
    (OLR NE-Pac -4): pval = 0.00001 | qval = 0.00040 | val =  0.073
    (OLR Philip-Sea -3): pval = 0.00002 | qval = 0.00044 | val =  0.072
    (OLR E-Pac 0): pval = 0.00041 | qval = 0.00041 | val = -0.059

Variable OLR E-Pac has 6 link(s):
    (OLR E-Pac -1): pval = 0.00000 | qval = 0.00000 | val =  0.737
    (OLR E-Pac -2): pval = 0.00000 | qval = 0.00000 | val = -0.360
    (OLR E-Pac -3): pval = 0.00000 | qval = 0.00000 | val =  0.168
    (OLR NE-Pac -3): pval = 0.00018 | qval = 0.00374 | val =  0.063
    (OLR Philip-Sea -5): pval = 0.00033 | qval = 0.00638 | val = -0.060
    (OLR NE-Pac 0): pval = 0.00041 | qval = 0.00041 | val = -0.059
```

3-daily timescale

```
## Significant links at alpha = 0.01:

Variable R NE-Pac has 5 link(s):
    (R NE-Pac -1): pval = 0.00000 | qval = 0.00000 | val =  0.792
    (R NE-Pac -2): pval = 0.00000 | qval = 0.00000 | val = -0.354
    (R NE-Pac -6): pval = 0.00001 | qval = 0.00014 | val =  0.130
    (R NE-Pac -3): pval = 0.00010 | qval = 0.00154 | val =  0.112
    (U250 NE-Pac -3): pval = 0.00078 | qval = 0.00956 | val =  0.097

Variable blocks NA-wcoast has 4 link(s):
    (blocks NA-wcoast -1): pval = 0.00000 | qval = 0.00000 | val =  0.399
    (U250 NE-Pac 0): pval = 0.00000 | qval = 0.00000 | val = -0.290
    (OLR Philip-Sea -1): pval = 0.00004 | qval = 0.00059 | val = -0.119
    (R NE-Pac -3): pval = 0.00067 | qval = 0.00856 | val = -0.099

Variable blocks WR-GL has 7 link(s):
    (blocks WR-GL -1): pval = 0.00000 | qval = 0.00000 | val =  0.913
    (blocks WR-GL -2): pval = 0.00000 | qval = 0.00000 | val = -0.775
    (blocks WR-GL -3): pval = 0.00000 | qval = 0.00000 | val =  0.668
    (blocks WR-GL -4): pval = 0.00000 | qval = 0.00000 | val = -0.566
    (blocks WR-GL -5): pval = 0.00000 | qval = 0.00000 | val =  0.495
    (blocks WR-GL -6): pval = 0.00000 | qval = 0.00000 | val =  0.324
    (U250 NE-Pac 0): pval = 0.00116 | qval = 0.00116 | val =  0.094

Variable U250 NE-Pac has 6 link(s):
    (U250 NE-Pac -1): pval = 0.00000 | qval = 0.00000 | val =  0.600
    (blocks NA-wcoast 0): pval = 0.00000 | qval = 0.00000 | val = -0.290
    (U250 NE-Pac -2): pval = 0.00000 | qval = 0.00000 | val = -0.172
    (OLR NE-Pac 0): pval = 0.00000 | qval = 0.00000 | val =  0.137
    (R NE-Pac -1): pval = 0.00001 | qval = 0.00014 | val = -0.129
    (blocks WR-GL 0): pval = 0.00116 | qval = 0.00116 | val =  0.094

Variable OLR Philip-Sea has 3 link(s):
    (OLR Philip-Sea -1): pval = 0.00000 | qval = 0.00000 | val =  0.366
    (R NE-Pac -1): pval = 0.00000 | qval = 0.00006 | val = -0.135
    (blocks WR-GL -3): pval = 0.00002 | qval = 0.00028 | val = -0.124

Variable OLR NE-Pac has 3 link(s):
    (OLR NE-Pac -1): pval = 0.00000 | qval = 0.00000 | val =  0.400
    (U250 NE-Pac 0): pval = 0.00000 | qval = 0.00000 | val =  0.137
    (OLR E-Pac 0): pval = 0.00001 | qval = 0.00001 | val = -0.129

Variable OLR E-Pac has 4 link(s):
    (OLR E-Pac -1): pval = 0.00000 | qval = 0.00000 | val =  0.407
    (OLR NE-Pac 0): pval = 0.00001 | qval = 0.00001 | val = -0.129
    (U250 NE-Pac -2): pval = 0.00011 | qval = 0.00159 | val = -0.112
    (OLR NE-Pac -1): pval = 0.00021 | qval = 0.00282 | val =  0.107
```

6-daily timescale

```
## Significant links at alpha = 0.01:

Variable R NE-Pac has 8 link(s):
    (R NE-Pac -1): pval = 0.00000 | qval = 0.00000 | val =  0.712
    (R NE-Pac -2): pval = 0.00000 | qval = 0.00000 | val = -0.438
    (R NE-Pac -3): pval = 0.00000 | qval = 0.00000 | val =  0.289
    (OLR Philip-Sea 0): pval = 0.00002 | qval = 0.00002 | val = -0.173
    (U250 NE-Pac 0): pval = 0.00007 | qval = 0.00007 | val = -0.162
    (blocks WR-GL -1): pval = 0.00022 | qval = 0.00198 | val =  0.151
    (OLR NE-Pac 0): pval = 0.00034 | qval = 0.00034 | val = -0.147
    (OLR NE-Pac -3): pval = 0.00095 | qval = 0.00819 | val = -0.136

Variable blocks NA-wcoast has 4 link(s):
    (U250 NE-Pac 0): pval = 0.00000 | qval = 0.00000 | val = -0.308
    (blocks NA-wcoast -1): pval = 0.00000 | qval = 0.00000 | val =  0.303
    (R NE-Pac -1): pval = 0.00000 | qval = 0.00002 | val =  0.196
    (OLR E-Pac 0): pval = 0.00441 | qval = 0.00441 | val = -0.117

Variable blocks WR-GL has 2 link(s):
    (blocks WR-GL -1): pval = 0.00000 | qval = 0.00000 | val =  0.623
    (blocks WR-GL -2): pval = 0.00000 | qval = 0.00000 | val = -0.225

Variable U250 NE-Pac has 7 link(s):
    (U250 NE-Pac -1): pval = 0.00000 | qval = 0.00000 | val =  0.349

    (blocks NA-wcoast 0): pval = 0.00000 | qval = 0.00000 | val = -0.308
    (OLR NE-Pac 0): pval = 0.00000 | qval = 0.00000 | val =  0.240
    (R NE-Pac -1): pval = 0.00000 | qval = 0.00000 | val = -0.211
    (R NE-Pac -2): pval = 0.00005 | qval = 0.00053 | val =  0.165
    (R NE-Pac 0): pval = 0.00007 | qval = 0.00007 | val = -0.162
    (OLR E-Pac 0): pval = 0.00105 | qval = 0.00105 | val = -0.134

Variable OLR Philip-Sea has 3 link(s):
    (OLR Philip-Sea -1): pval = 0.00000 | qval = 0.00002 | val =  0.193
    (blocks WR-GL -1): pval = 0.00000 | qval = 0.00009 | val = -0.181
    (R NE-Pac 0): pval = 0.00002 | qval = 0.00002 | val = -0.173

Variable OLR NE-Pac has 4 link(s):
    (OLR NE-Pac -1): pval = 0.00000 | qval = 0.00000 | val =  0.341
    (U250 NE-Pac 0): pval = 0.00000 | qval = 0.00000 | val =  0.240
    (R NE-Pac 0): pval = 0.00034 | qval = 0.00034 | val = -0.147
    (OLR E-Pac 0): pval = 0.00127 | qval = 0.00127 | val = -0.132

Variable OLR E-Pac has 5 link(s):
    (OLR E-Pac -1): pval = 0.00000 | qval = 0.00000 | val =  0.322
    (U250 NE-Pac -1): pval = 0.00000 | qval = 0.00002 | val = -0.194
    (U250 NE-Pac 0): pval = 0.00105 | qval = 0.00105 | val = -0.134
    (OLR NE-Pac 0): pval = 0.00127 | qval = 0.00127 | val = -0.132
    (blocks NA-wcoast 0): pval = 0.00441 | qval = 0.00441 | val = -0.117
```

List of figures

List of tables

References

Ali, S.M., Martius, O., and Röthlisberger, M. (2021) Recurrent Rossby Wave Packets Modulate the Persistence of Dry and Wet Spells Across the Globe. *Geophysical Research Letters* **48**: e2020GL091452. doi: 10.1029/2020GL091452.

Ali. M. and Röthlisberger, M. (2021). avatar101/*R*: (Version v1.1). Zenodo. https://doi.org/10.5281/zenodo.5742810. (Accessed 02.12.2021).

Altenhoff, A.M., Martius, O., Croci-Maspoli, M., Schwierz, C., and Davies, H.C. (2008) Linkage of atmospheric blocks and synoptic-scale Rossby waves: a climatological analysis. *Tellus A: Dynamic Meteorology and Oceanography* **60**: 1053-1063. doi: 10.1111/j.1600-0870.2008.00354.x.

Barton, Y., Giannakaki, P., von Waldow, H., Chevalier, C., Pfahl, S., and Martius, O. (2016) Clustering of Regional-Scale Extreme Precipitation Events in Southern Switzerland. *Monthly Weather Review* **144**: 347–369. doi: 10.1175/MWR-D-15-0205.1.

Benjamini, Y. and Hochberg, Y. (1995) Controlling the false discovery rate: A practical and powerful approach to multiple testing. *Journal of the Royal Statistical Society Series B*. **57**: 289–300. doi: 10.1111/j.2517-6161.1995.tb02031.x.

Blackburn, M., Methven, J., and Roberts, N. (2008) Large-scale context for the UK floods in summer 2007. *Weather* **63**: 280-288. doi: 10.1002/wea.322.

Buehler, T., Raible, C.C., and Stocker, T.F. (2011) The relationship of winter season North Atlantic blocking frequencies to extreme cold or dry spells in the ERA-40. *Tellus A: Dynamic Meteorology and Oceanography* **63**: 212–222. doi: 10.1111/j.1600-0870.2010.00492.x.

Cassou, C. (2008) Intraseasonal interaction between the Madden–Julian Oscillation and the North Atlantic Oscillation. *Nature* **455**: 523–527. doi: 10.1038/nature07286.

Davies, H.C. (2015) Weather chains during the 2013/2014 winter and their significance for seasonal prediction. *Nature Geoscience* **8**: 833–837. doi: 10.1038/ngeo2561.

Deng, Y. and Ebert-Uphoff, I. (2014) Weakening of atmospheric information flow in a warming climate in the Community Climate System Model. *Geophysical Research Letters* **41**: 193–200. doi: 10.1002/2013GL058646.

Di Capua, G., Kretschmer, M., Donner, R. V., van den Hurk, B., Vellore, R., Krishnan, R., and Coumou, D. (2020a) Tropical and mid-latitude teleconnections interacting with the Indian summer monsoon rainfall: a theory-guided causal effect network approach. *Earth System Dynamics* **11**: 17–34. doi: 10.5194/esd-11-17-2020.

Di Capua, G., Runge, J., Donner, R. V., van den Hurk, B., Turner, A. G., Vellore, R., Krishnan, R., and Coumou, D. (2020b) Dominant patterns of interaction between the tropics and mid-latitudes in boreal summer: causal relationships and the role of timescales. *Weather and Climate Dynamics* **1**: 519–539, doi: 10.5194/wcd-1-519-2020.

Draper, N.R. and Smith, H. (1998) Applied Regression Analysis. 3rd ed. Wiley, New Jersey. doi: 10.1002/9781118625590.

Ebert-Uphoff, I. and Deng, Y. (2012) Causal Discovery for Climate Research Using Graphical Models. *Journal of Climate* **25**: 5648–5665. doi: 10.1175/JCLI-D-11-00387.1.

Feldstein, S.B. (2003) The dynamics of NAO teleconnection pattern growth and decay. *Quarterly Journal of the Royal Meteorological Society* **129**: 901–924. doi: 10.1256/qj.02.76.

Fragkoulidis, G., Wirth, V., Bossmann, P., and Fink, A.H. (2018) Linking Northern Hemisphere temperature extremes to Rossby wave packets. *Quarterly Journal of the Royal Meteorological Society* **144**: 553–566. doi: 10.1002/qj.3228.

Francis, J.A. and Vavrus, S.J. (2012) Evidence linking Arctic amplification to extreme weather in mid-latitudes: Arctic links to mid-latitude weather. *Geophysical Research Letters* **39**: L06801. doi: 10.1029/2012GL051000.

Francis, J.A. and Vavrus, S.J. (2015) Evidence for a wavier jet stream in response to rapid Arctic warming. *Environmental Research Letters* **10**: 014005. doi: 10.1088/1748-9326/10/1/014005.

Gerhardus, A. and Runge, J. (2021) High-recall causal discovery for autocorrelated time series with latent confounders. ArXiv:2007.01884.

Glatt, I. and Wirth, V. (2014) Identifying Rossby wave trains and quantifying their properties: Identifying and Quantifying Rossby Wave Trains. *Quarterly Journal of the Royal Meteorological Society* **140**: 384–396. doi: 10.1002/qj.2139.

Gosling, S.N., Lowe, J.A., McGregor, G.R., Pelling, M., and Malamud, B.D. (2009) Associations between elevated atmospheric temperature and human mortality: a critical review of the literature. *Climatic Change* **92**: 299–341. doi: 10.1007/s10584-008-9441-x.

Grams, C.M., Beerli, R., Pfenninger, S., Staffell, I., and Wernli, H. (2017) Balancing Europe's wind-power output through spatial deployment informed by weather regimes. *Nature Climate Change* **7**: 557–562. doi: 10.1038/nclimate3338.

Hajat, S., O'Connor, M., and Kosatsky, T. (2010) Health effects of hot weather: from awareness of risk factors to effective health protection. *The Lancet* **375**: 856–863. doi: 10.1016/S0140-6736(09)61711-6.

Hersbach, H., Bell, B., Berrisford, P., Biavati, G., Horányi, A., Muñoz Sabater, J., Nicolas, J., Peubey, C., Radu, R., Rozum, I., Schepers, D., Simmons, A., Soci, C., Dee, D., and Thépaut, J-N. (2018) ERA5 hourly data on single levels from 1979 to present. *Copernicus Climate Change Service (C3S) Climate Data Store (CDS)*. (Accessed on 25-11-2021). doi: 10.24381/cds.adbb2d47.

Hersbach, H., Bell, B., Berrisford, P., Hirahara, S., Horányi, A., Muñoz-Sabater, J., Nicolas, J., Peubey, C., Radu, R., Schepers, D., Simmons, A., Soci, C., Abdalla, S., Abellan, X., Balsamo, G., Bechtold, P., Biavati, G., Bidlot, J., Bonavita, M., Chiara, G., Dahlgren, P., Dee, D., Diamantakis, M., Dragani, R., Flemming, J., Forbes, R., Fuentes, M., Geer, A., Haimberger, L., Healy, S., Hogan, R. J., Hólm, E., Janisková, M., Keeley, S., Laloyaux, P., Lopez, P., Lupu, C., Radnoti, G., Rosnay, P., Rozum, I., Vamborg, F., Villaume, S., and Thépaut, J. (2020) The ERA5 global reanalysis. *Quarterly Journal of the Royal Meteorological Society* **146**: 1999–2049. doi: 10.1002/qj.3803.

Hirt, M., Craig, G.C., Schäfer, S.A.K., Savre, J., and Heinze, R. (2020) Cold-pool-driven convective initiation: using causal graph analysis to determine what convection-permitting models are missing. *Quarterly Journal of the Royal Meteorological Society* **146**: 2205–2227. doi: 10.1002/qj.3788.

Horton, D.E., Johnson, N.C., Singh, D., Swain, D.L., Rajaratnam, B., and Diffenbaugh, N.S. (2015) Contribution of changes in atmospheric circulation patterns to extreme temperature trends. *Nature* **522**: 465–469. doi: 10.1038/nature14550.

Hoskins, B.J., McIntyre, M.E., and Robertson, A.W. (1985) On the use and significance of isentropic potential vorticity maps. *Quarterly Journal of the Royal Meteorological Society* **111**: 877–946. doi: 10.1002/qj.49711147002.

Hoskins, B.J. and Sardeshmukh, P.D. (1987) A Diagnostic Study of the Dynamics of the Northern Hemisphere Winter of 1985-86. *Quarterly Journal of the Royal Meteorological Society* **113**: 759–778. doi: 10.1002/qj.49711347705.

Huang, C.S.Y. and Nakamura, N. (2017) Local wave activity budgets of the wintertime Northern Hemisphere: Implication for the Pacific and Atlantic storm tracks. *Geophysical Research Letters* **44**: 5673–5682. doi: 10.1002/2017GL073760.

Huynen, M.M., Martens, P., Schram, D., Weijenberg, M.P., and Kunst, A.E. (2001) The impact of heat waves and cold spells on mortality rates in the Dutch population. *Environmental Health Perspectives* **109**: 463–470. doi: 10.1289/ehp.01109463.

Jin, F. and Hoskins, B.J. (1995) The Direct Response to Tropical Heating in a Baroclinic Atmosphere. *Journal of the Atmospheric Sciences* **52**: 307–319. doi: 10.1175/1520-0469(1995)052<0307:TDRTTH>2.0.CO;2.

Kiladis, G.N. (1998) Observations of Rossby Waves Linked to Convection over the Eastern Tropical Pacific. *Journal of the Atmospheric Sciences* **55**: 321-339. doi: 10.1175/1520-0469(1998)055<0321:OORWLT>2.0.CO;2.

Kiladis, G. N., Dias, J., Straub, K. H., Wheeler, M. C., Tulich, S. N., Kikuchi, K., Weickmann, K. M., and Ventrice, M. J. (2014) A Comparison of OLR and Circulation-Based Indices for Tracking the MJO. *Monthly Weather Review* **142**: 1697–1715. doi: 10.1175/MWR-D-13-00301.1.

Knight, J. R., Maidens, A., Watson, P. A. G., Andrews, M., Belcher, S., Brunet, G., Fereday, D., Folland, C. K., Scaife, A. A., and Slingo, J. (2017) Global meteorological influences on the record UK rainfall of winter 2013–14. *Environmental Research Letters* **12**: 074001. Doi: 10.1088/1748-9326/aa693c.

Knippertz, P. (2007) Tropical–extratropical interactions related to upper-level troughs at low latitudes. Dynamics of Atmospheres and Oceans. *Monthly Weather Review* **43**: 36–62. doi: 10.1175/MWR2999.1.

Kretschmer, M., Coumou, D., Donges, J.F., and Runge, J. (2016) Using Causal Effect Networks to Analyze Different Arctic Drivers of Midlatitude Winter Circulation. *Journal of Climate* **29**: 4069–4081. doi: 10.1175/JCLI-D-15-0654.1.

Lenggenhager, S., Croci-Maspoli, M., Brönnimann, S., and Martius, O. (2019) On the dynamical coupling between atmospheric blocks and heavy precipitation events: A discussion of the southern Alpine flood in October 2000. *Quarterly Journal of the Royal Meteorological Society* **145**: 530–545. doi: 10.1002/qj.3449.

Li, R.K.K., Woollings, T., O'Reilly, C., and Scaife, A.A. (2020) Effect of the North Pacific Tropospheric Waveguide on the Fidelity of Model El Niño Teleconnections. *Journal of Climate* **33**: 5223–5237. doi: 10.1175/JCLI-D-19-0156.1.

Ma, Q. and Franzke, C.L.E. (2021) The role of transient eddies and diabatic heating in the maintenance of European heat waves: a nonlinear quasi-stationary wave perspective. *Climate Dynamics* **56:** 2983–3002. doi: 10.1007/s00382-021-05628-9.

Madden, R.A. and Julian, P.R. (1994) Observations of the 40–50-Day Tropical Oscillation—A Review. *Monthly Weather Review* **122**: 814–837. doi: 10.1175/1520-0493(1994)122<0814:OOTDTO>2.0.CO;2.

Manola, I., Haarsma, R. J., and Hazeleger, W. (2013) Drivers of North Atlantic Oscillation Events. *Tellus A: Dynamic Meteorology and Oceanography* **65**: 19741. doi: 10.3402/tellusa.v65i0.19741.

Martius, O., Schwierz, C., and Davies, H.C. (2010) Tropopause-Level Waveguides. *Journal of the Atmospheric Sciences* **67**: 866–879. doi: 10.1175/2009JAS2995.1.

MeteoSchweiz (2006) Starkniederschlagsereignis August 2005. Arbeitsberichte der MeteoSchweiz 211: 63 pp.

Michel, C. and Rivière, G. (2011) The Link between Rossby Wave Breakings and Weather Regime Transitions. *Journal of the Atmospheric Sciences* **68**: 1730–1748. doi: 10.1175/2011JAS3635.1.

Moore, R.W., Martius, O., and Spengler, T. (2010) The Modulation of the Subtropical and Extratropical Atmosphere in the Pacific Basin in Response to the Madden–Julian Oscillation. *Monthly Weather Review* **138**: 2761–2779. doi: 10.1175/2010MWR3194.1.

Nakamura, N. and Huang, C.S.Y. (2017) Local Wave Activity and the Onset of Blocking along a Potential Vorticity Front. *Journal of the Atmospheric Sciences* **74**: 2341–2362. doi: 10.1175/JAS-D-17-0029.1.

NOAA Center for Weather and Climate Prediction (CPC) (2005a) Daily Madden-Julian Oscillation Indices. (Accessed 26.11.2021). https://www.cpc.ncep.noaa.gov/products/precip/CWlink/daily_mjo_index/mjo_index.shtml

NOAA Center for Weather and Climate Prediction (CPC) (2005b) MJO-Index AND MJO-Related Influences. (Accessed 26.11.2021). https://www.cpc.ncep.noaa.gov/products/precip/CWlink/daily_mjo_index/details.shtml

Pfahl, S. and Wernli, H. (2012) Quantifying the relevance of atmospheric blocking for co-located temperature extremes in the Northern Hemisphere on (sub-)daily time scales. *Geophysical Research Letters* **39**: L12807. doi: 10.1029/2012GL052261.

Pfleiderer, P. and Coumou, D. (2018) Quantification of temperature persistence over the Northern Hemisphere land-area. *Climate Dynamics* **51**: 627–637. doi: 10.1007/s00382-017-3945-x.

Quandt, L.-A., Keller, J.H., Martius, O., and Jones, S.C. (2017) Forecast Variability of the Blocking System over Russia in Summer 2010 and Its Impact on Surface Conditions. *Weather and Forecasting* **32:** 61–82. doi: 10.1175/WAF-D-16-0065.1.

Rohrer, M., Brönnimann, S., Martius, O., Raible, C.C., Wild, M., and Compo, G.P. (2018) Representation of Extratropical Cyclones, Blocking Anticyclones, and Alpine Circulation Types in Multiple Reanalyses and Model Simulations. *Journal of Climate* **31:** 3009–3031. doi: 10.1175/JCLI-D-17-0350.1.

Rossby, C.-G. (1945) On the Propagation of Frequencies and Energy in Certain Types of Oceanic and Atmospheric Waves. *Journal of Meteorology* **2:** 187–204. doi: 10.1175/1520-0469(1945)002<0187:OTPOFA>2.0.CO;2.

Röthlisberger, M., Pfahl, S., and Martius, O. (2016) Regional-scale jet waviness modulates the occurrence of midlatitude weather extremes. *Geophysical Research Letters* **43**: 10,989– 10,997. doi:10.1002/2016GL070944.

Röthlisberger, M., Martius, O., and Wernli, H. (2018) Northern Hemisphere Rossby Wave Initiation Events on the Extratropical Jet—A Climatological Analysis. *Journal of Climate* **31**: 743–760. doi: 10.1175/JCLI-D-17-0346.1.

Röthlisberger, M. and Martius, O. (2019) Quantifying the Local Effect of Northern Hemisphere Atmospheric Blocks on the Persistence of Summer Hot and Dry Spells. *Geophysical Research Letters* **46**: 10101–10111. doi: 10.1029/2019GL083745.

Röthlisberger, M., Frossard, L., Bosart, L.F., Keyser, D., and Martius, O. (2019) Recurrent Synoptic-Scale Rossby Wave Patterns and Their Effect on the Persistence of Cold and Hot Spells. *Journal of Climate* **32**: 3207–3226. doi: 10.1175/JCLI-D-18-0664.1.

Runge, J., Petoukhov, V., and Kurths, J. (2014) Quantifying the Strength and Delay of Climatic Interactions: The Ambiguities of Cross Correlation and a Novel Measure Based on Graphical Models. *Journal of Climate* **27**: 720–739. doi: 10.1175/JCLI-D-13-00159.1.

Runge, J., Petoukhov, V., Donges, J. F., Hlinka, J., Jajcay, N., Vejmelka, M., Hartman, D., Marwan, N., Paluš, M., and Kurths, J. (2015) Identifying Causal Gateways and Mediators in Complex Spatio-Temporal Systems. *Nature Communications* **6**: 8502. doi: 10.1038/ncomms9502.

Runge, J. (2018) Causal network reconstruction from time series: From theoretical assumptions to practical estimation. *Chaos: An Interdisciplinary Journal of Nonlinear Science* **28**: 075310. doi: 10.1063/1.5025050.

Runge, J., Bathiany, S., Bollt, E., Camps-Valls, G., Coumou, D., Deyle, E., Glymour, C., Kretschmer, M., Mahecha, M. D., Muñoz-Marí, J., van Nes, E. H., Peters, J., Quax, R., Reichstein, M., Scheffer, M., Schölkopf, B., Spirtes, P., Sugihara, G., Sun, J., Zhang, K., and Zscheischler, J. (2019a) Inferring causation from time series in Earth system sciences. *Nature Communications* **10:** 2553. doi: 10.1038/s41467-019-10105-3.

Runge, J., Nowack, P., Kretschmer, M., Flaxman, S., and Sejdinovic, D. (2019b) Detecting and quantifying causal associations in large nonlinear time series datasets. *Science Advances* **5:** eaau4996. doi: 10.1126/sciadv.aau4996.

Runge, J. (2020). Discovering contemporaneous and lagged causal relations in autocorrelated nonlinear time series datasets. In: Conference on Uncertainty in Artificial Intelligence (pp. 1388-1397). PMLR. arXiv:2003.03685.

Saggioro, E. and Shepherd, T.G. (2019) Quantifying the Timescale and Strength of Southern Hemisphere Intraseasonal Stratosphere-troposphere Coupling. *Geophysical Research Letters* **46**: 13479–13487. doi: 10.1029/2019GL084763.

Samarasinghe, S.M., Deng, Y., and Ebert-Uphoff, I. (2020) A Causality-Based View of the Interaction between Synoptic- and Planetary-Scale Atmospheric Disturbances. *Journal of the Atmospheric Sciences* **77**: 925–941. doi: 10.1175/JAS-D-18-0163.1.

Schleussner, C.F., Runge, J., Lehmann, J., and Levermann, A. (2014) The role of the North Atlantic overturning and deep ocean for multi-decadal global-mean-temperature variability. *Earth System Dynamics* **5:** 103–115. doi: 10.5194/esd-5-103-2014.

Schwierz, C., Croci-Maspoli, M., and Davies, H.C. (2004) Perspicacious indicators of atmospheric blocking. *Geophysical Research Letters* **31**: L06125. doi: 10.1029/2003GL019341.

Shutts, G.J. (1983) The propagation of eddies in diffluent jetstreams: Eddy vorticity forcing of 'blocking' flow fields. *Quarterly Journal of the Royal Meteorological Society* **109**: 737–761. doi: 10.1002/qj.49710946204.

Sillmann, J., Croci-Maspoli, M., Kallache, M., and Katz, R.W. (2011) Extreme Cold Winter Temperatures in Europe under the Influence of North Atlantic Atmospheric Blocking. *Journal of Climate* **24**: 5899–5913. doi: 10.1175/2011JCLI4075.1.

Simmons, A.J. and Hoskins, B.J. (1979) The Downstream and Upstream Development of Unstable Baroclinic Waves. *Journal of the Atmospheric Sciences* **36**: 1239–1254. doi: 10.1175/1520-0469(1979)036<1239:TDAUDO>2.0.CO;2.

Slingo, J.M. (1998) Extratropical forcing of tropical convection in a northern winter simulation with the UGAMP GCM. *Quarterly Journal of the Royal Meteorological Society* **124**: 27–51. doi: 10.1002/qj.49712454503.

Spirtes, P. and Glymour, C. (1991) An Algorithm for Fast Recovery of Sparse Causal Graphs. *Social Science Computer Review* **9:** 62–72. doi: 10.1177/089443939100900106.

Stock, J.H. and Watson, M.W. (2015) Introduction to econometrics. updated 3. Ed. Pearson, Boston. ISBN-13: 9781292071312.

Vallis, G.K. (2007) Atmospheric and Oceanic Fluid Dynamics: Fundamentals and Large-Scale Circulation. Cambridge University Press, Cambridge.

van der Wiel, K., Matthews, A.J., Joshi, M.M., and Stevens, D.P. (2016) The influence of diabatic heating in the South Pacific Convergence Zone on Rossby wave propagation and the mean flow. *Quarterly Journal of the Royal Meteorological Society* **142**: 901–910. doi: 10.1002/qj.2692.

Vautard, R. (1990) Multiple Weather Regimes over the North Atlantic: Analysis of Precursors and Successors. *Monthly Weather Review* **118**: 2056–2081. doi: 10.1175/1520-0493(1990)118<2056:MWROTN>2.0.CO;2.

Wald, A. (1943) Tests of statistical hypotheses concerning several parameters when the number of observations is large. *Transactions of the American Mathematical Society* **54**: 426–482. doi: 10.1090/S0002-9947-1943-0012401-3.

Welch, B.L. (1947) The generalisation of student's problems when several different population variances are involved. *Biometrika* **34**: 28–35. doi: 10.1093/biomet/34.1-2.28.

Whan, K., Zwiers, F., and Sillmann, J. (2016) The Influence of Atmospheric Blocking on Extreme Winter Minimum Temperatures in North America. *Journal of Climate* **29**: 4361–4381. doi: 10.1175/JCLI-D-15-0493.1.

Wheeler, M.C. and Hendon, H.H. (2004) An All-Season Real-Time Multivariate MJO Index: Development of an Index for Monitoring and Prediction. *Monthly Weather Review* **132**: 1917–1932. doi: 10.1175/1520-0493(2004)132<1917:AARMMI>2.0.CO;2.

Wirth, V., Riemer, M., Chang, E.K.M., and Martius, O. (2018) Rossby Wave Packets on the Midlatitude Waveguide—A Review. *Monthly Weather Review* **146**: 1965–2001. doi: 10.1175/MWR-D-16-0483.1.

Wirth, V. (2020) Waveguidability of idealized midlatitude jets and the limitations of ray tracing theory. *Weather and Climate Dynamics* **1**: 111–125. doi: 10.5194/wcd-1-111-2020.

Wolf, G. and Wirth, V. (2017) Diagnosing the Horizontal Propagation of Rossby Wave Packets along the Midlatitude Waveguide. *Monthly Weather Review* **145**: 3247–3264. doi: 10.1175/MWR-D-16-0355.1.

Zhang, C. (2005) Madden-Julian Oscillation. *Reviews of Geophysics* **43:** RG2003. doi: 10.1029/2004RG000158.

Declaration of consent

on the basis of Article 30 of the RSL Phil.-nat. 18

Name/First Name: Meyer Lukas

Registration Number: 14-402-713

Study program: Master of Science in Climate Sciences

Bachelor ☐   Master ✔   Dissertation ☐

Title of the thesis: Analysing Potential Drivers of Recurrent Rossby Wave Packets using Causal Inference

Supervisor: Prof. Dr. Olivia Romppainen-Martius

I declare herewith that this thesis is my own work and that I have not used any sources other than those stated. I have indicated the adoption of quotations as well as thoughts taken from other authors as such in the thesis. I am aware that the Senate pursuant to Article 36 paragraph 1 litera r of the University Act of 5 September, 1996 is authorized to revoke the title awarded on the basis of this thesis.

For the purposes of evaluation and verification of compliance with the declaration of originality and the regulations governing plagiarism, I hereby grant the University of Bern the right to process my personal data and to perform the acts of use this requires, in particular, to reproduce the written thesis and to store it permanently in a database, and to use said database, or to make said database available, to enable comparison with future theses submitted by others.

Bern, 25.01.2022

Place/Date

Signature